Investigations on the photoelectrochemical properties of MBE-grown $In_xGa_{1-x}N$ thin films

A Thesis
Submitted for the Degree of
DOCTOR OF PHILOSOPHY
In the Faculty of Science

By

SHIVARAM B KUBAKADDI

Chemistry and Physics of Materials Unit
Jawaharlal Nehru Centre for Advanced Scientific Research
Bangalore – 560064, India

July 2022

DECLARATION

I hereby declare that the matter embodied in this thesis entitled **"Investigations on the photoelectrochemical properties of MBE grown $In_xGa_{1-x}N$ thin films"** is the result of the research carried out by me at the Chemistry and Physics of Materials Unit, Jawaharlal Nehru Centre for Advanced Scientific Research, Bangalore, India, under the supervision of **Prof. S. M. Shivaprasad** and it has not been submitted elsewhere for the award of any degree or diploma.

In keeping with the general practices of reporting scientific observation, due acknowledgments have been made whenever the work described is based on the findings of other investigators. Any omission which might have occurred by oversight or error in judgment is regretted.

Bengaluru

....
Shivaram B Kubakaddi

CERTIFICATE

I hereby certify that the matter embodied in this thesis entitled **"Investigations on the photoelectrochemical properties of MBE grown $In_xGa_{1-x}N$ thin films"** has been carried out by **Mr. Shivaram B Kubakaddi** at the Chemistry and Physics of Materials Unit, Jawaharlal Nehru Centre for Advanced Scientific Research, Bangalore, India under my supervision and that has not been submitted elsewhere for the award of any degree or diploma.

Bengaluru

Professor S. M. Shivaprasad
(Research Supervisor)

Acknowledgments

I take this opportunity to acknowledge and express my gratitude to all the people who have inspired, motivated, and supported me throughout my Ph.D. journey.

First, I am deeply grateful to my supervisor, Prof. S. M. Shivaprasad, for his invaluable academic guidance, enormous support, kindness and encouragement throughout all stages of this work. It is a great experience to be working with him. I am fully grateful for all that he has taught me. It has been a great privilege for me to have been educated by him. I appreciate the efforts that he has made in my personal development as a researcher and in numerous discussions required by this study. I would like to thank Prof. M. Eswaramoorthy for his care towards our lab when Prof. Shivaprasad was on a lien.

I thank Dr. Saraswathi for the constant support, motivation, and guidance throughout my Ph. D., without her support this work would not have been possible. Also, I would like to thank her family for their hospitality.

I would like to thank Dr. Bivas Saha for taking care of lab-related issues. Also, for memorable times spent with his group in the lab and outside the lab.

I thank Prof. C.N.R. Rao and all the past and present chairpersons of CPMU for providing us with world-class research facilities and scientific temper through various talks here at JNCASR. I also express my sincere gratitude to Prof. K. S. Narayan, Prof. N. S. Vidhyadhiraja, Prof. A. Sundaresan, Prof. Umesh V. Waghmare, Prof. S. M. Shivaprasad for their informative course work, where I gained basic concepts materials science, which has been very useful for my Ph. D work.

I would like to thank Mr. Srinath, for helping and educating me with matters pertaining to electronic circuits, vacuum systems, baking and maintaining MBE system, fixing other important pieces of apparatus, without his help successful experiments would not have been possible. I also thank Mr. Alla Srinivas Rao for the help in PVD system related issues, Mr. Mahesh, Mr. Prajwal, Dr. Jay Ghatak, Ms. Meenakshi, Dr. Selvi and Mr. Rahul for FESEM imaging, Mr. Jagadeesh and Mr. Prajwal for XPS measurements, Mr. Vasu for Raman spectroscopy and Mr. Anil for XRD measurements. All the help provided by Academic

Section, DG room, Security, Dhanvantri, Administrative Section, Library, Complab and Hostel Authority is also greatly appreciated.

I thank the Council of Scientific and Industrial Research (CSIR) for providing me research fellowship and JNCASR for financial assistance in the later part of my Ph.D.

I would like to thank Dr. Bharath, Dr. Shashidhara, Dr. Shreedhara, Mr. Reetendra, Ms. Dheemahi, Mr. Krishna, Dr. Abhijit, Ms. Divya, Dr. Premakumar Dr. Pradeep for the help in various experimental measurements.

I would like to thank all the lab members of Epitaxy Lab (MBE) and Heterogenous Integration Research Group (HIRG); Dr. Varun, Dr. Arpan, Dr. Sanjay, Dr. Nagaraja, Dr. Muthuvinayagam, Dr. Shashidhara, Dr. Saraswathi, Dr. Anjan, Dr. Abhijit, Dr. Rajendra, Mr. Sachin, Mr. Gururaj, Mr. Sachin, Mr. Anirudh, Mr. Samip, Ms. Dheemahi and Mr. Vinayak, Krishna, Bidesh, Sourjyadeep, Prasanna, Deeksha, Krithika, Sourav, Rahul, Debmalya, Dr. Nidhi, Mehak, Sneha and Ankit for their informative discussions and pleasant atmosphere in the lab, during my Ph.D. I have learned a lot of things throughout this Ph. D. journey.

I would like to thank all my batchmates and friends, special thanks to Dr. Pradeep, Dr. Premakumar, Dr. Ravishankar, Dr. Rajendra, Dr. Divya, Dr.Priyanka, Dr. Ganesh, Mr. Deepak, Dr. Usha, Dr. Anusha, Dr. Malay, Mr. Vybhav, Dr. Manodeep, Ms. Pavitra, Dr. Aditya, Dr. Manjeet, Dr. Raaghesh, Dr. Chandan, Mr. Bhupesh, Mr. Shashank, Mr. Navneet and Mr. Devendra Panda. The countless memories that I have built with them, from everyday activities to sports, movies, dinners, and trips will always have a special place in my heart. Mr. Reetendra, Dr. Bharath, Dr. Rajashekhar, and many friends from Basketball, Cricket, Badminton, and Volleyball groups, for making this Ph. D. life enjoyable and memorable.

I would like to thank my special friends, Ms. Deepa, Mr. Gangadhar, Dr. Ashok, and Dr. Umakant for being there every time with me as a family member. Also, I would like to thank Mr. Santosh, Dr. Madhuri, and Dr. Veena for their support.

I also would like to thank all my teachers from kindergarten to Ph.D. And finally, I would like to thank all my family members for their supporting me in whatever pursuit I have chosen.

Synopsis

The group III-nitride semiconductors and related alloys have shown great utility in the development of electronic and optoelectronic devices. Their tunable bandgap from deep UV to Near-IR and chemical robustness under high electrical current and temperature, make them best suited for the fabrication of high temperature, high frequency, high power electronic, and optoelectronic devices. Among ternary compounds of group III-nitride semiconductors, $In_xGa_{1-x}N$ is the key material in fabricating light emitters since it covers the visible region of the electromagnetic spectrum. Since the band gap of GaN straddles the redox potential of water and the bandgap tuning can be optimized, it is a potential candidate for hydrogen generation. However, growing high-quality $In_xGa_{1-x}N$ thin films poses problems of phase separation, due to the large miscibility gap between InN and GaN, the high vapor pressure of InN leading to low indium incorporation, strong indium surface segregation due to formation enthalpies of GaN and InN, etc. These problems can be minimized by carefully optimizing the growth parameters such as low growth temperatures, low growth rates, low growth pressure, and high V/III flux ratio.

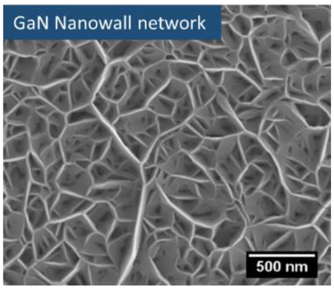

In the past, our research group has studied different nanostructures of GaN, among which GaN Nanowall Network (NWN) is studied extensively, because of its advantages like high surface area, minimal stress and defects, high conductivity and can be grown spontaneously. All these properties motivated us to explore the photoelectrochemical properties of $In_xGa_{1-x}N$ thin films. To understand these properties, we varied indium composition, surface morphology, and different substrates. We also formed GaN/TiO_2 heterostructures and studied their properties.

The work in the present thesis is organized in the following chapters:

Chapter 1 gives a brief introduction of group III-Nitrides and discusses their importance. The chapter includes general information about crystal structure and growth techniques used for thin films of III-nitride deposition, and its different nucleation and growth modes. The brief introduction to $In_xGa_{1-x}N$ includes a historical perspective of growth kinetics and difficulties in the growth of $In_xGa_{1-x}N$ thin films (such as phase separation, high indium incorporation, etc). An introduction to photoelectrochemical water splitting and its working principle is included. The latter part describes the motivation for the selection of this system and a brief discussion on $In_xGa_{1-x}N$ photoelectrodes.

Chapter 2 provides the details of the different experimental techniques used in this study. It begins with some basic information on Plasma Assisted Molecular Beam Epitaxy system to grow thin films, which consists of effusion cells, Nitrogen RF Plasma Source, Reflection High Energy Electron Diffraction, and Residual Gas Analyzer. Also, the principle of Atomic Layer Deposition and Physical Vapor Deposition systems are provided. The details of characterization tools such as Field Emission Scanning Electron Microscopy, Atomic Force Microscopy, High-Resolution X-ray Diffraction, Cathodoluminescence, Photoluminescence, and Ultraviolet-Visible spectroscopy, X-ray Photoelectron Spectroscopy and Hall Effect Measurements are given briefly and finally, the Photoelectrochemical setup used in the study is discussed.

Chapter 3 contains two parts: First part discusses the comparison of photoelectrochemical properties of heterostructures of TiO_2 deposited on GaN Epilayer and GaN nanowall network. The later part discusses observed results of $In_xGa_{1-x}N$ thin films grown on c-Sapphire, and their heterostructure with TiO_2. TiO_2/GaN nanowall network and $TiO_2/In_{0.16}Ga_{0.84}N$ heterostructure photoelectrodes are seen to yield better performances in photocurrent densities (in Na_2SO_4 electrolyte) which is attributed to increased band bending in heterostructures and that is employed to separate the charge carriers. The schematic band diagrams are drawn by obtaining the values from absorption, emission, XPS, and other studies to estimate the band bending.

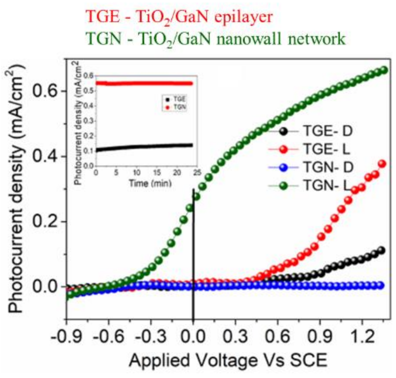

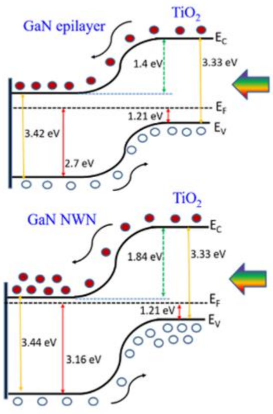

Chapter 4 which contains three parts discusses photoelectrochemical studies on $In_xGa_{1-x}N$ grown on c-sapphire with GaN buffer layer. The first part discusses the role of morphology for the samples that were grown with different growth parameters such as varying nitrogen flux and the thickness of the films to change the surface morphology. The roughness of these films is measured by AFM and photoelectrochemical studies show enhanced photocurrent densities as the roughness of the samples increases. In part two, $In_xGa_{1-x}N$ thin films were grown by varying the indium flux. The indium composition is increased with increasing indium flux, which causes a decrease in the bandgaps. The photoelectrochemical studies show better performance in thin films that have the highest indium composition. In part three, photoelectrochemical studies on $In_xGa_{1-x}N$ photoelectrodes are performed on three different electrolytes, namely, Na_2SO_4, HCl, and NaOH. In the case of NaOH, the onset potential in the linear sweep voltammogram is compared to that of the other two, as shown in the figure. Also, the photoelectrodes are observed to be etched out after the experiment in NaOH, which is confirmed by FESEM and XRD techniques.

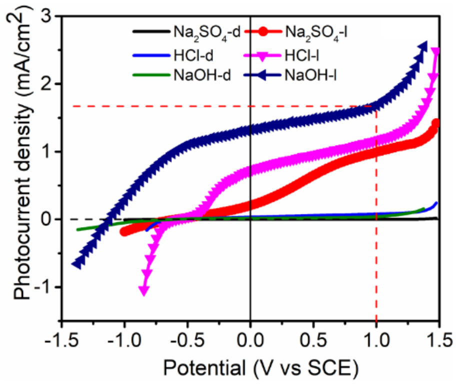

Chapter 5 consists of two parts. In the first part, the photoelectrochemical properties of $In_xGa_{1-x}N$ thin films that are grown on heavily doped Si (111) substrates, are studied. The linear sweep voltammogram shows the anodic shift in the onset potential compared to $In_xGa_{1-x}N$ grown on c-sapphire. The shift is attributed to silicon nitride formation at the interface. To understand this in the second part $In_xGa_{1-x}N$ thin films are grown simultaneously on Si (111) and on TiN {which is grown on Si (111)}. The HRXRD pattern shows an epitaxial relationship with the substrate and the phi-scan reflects the six-fold symmetry. The observed linear sweep voltammogram shows the cathodic shift in the case of $In_xGa_{1-x}N$ grown on TiN compared to $In_xGa_{1-x}N$ grown on Si, as shown in the figure. This may be due to interfacial silicon nitride formation during growth.

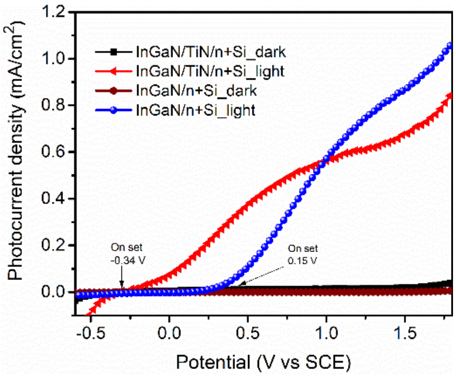

Chapter 6 summarizes the research work of the thesis and concludes with the observed results. Overall, the thesis is a systematic approach to understanding the photoelectrochemical properties of $In_xGa_{1-x}N$ thin films with different surface morphologies, indium compositions, and the formation of heterostructure with TiO_2. This chapter also provides a brief outlook for the future direction of studies on this system.

Table of Contents

List of Figures

Chapter 1
Introduction and Literature Review

This chapter describes the importance of Group III nitrides and their applications. Crystal structure, substrates used to grow the films, and a brief review of InGaN and its properties are presented. Also, an introduction to photoelectrochemical water splitting phenomena is provided.

1.1 A brief introduction to III-Nitrides

The research and technological developments in electronic materials and devices during the semiconductor age have changed our views, and attitudes towards our way of life in the last few decades. during the 'Semiconductor Age' in the last few decades. Mobile phones, Personal computers, and LED-based lighting and display devices are just a few examples of the huge array of electronic devices that have influenced our living styles. Nitride-based LED and Laser Diode (LD) are notable examples in this context among which the blue LED was the product of a scientific breakthrough in 1994 that led to a revolution in optoelectronics, for which Shuji Nakamura, Hiroshi Amano, and Isamu Akasaki were awarded the prestigious Nobel prize in 2014.

Group-III nitride semiconductors, aluminium nitride (AlN), gallium nitride (GaN), indium nitride (InN), and their alloys, are a unique class of materials that can be used to design and mass-produce a wide range of electrical and optoelectronic devices. The outstanding properties of these materials are well explored in numerous literature[1–11] and books[12,13]. One of the important properties of these materials is that their room temperature bandgaps can be tuned over a range spanning from 0.64 eV (InN)[14] to 6.02 eV (AlN)[15] by alloying as shown in Figure 1.1. As a result, absorption, emission, and detection of wavelengths ranging from near-infrared (NIR) to deep ultraviolet (UV) have become possible. Another benefit of III-nitride semiconductors is the nature of their strong chemical bond, which is both ionic and covalent, making them exceptionally stable and resistant to deterioration at high electric currents and temperatures. Their large piezoelectric constants, spontaneous polarization, and high thermal and mechanical stability make them good candidates for the fabrication of optoelectronic and electronic devices that can operate at high frequencies, high temperatures, and high-power densities, consequently opening up applications in a wide range of areas such as solid-state lighting, full color displays, sensors and diagnostics, high-density optical information storage, radio frequency (RF) amplifiers, and power electronic devices[16].

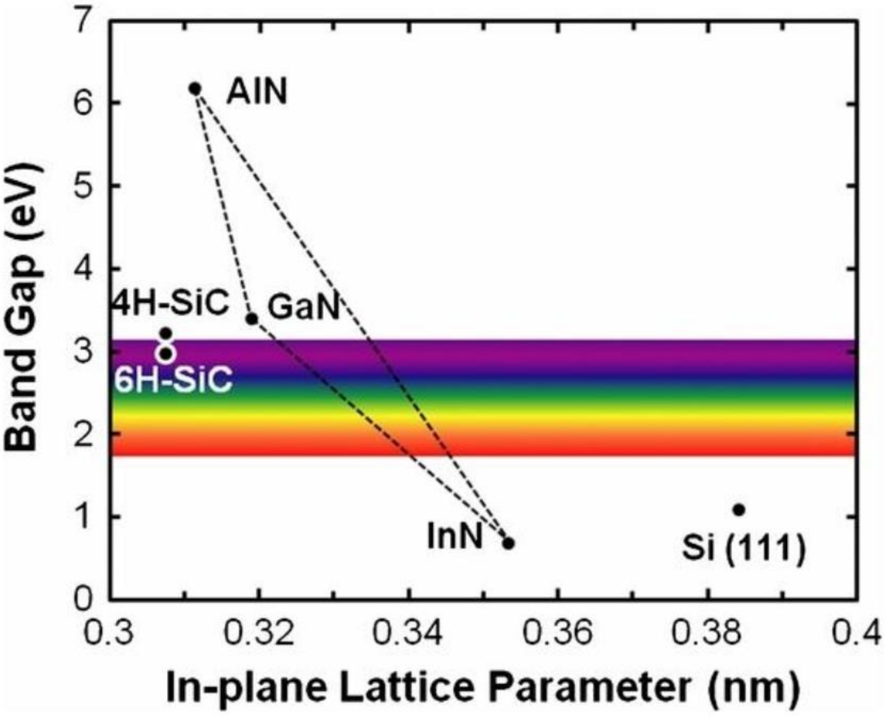

Figure 1.1 RT band gap energies vs lattice constants of Group III-Nitride semiconductors[17]. (©IOP Publishing. Reproduced with permission. All rights are reserved)

Juza et al. were the first to show the synthesis of GaN and InN crystallites in 1938. GaN was created by passing ammonia over hot gallium, and InN was created by reducing $InF_6(NH_4)_3$. The goal of these investigations was to determine the lattice parameters of the synthesized materials[18]. After almost three decades, Maruska et al. were the first to grow GaN layers on sapphire substrates using vapor phase deposition, which spurred interest in the nitrides among researchers[19]. Pankove et al. created blue LEDs based on GaN:Zn/nGaN structures on vapor phase grown GaN, where the structures depended on hot carrier injection from avalanche breakdown to generate holes [20].

Since then, GaN growth has been intensively pursued. However, GaN is spontaneously n-type with a large carrier concentration, but the growth of p-type GaN has been difficult. It wasn't until 1989 that Amano et al. were able to reliably produce it by doping it with Mg[21]. Nichia Chemical Industries researchers Nakamura et al. used Mg doping to construct p-n junctions, which produced at the time, the brightest blue LEDs [22–24]. It was then that Nichia Chemical Industries and others began commercializing blue and green LEDs. Following this, the first Laser Diodes (LDs) based on the III-nitride material system were developed by Akasaki et al. and Nakamura et al[25]. Since then, growth in science and technology of III-nitrides has progressed at a remarkable rate, with an expanding number of research groups participating.

The early 1990s saw the discovery of strain-induced and spontaneous piezoelectric polarisation phenomena in III-nitride materials. $Al_xGa_{1-x}N$/GaN high electron mobility transistors (HEMTs) were also demonstrated as a result of this research, which led to the development of the 2-Dimensional Electron Gas (2DEG). Nichia reported in 2002 that it has developed high-power InGaN LEDs for white, blue, and green light emission with a lifetime of approx. 100000 hours. As a result, all devices are currently researched using nitride compounds and alloys, starting with heterostructure LEDs and LDs and progressing to fabricating HEMTs.

1.1.1 Crystal structure of III-Nitrides

III-nitride semiconductors demonstrate partially ionic bonding with a strong charge transfer between the less electronegative metal atoms (Al, Ga, or In) and the highly electronegative nitrogen atoms. The bond strength of Ga-N is 2.23 eV, which is similar to the bond strength of C-C in diamond (1.9 eV), but stronger than the other well-known III-V semiconductor, GaAs, whose bond strength is 1 eV. III-nitrides with a wurtzite crystal structure are thus thermodynamically more stable (Figure 1.2a). Other than this, there also exists a meta-stable zinc blend structure for this material.

The wurtzite crystal structure is formed by two translated compact hexagonal close-packed (hcp) sub-lattices of N and metal atoms, that are shifted with respect to each other by 62% of the length of a unit cell in the c-direction and the structure is shown in the Figure 1.2a. Figure 1.2b shows the different crystallographic planes in the hexagonal crystal structure. The family of planes {0001} is referred to as basal plane or most commonly as c-plane, $\{10\bar{1}0\}$ plane is referred to as prismatic or m-plane, and the plane perpendicular to the m-plane is referred to as a-plane $\{11\bar{2}0\}$. Both the a-plane and the m-plane have the special feature of having an equal number of Ga and N atoms in each layer, making them non-polar. The absence

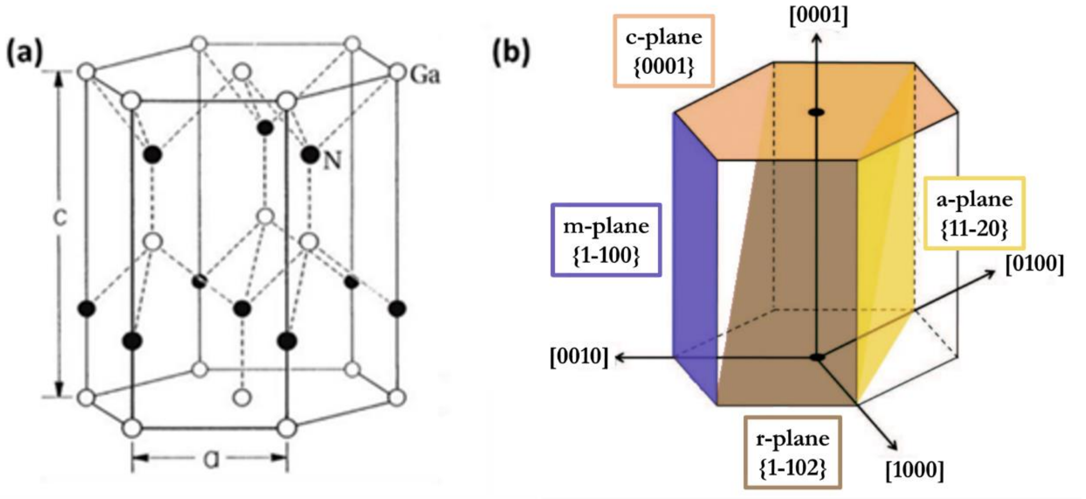

Figure 1.2 (a) Wurtzite crystal structure of GaN and (b) some crystallographic plane representation.

of in-built polarisation due to the non-polar nature of films formed with these planes has removed a long-standing roadblock in the development of extremely efficient devices. The stacking sequence of closely packed diatomic planes in the c-direction differs between wurtzite and zinc-blende structures. The stacking sequence in the <0001> direction of the wurtzite structure is ABAB, whereas the stacking sequence in the <111> direction of the zinc blende structure is ABCABC. A slight difference in these sequences leads to defects in the crystal structure resulting in a stalking fault. Due to the low formation energy of roughly 10mmeV in GaN and 19 meV in InN, stacking faults are very common during growth. III-nitrides have four atoms per unit cell. The metal atom (Al, Ga, or In) is surrounded by four nitrogen atoms. The polarity of the formed film is either Ga- or N-polar, depending on the growth parameters. Polarity is the bonding sequence that results from the stacking configuration within the atomic layers. This is owing to the non-centrosymmetric character of group III-nitrides in the wurtzite crystal structure along the <0001> direction, which increases the likelihood of the film having two opposing atomic layers in the stacking sequences. GaN (0001), for example, is Ga-polar, with a vertical bond from a Ga atom to an N atom above it, but GaN $(000\bar{1})$ is N-polar, with the vertical bond from an N atom to a Ga atom above it, as shown in Figure 1.3. The polarity of films grown on sapphire substrate in MBE and MOCVD growths is determined by the buffer layer utilized. Ga-polar GaN is known to be initiated by AlN buffer layers, and N-polar GaN is initiated by GaN buffer layers. Chemical etching is a useful method used for determining GaN polarity, where the relative etching rate is high for N-polar surfaces while the film stays unchanged even after long periods of exposure to the etchant for Ga-polar surfaces.

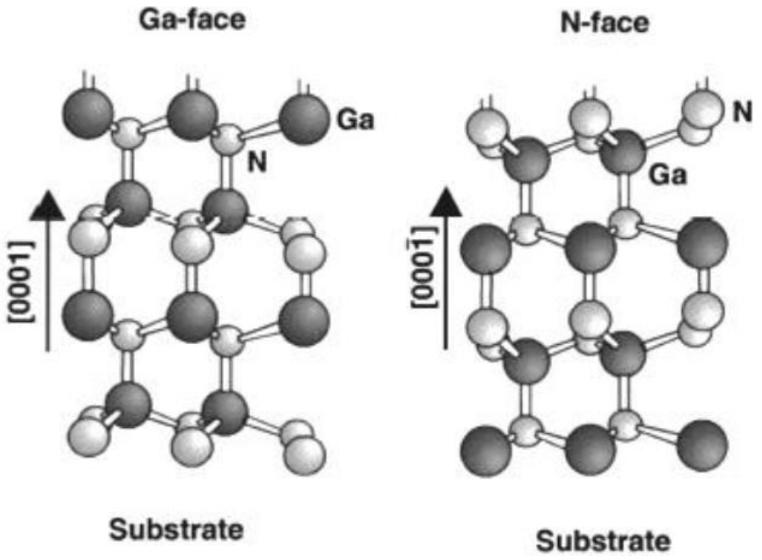

Figure 1.3 Polarity in GaN[1]*: (a) Ga-polar along* [0001] *and N-polar along* [000$\bar{1}$]. (*©IOP Publishing. Reproduced with permission. All rights are reserved.*)

1.1.2 Substrates

The scarcity of affordable and large single crystals that can be utilized as substrates for homoepitaxial growth is a specific challenge in the growth of III-nitride thin films. As a result, heteroepitaxial growth is the only option, although substrate selection is crucial. This is a long-standing issue, and several studies have been published towards resolving it, on the effects of the substrate on the structural, electrical, and morphological aspects of compound semiconductor thin films[26–35]. Hetero-epitaxial growth necessitates the use of a substrate with a surface template that matches the target material's crystal symmetry and lattice parameters. The mismatch in lattice parameters between the substrate and the film causes the formation of misfit dislocations at the interfaces to release the strain caused by the mismatch. Regrettably, relaxation is rarely restricted to the interface and the dislocations typically propagate over the thickness of the films and are thus called threading dislocations. Not only does the lattice parameter difference play a crucial role in heteroepitaxial growth, but the thermal behavior of the substrate and epitaxial layers must also be effectively managed. Depending on the differences in their thermal expansion coefficients, the substrate and film will relax in dramatically different ways when they cool down from the growth temperature, and overgrown films form deformation and cracks.

MOCVD and VPE (Vapour Phase Epitaxy) substrate materials with low thermal expansion and lattice-mismatched are limited to those unaffected by high concentrations of Ammonia and Hydrogen at temperatures above 1000°C. Even though the growth temperatures for PAMBE are roughly 200 degrees Celsius, lower than for VPE and MOCVD, the substrate surfaces must be stable under the effect of nitrogen plasma at 800 degrees Celsius. The substrate of choice for device manufacturing procedures must be available in a minimum size wafer of two inches, with atomically smooth surfaces, and in huge quantities at reasonable prices. sapphire, silicon, and silicon carbide are the most common substrate materials used under these assumptions. The lattice parameters, mismatch, and thermal expansion coefficients differ significantly across the nitrides and the substrates utilized, as shown in Table 1.1. As a result, if no extra precautions are taken, high defect concentrations will result from the heteroepitaxy of nitride layers on these substrates. The main criterion for selecting a substrate is that it has a low lattice mismatch. The misfit parameter (f_m) is calculated as $f_m = (a_{substrate} - a_{film})/a_{substarte}$, where $a_{substarte}$ and a_{film} are the substrate and film lattice constants, respectively.

Table 1.1 parameters for III-Nitrides and most commonly used substrates.

Material	**Crystal Structure**	**Lattice constant (Å)**		**Lattice mismatch (approx. %) w.r.t.**			**Thermal expansion ($10^{-6}K^{-1}$)[12,36]**	
		a_o	**c_o**	**AlN**	**GaN**	**InN**	**‖a-axis**	**‖ c-axis**
AlN	Wurtzite	3.1106[37]	4.9795[37]	0	2.5	12.1	4.20	5.30
GaN	Wurtzite	3.1893[38]	5.1852[38]	-2.5	0	9.8	3.17	5.59
InN	Wurtzite	3.5376[39]	5.7064[39]	-13.7	-10.9	0	3.09	2.79
Al_2O_3	Hexagonal	4.765[40]	12.982[40]	34.7	33.1	25.7	5.00	9.03
SiC	Wurtzite	3.0806[40]	15.1173[40]	-0.97	-3.5	-14.8	4.30	4.70
Si	Cubic	a = b = c = 5.431[40]		23.4	16.9	8	3.59	

Although sapphire has a large lattice and thermal expansion mismatch with III-nitrides, it has been widely employed for epitaxial growth of III-nitrides in a variety of orientations, including c-(0001), a-$(11\bar{2}0)$, m-$(10\bar{1}0)$ and r-$(10\bar{1}2)$. Because of this substantial discrepancy, III-nitride unit cells tend to rotate 30 degrees around the c-axis when compared to sapphire unit cells, and consequently the lattice mismatch and the nitrogen and III-element sub-lattices of the two materials are aligned[41]. As mentioned above the mismatch between sapphire and III-nitride lattice properties is thus determined using the following relation in this orientation: $f_m = (a_{substrate} - 2a_{film}cos\theta)/a_{substrate}$, where θ is the angle of rotation of the III-nitride unit cell with respect to sapphire. When InN is grown directly on c-sapphire, two types of in-plane rotational domains can be seen with epitaxial relationships of $[10\bar{1}0]_{InN}||[11\bar{2}0]_{Sapphire}$ and $[11\bar{2}0]_{InN}||[11\bar{2}0]_{Sapphire}$ where the magnitude of lattice mismatches is almost equal. InN has an equal chance of growing in both epitaxial directions, on sapphire. The lattice mismatch between c-sapphire and III-nitrides is tabulated below in Table 1.2.

Table 1.2 Lattice mismatch between III-nitrides and c-Sapphire along <$11\bar{2}0$> and <$10\bar{1}0$>directions.

	$[11\bar{2}0]_{III-nitride}||[11\bar{2}0]_{Sapphire}$	$[10\bar{1}0]_{InN}||[11\bar{2}0]_{Sapphire}$
AlN	34.7%	-13.1%
GaN	33.1%	-15.9%
InN	25.7%	-28.6%

Si (111), on the other hand, is being intensively investigated as a potential alternative substrate for III-nitride growth due to its excellent doping properties, high abundance, low cost, good thermal conductivity, excellent crystal quality, availability of large-sized wafers, ease of cleavability, and the benefit of integrating III-nitrides with the mature Silicon technology[42].

1.1.3 Nucleation and Growth of Thin Film

The growth of thin film depends on various factors, and the critical ones are the substrate surface energy, the symmetry of the surface, the lattice mismatch between the substrate and the film, the supersaturation (flux) of the crystallizing phase, the growth temperature, etc. The following Figure 1.4 depicts the several steps involved in thin film nucleation and growth.

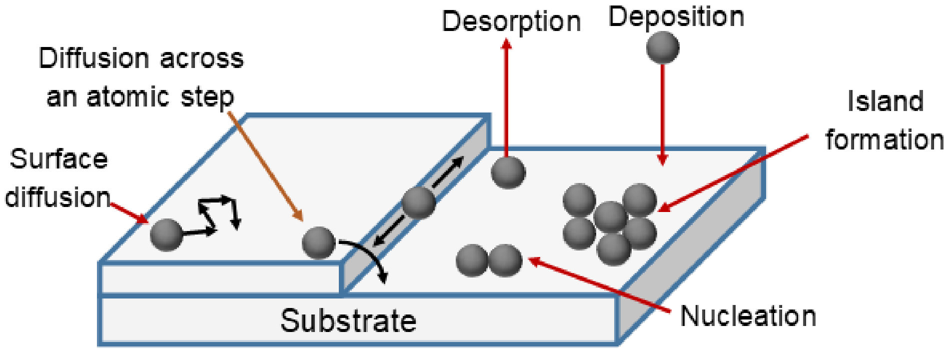

Figure 1.4 Schematic diagram of various processes involved during thin film nucleation and growth

When atoms or molecules approach a crystalline surface, they begin to interact with the surface atoms as well as the Potential Energy Surface (PES) that they have formed. Incoming atoms are either reflected or transfer sufficient energy to the lattice to become weakly bonded to the surface as adatoms, depending on the interaction. The incoming flux, the trapping chance, and the sticking coefficient of the arriving atom on the substrate surface all play a role in this process. Because the adsorbed particles are restricted in a two-dimensional phase state, they are not strongly bonded to the surface and can move freely on the substrate surface, induced by the energy from lattice vibrations. The adatoms must cross the PES's saddle ridges to perform such movements. Random jumps of an adatom from one PES minimum to another are known as surface diffusion. These adatoms diffuse around on the surface until they either desorb, form a stable nucleus, or attach to a stable island that has already been formed. Some part of the adsorbed atoms forms nuclei, compared to isolated sub-critical clusters, because they are energetically favorable, however, the aggregated adatoms can still disintegrate. Only once a specific nucleus size is reached it is more energetically advantageous to attach, rather than lose atoms. The surface mobility of adatoms is dependent on the growth temperature, their kinetic energy upon impact, and the strength of interaction between the substrate and a single atom. If this interaction is strong, then high nucleus density can be obtained otherwise large islands with low nucleus density are formed.

1.1.3.1 Thin Film Growth Modes

At the nucleation stage of epitaxial thin film growth, three main growth patterns have been identified, which are schematically represented in Figure 1.5 and briefly described here.

Volmer-Weber (VW) mode

This is the three-dimensional growth mode, often known as island growth. Adatoms form clusters on the substrate in Volmer-Weber mode (Figure 1.5a), which then expand into individual islands. When the adatoms are more tightly bonded to each other than to the substrate, sluggish surface diffusion occurs. Thus, the thermodynamic condition required for island growth is

$$\gamma_{substrate} < \gamma_{film} + \gamma_{interface}$$

Where, $\gamma_{substrate}$ is the surface energy of a substrate

γ_{film} is the surface energy of the film

$\gamma_{interface}$ is interface energy between substrate and film

This non-wetting mode governs heteroepitaxial growth when the two materials have completely different symmetries, surface energies, and a large lattice mismatch, such as when metals grow on insulators and semiconductors, including many metals on alkali halides, graphite, and other layered compounds like mica.

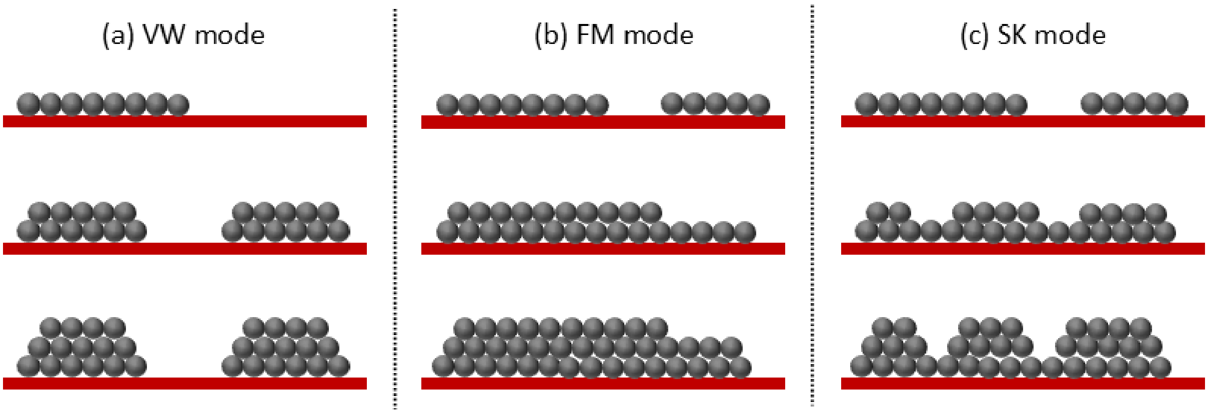

Figure 1.5 Schematic of different growth modes (a) Volmer-Weber, (b) Frank-van der Merwe, and (C) Stranski-Krastanov.

Frank-van der Merwe (FM) mode

This is the two-dimensional growth mode, often known as layer-by-layer growth. When adatoms are more strongly bound to the substrate than to each other, the Frank-van der Merwe mode (Figure 1.5b) unfolds, allowing for quicker adatom surface diffusion. As a result, the first atoms condense, tending to form a full monolayer on the surface, which is then covered by a slightly less tightly bonded second layer. The growth proceeds in a smooth, layer-by-layer fashion, yielding the best crystalline quality. Thus, the thermodynamic condition required for growth is

$$\gamma_{substrate} \geq \gamma_{film} + \gamma_{interface}$$

When the two materials have similar or almost equivalent characteristics such as symmetry, lattice parameters, surface energies, etc, this wetting growth mode occurs. e.g., in the case of adsorbed gases, some metal-metal systems, and in semiconductor growth on semiconductors.

Stranski-Krastanov (SK) mode

In Stranski-Krastanov growth mode, layer-by-layer growth is followed by island growth mode. The first monolayer (ML) or a few ML are generated in the SK mode (Figure 1.5c), but the following layer growth becomes unfavorable, and islands begin to form on top of this 'intermediate' layer. There are numerous conceivable causes for this mode to arise, and practically any factor that disrupts the layer growth's characteristic monotonic decline in binding energy could be the catalyst for subsequent 3D growth. For example, a strain in the film is caused by a lattice mismatch between the film and the substrate, which can explain the transition from 2D layer to 3D island formation modes. Thus, the thermodynamic condition required for growth is

Initially, $\gamma_{substrate} \geq \gamma_{film} + \gamma_{interface}$

Finally, $\gamma_{substrate} < \gamma_{film} + \gamma_{interface}$

This growth mode occurs commonly in nature, it can be found in metal-metal, metal-semiconductor, gas-metal, gas-layer complex systems, etc.

1.2 A Brief Introduction to $In_xGa_{1-x}N$

The ternary indium gallium nitride ($In_xGa_{1-x}N$) is a semiconductor material in the group III-V family composed of x parts Indium Nitride (InN) and (1-x) parts gallium nitride (GaN). It can form in two different structures, Wurtzite and Zinc-Blende, but the wurtzite structure is more thermodynamically stable. It is made up of a hexagonal close packing lattice with an AB atomic repeating pattern. Furthermore, because nitrogen is more electronegative than the other group-V elements, nitride semiconductors have a high degree of ionicity. Crystal structures with a high degree of ionicity are more likely to be wurtzite[43].

1.2.1 Enabling Attributes of $In_xGa_{1-x}N$

- Ternary Wurtzite Indium Gallium Nitride ($In_xGa_{1-x}N$) alloy is a group III-V semiconductor material with a direct bandgap, allowing direct interband transitions to occur without the assistance of phonons[44].
- Because it possesses a direct bandgap, hence, suitable for use in a variety of optoelectronic devices such as light-emitting diodes, laser diodes, and optical communication.

- For Ternary $In_xGa_{1-x}N$ alloy, the lattice constants follow Vegard's law.

  $$a(In_xGa_{1-x}N) = x\ a(InN) + (1-x)\ a(GaN)$$

- The absorption coefficient α(E) as a function of energy in an ideal semiconductor can be expressed as

  $$\alpha(E) = \alpha_o \sqrt{\frac{E - E_g(x)}{E_g(x)}}$$

  Where $E_g(x)$ is band gap of InGaN, E is the energy of photons and α_o is constant, for InGaN, it is assumed to be the same as that for GaN[45] ($2x10^5 cm^{-1}$). InGaN alloys have high absorption coefficient[46].
- The band gap InGaN can be varied from 0.64 eV to 3.42 eV, and this spans about 90% of the visible solar spectrum. Within the first 500 nm thickness of an $In_xGa_{1-x}N$ alloy film, 90 percent of photons lying above the bandgap are absorbed[47].
- The low effective mass of charge carriers in InGaN alloy results in high electron mobility[48]. They also possess high heat capacity, high thermal conductivity, high saturation velocity, and large breakdown voltage[7,49,50].
- They have the ability to endure high levels of radiation while still maintaining their optoelectronic capabilities[49].
- Due to their large absorption coefficients, wide range of tunable bandgap, high saturation velocity, thermal conductivity, and high temperature and radiation resistance, they have huge potential in photovoltaics research and development. Also, they are used in lasers because of their high saturation velocity.
- They have high spontaneous and piezoelectric polarisation, resulting in strong internal fields in the active region, hence quantum wells are utilized to reduce recombination.

- Low pyroelectric coefficients in nitrides, make them suitable for high-power electronics and high-temperature applications[13].
- Large dislocation densities are ignored in $In_xGa_{1-x}N$ alloys because strong internal fields caused by spontaneous and piezoelectric phenomena may counteract the influence of dislocations[51,52].
- Because of the high absorption coefficients, even a thin light-harvesting layer of InGaN alloy in solar applications or photovoltaic systems is capable of capturing photons from solar radiation, lowering the device's production cost and size.

1.2.2 Growth Kinetics of $In_xGa_{1-x}N$

Growing InGaN materials is a challenging process due to the difficulty of producing high-quality InGaN materials: InN and GaN have a large lattice mismatch, resulting in a solid phase miscibility gap[53] and low indium incorporation in the InGaN alloy due to the relatively high vapor pressure of InN[54]. On the growth front, the difference in formation enthalpies for InN and GaN yields a substantial indium surface segregation[55]. However, this is encountered by optimizing growth parameters such as using relatively low growth temperatures, a high V/III flux ratio, a low growth rate, and a low growth pressure.

Piner et al. have grown InGaN by MOCVD and they found that by lowering the growth temperature desorption of indium from the surface was minimized, but the growth rate was reduced due to cracking of ammonia at low temperature and obtained low indium composition in the film. This again leads to the formation of indium clusters. By keeping a large V/III ratio, researchers have achieved suppression of indium segregation while deposition[56]. Kim et al[57] investigated the effect of growth pressure on the incorporation of indium and observed that by decreasing the growth pressure from 250 Torr to 150 Torr the indium incorporation is increased but the crystal quality is reduced as evident by the broadening in the emission spectrum. To overcome the ammonia cracking issue PAMBE is very effective in growing at low temperatures as active nitrogen species are produced by radio frequency plasma source. InGaN grown by MBE has some similarities to MOCVD grown film, like, as substrate temperature is increased the indium incorporation decreased[58–60], but when nitrogen flux and growth temperature are maintained constant and indium and gallium flux are increased in a constant ratio, the indium incorporation is increased at low metal flux. Shen et al.[61] used PAMBE to grow InGaN films on both nitrogen- and gallium-polar GaN buffer layers. There was a difference in film quality between InGaN grown on nitrogen-polar and gallium-polar GaN, with the gallium-polar GaN being superior in structural quality. With this finding, high-quality InGaN films with an indium composition of up to 0.36 were grown on gallium polar GaN, exhibiting intense PL emissions. So, the growth parameters should be optimized for the desired results otherwise they will significantly affect the device properties.

1.3 PEC Water Splitting

Rising energy demand as a result of population increase has resulted in increasing fossil fuel usage and major environmental issues[62]. Currently, most of the world’s energy comes from fossil fuels, which ultimately leads to the depletion of available resources. As a result, forcing humankind to seek cleaner, renewable and sustainable alternative energy sources[63,64]. In this view, hydrogen is ideal energy due to zero carbon emission and its high gravimetric energy density[65,66]. Currently, industrial hydrogen production is primarily accomplished by reforming hydrocarbon steam in fossil energy or coal via reaction to fossil fuels under steam control, which is not only costly but also produces significant emissions[67,68]. As a result, despite the hurdles, the use of renewable energy to create hydrogen is being explored[69]. Solar energy has received a lot of attention in recent years as the world's greatest renewable energy source. If solar energy can be used effectively, it will provide a steady source of electricity in the future[70,71], but the solar power's potential to power a substantial amount of global infrastructure is still a long way off, and thus, there is a lot of research going on to utilize solar energy. One of the ways researchers are using solar energy is to generate hydrogen by splitting water. Again, there are few ways to generate hydrogen but one of them is photoelectrochemical (PEC) water splitting. PEC has the potential to provide considerable conversion efficiency at an affordable cost[72]. Fujishima and Honda discovered PEC water splitting in the 1970s[73], using TiO_2, an n-type semiconductor material with a band gap ~3.2 eV, in contact with an electrolyte. Upon illumination of light, TiO_2 absorb photons and generate enough potential to split the water molecule into oxygen and hydrogen, storing solar energy in chemical bonds[74]. Since realizing this, it has received lot of interest in the research community.

1.3.1 Working principle

In PEC water splitting, a semiconductor photoelectrode is immersed in an electrolyte solution. Upon illumination of light on the electrode, it absorbs photons with energy higher than its bandgap, exciting electrons from the valence band to the conduction band and consequently creating electron-hole pairs. These photogenerated charge carriers will be separated by applied bias. If we consider an n-type semiconductor photoelectrode, the photogenerated carriers within the space charge region will be driven by the electric field away from the interface of the semiconductor and electrolyte. When light is incident on the photoelectrode the Fermi level raises, resulting in a decrease in the band bending and splitting into a quasi-Fermi level for electrons and close to the interface for the holes. These excited electrons move through the ohmic contact towards the counter electrode, typically the platinum electrode, where they reduce water to hydrogen. Water reacts with semiconductor surface holes, (OH^-) diffuses back to react with holes at the photoelectrode's surface resulting in oxidizing the holes to oxygen. Generally, overall water splitting consists of two half-reactions: reduction of protons (Hydrogen Evolution Reaction or HER) and oxidation of water (Oxygen Evolution Reaction or OER).

The Hydrogen Evolution Reaction (HER) and Oxygen Evolution Reaction (OER) in a PEC cell with an acidic electrolyte are as follows:

$$4h\nu \rightarrow 4e^- + 4h^+$$

HER: $4H^+ + 4e^- \rightarrow 2H_2$, at $E^o_{H^+/H_2} = +\,0.00\ V_{NHE}$

OER: $2H_2O + 4h^+ \rightarrow 4H^+ + O_2$, at $E^o_{H_2O/O_2} = -1.23\ V_{NHE}$

For an alkaline electrolyte, the dissociation reaction of water produces hydroxyl anions; the reduction and oxidation reactions are written as[75]:

HER: $4H_2O + 4e^- \rightarrow 2H_2 + 4OH^-$, at $E^o_{H_2O/OH^-} = -0.828\ V_{NHE}]$

OER: $4OH^- + 4h^+ \rightarrow 2H_2O + O_2$, at $E^o_{O_2/OH^-} = +0.401\ V_{NHE}]$

Where, NHE is Normal Hydrogen Electrode, which is the potential of a platinum electrode in 1M acid solution, E_o is a measure of the tendency of any chemical substance to lose or gain electrons.

The overall water splitting reaction is given by the following reaction

$$2H_2O + 4h\nu \rightarrow 2H_2 + O_2$$

The number of photons absorbed equals the number of produced electron-hole pairs, which is twice the number of produced H_2 molecules and four times the number of produced O_2 molecules. PEC water splitting is an endothermic process, requiring a Gibbs free energy of

273.2 kJ mol^{-1}, or 1.23 eV per electron transferred[72] at 25 ^{o}C and 1 atm pressure, which is thermodynamically unfavorable and necessitates the use of external energy to overcome the reaction energy barrier. In practice, hundreds of millivolts of overpotential are required to drive the water-splitting reaction. Owing to the overpotentials associated with water oxidation, as well as the counter electrode overpotential, charge transport in the electrolyte and in the photoelectrode, the distance between the electrodes, and the geometry of the device, play a crucial role.[76]

1.3.2 Required criteria for photoelectrode

The semiconductor electrode for water splitting has to meet several criteria for better efficiency such as material should possess strong absorption of visible light, band gap should straddle with the reduction and oxidation potential of water, should be stable in electrolyte solution for longer duration, kinetic overpotential for oxidation and reduction reactions should be low, and the material should be earth abundant and cost effective[77,78].

The bandgap energy of a semiconductor is the basic characteristic that governs the spectral range in which it absorbs light. Because just 1.23 V is required for water splitting, a bandgap of 1.23 eV may be sufficient. A semiconductor with such a bandgap would have a maximum total solar-to-hydrogen conversion efficiency of 47.4 % based on the standard AM 1.5 G solar spectrum (100 mW/cm^2), assuming no losses[79]. Unfortunately, important back processes such as thermodynamic losses (0.3–0.4 eV) and overpotentials required for guaranteeing sufficiently fast reaction kinetics (0.4–0.6 eV)[80] are involved during solar water splitting. As a result, the semiconductor must have a bandgap of at least 1.9 eV, which corresponds to an absorption onset of around 650 nm[78]. Typically, preferred band gap values for better solar to hydrogen efficiency are between 1.9 to 2.4 eV. In direct contact with the electrolyte in the dark and under the illumination of light, the semiconductor must have high chemical stability. It is observed that in general, the stability against corrosion increases with the band gap but that limits the absorption of light. To overcome this kind of issue, the idea of deposition of a thin coating of passivation layer has been used. The band edge positions of the semiconductor must straddle with the reduction and oxidation potentials of the water.

However, due to the severe conditions outlined above, no semiconductor material has been singularly identified that promotes unbiased water splitting, high solar-to-hydrogen conversion efficiency, and long-term stability. Metal oxides like TiO_2, $BiVO_4$, Cu_2O, etc, and non-oxides like Si, GaAs, CdS, GaP, etc. have been investigated extensively, especially oxides since they show good stability in general and relatively cost less. Turner et al[81] reported solar to the hydrogen conversion efficiency of 12.4% in p-$GaInP_2$/pn-GaAs system, as one of the best-reported values but these cells are expensive to produce, due to pn-GaAs substrates.

1.3.3 Semiconductor Liquid Interface

When a semiconductor photoelectrode is immersed in an electrolyte solution it undergoes equilibration, the electrons will move between the semiconductor and redox couple in the solution. As a result, the space charge layer, Helmholtz layer, and the Gouy-Chapman layer will be present at equilibrium. A space charge layer will be built in the semiconductor. In case of an n-type semiconductor, electrons are the majority carriers and a few of these excess electrons diffuse into the electrolyte solution as a result, a positively charged ionic region will be formed, called as depletion region. In case of a p-type semiconductor, electrons diffuse into the semiconductor and accumulate at the surface and the latter formed is known as the accumulation layer. The formation of these layers leads to local polarisation and band bending at the interface. Inner and outer Helmholtz planes make up another layer. For example, the inner Helmholtz plane represents ions that have been specifically adsorbed; the outer Helmholtz plane represents a region of solvated ions that are closest to the surface, Helmholtz layer width is usually smaller compared to the space charge layer width[82]. Gouy-Chapman layer is a diffuse region where one charged species exists in a higher concentration than that of the opposite charge species in the solution.

1.3.3.1 Band bending

When it comes to photoelectrochemical reactions, band bending in the space charge layer is critical for better performance. Once equilibrium is achieved between the semiconductor and electrolyte, the Fermi level is positioned at the same level as the redox potential of the electrolyte solution. Figure 1.6 Illustrates different scenarios for an n-type semiconductor. No band bending occurs if the Fermi level of semiconductor and redox potential are equivalent, as there is no net charge transfer. This scenario is known as flat band potential. When the potential falls below that of the flat band due to electron injection, the bands bend downwards[83], forming an accumulation layer. In other scenarios, the bands bend upwards, forming a depletion layer. There is a net flow of electrons into the electrolyte when the Fermi level of the semiconductor is larger than the redox potential of the electrolyte. As a

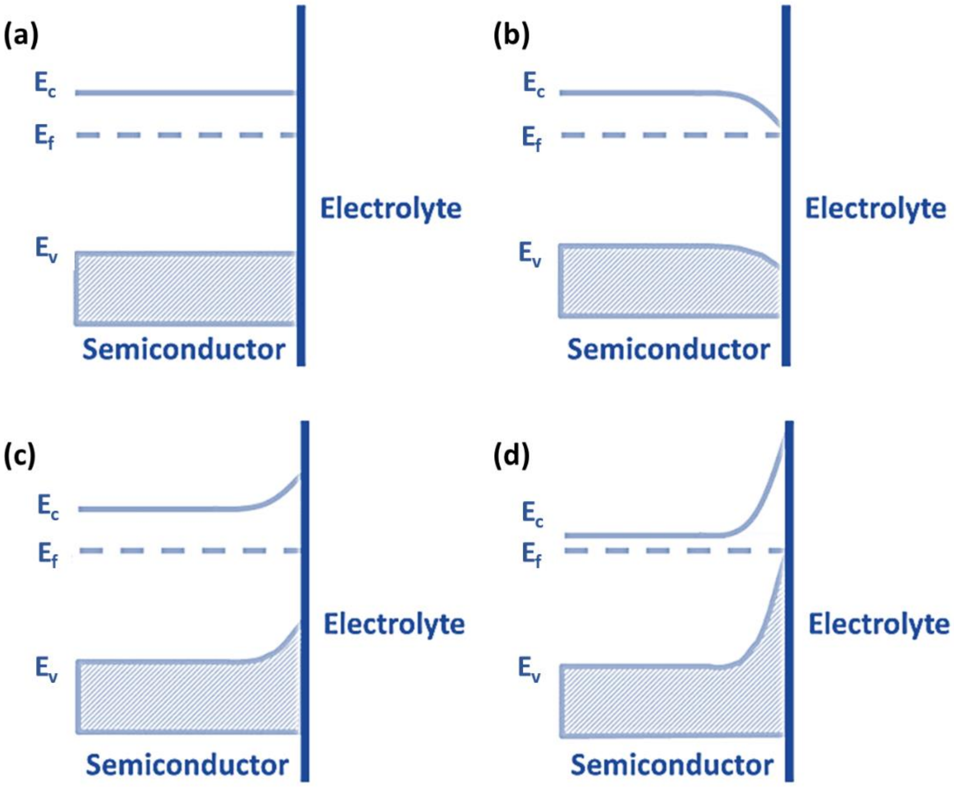

Figure 1.6 n-type semiconductor band structure in an electrolyte (a) equivalent Fermi level and redox potentials (b) Fermi level of semiconductor < redox potential (c) Fermi level of semiconductor > redox potential (d) Fermi level of semiconductor >> redox potential.

result, electrons are depleted on the semiconductor surface, and the bands of an n-type semiconductor rise upward. Because there aren't enough charge carriers in a depletion region, electron-transfer processes are slow. An inversion layer will emerge if a large force is applied to the system to extract electrons from both the valence and conduction bands of the electrode. In the space charge region, sufficient electron removal at the semiconductor's surface leads the semiconductor type to invert[83]. As a result, at the interface, n-type semiconductors will become p-type. An accumulation of electrons and holes facilitates reduction and oxidation reactions in n-type and p-type semiconductor electrodes, respectively.

1.3.3.2 Fermi level pinning

In semiconductor photoelectrodes, Fermi level pinning is a typical occurrence due to the presence of surface states. When the photoelectrode is immersed in a solution, the surface states form due to surface defects that can get charged. Over a specific potential range, charging the surface states maintains the band bending within the space charge layer. Thus, given a photoelectrode with varying applied voltage, the band bending will remain constant throughout a specific region. The performance of the electrode is influenced by the number of surface states and their respective energy levels[84].

1.3.4 III-Nitrides photoelectrodes

Metal oxide semiconductors have typically been preferred for solar water splitting due to their inherent stability in aqueous solutions and typically reasonable performance. III–V semiconductors have been extensively explored for solar cell applications (e.g., GaAs). However, they have certain disadvantages like a large band gap and poor absorption of light, which is required for a photoelectrode to be employed in solar water splitting. A notable exception to this is seen in III-nitride semiconductors. GaN, for example, is discovered to be very stable in water, acids, and bases[19]. Furthermore, because the N 2p orbital is more negative than the O 2p orbital, nitride semiconductors can have smaller band gaps by alloying that can be tailored to straddle the water splitting potentials (redox potential) and the full solar spectrum[85], as we can see from Figure 1.7 with highlighted in the red dotted box for III-nitrides.

Turner et al from NREL, USA, presented GaN as a PEC photoelectrode for the first time in 1995[86], and since then, a lot of work has gone into understanding the PEC performance of GaN-based electrodes. Fujii et al. reported the production of H_2 on a Pt counter electrode with an n-type GaN working electrode under external bias[87] and the effect of indium composition on GaN PEC characteristics was explored further[88] in the year 2005. InGaN semiconductors, especially with nanostructures, are contributing to PEC water splitting in improving the performance since the presence of dislocations and piezoelectric polarization fields can be minimized because of the small lattice mismatch. Thus, it can reduce optical losses, enhance carrier separation, and increase surface area. When compared to the flat films,

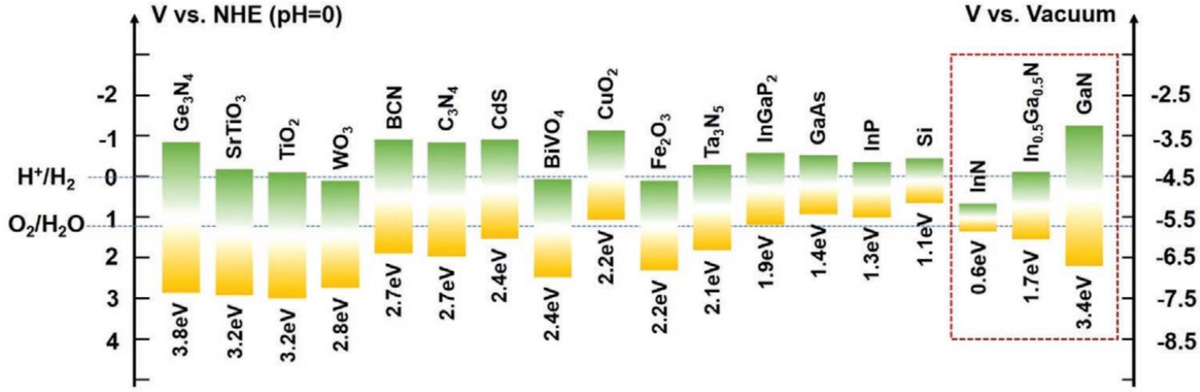

Figure 1.7 Band edge position of some typical photoelectrode materials w.r.t. water redox potential against NHE at pH 0 and vacuum level, also band edge positions of III-nitrides are highlighted[89]*. (© wiley. Reproduced with permission. All rights are reserved.)*

GaN nanostructures such as GaN nanorod arrays, GaN nanopillars, GaN nanowall network, and InGaN/ GaN MQW nanopillars have shown a several-fold, increase in photocurrent density[90–92]. In addition to the nanostructure, the band gap can be tuned from 0.64 to 3.4 eV by incorporating indium in GaN to get the desired bandgap. Theoretically, the estimated maximum solar to hydrogen conversion efficiency is reported to be approx. 27% for the 50% of In concentration which also straddles with the redox potential of water and corresponds to 1.77 eV bandgap, giving InGaN an upper hand over other materials [93–97]. It also shows better stability in acids and neutral pH solutions. Despite these advantages, it still encounters issues such as carrier recombination, and high dislocation densities[98,99], which lead to the Fermi level pinning effect on its large surface area[100,101]. These lead to poor PEC performance of InGaN.

Different configuration of electrodes is also investigated. For instance, Kibria et al.[102] demonstrated MBE-grown catalyst-free InGaN/GaN multiband nanowire heterostructures. Photo deposition of Rhodium (Rh)/Chromium-Oxide (Cr_2O_3) core-shell nanoparticles was used to decorate InGaN/GaN nanowires. This heterostructure provided stable hydrogen generation from pure water splitting (pH 7.0). The use of photo-deposited Rh/Cr_2O_3 nanoparticles enhances the forward reaction of H_2O reduction while suppressing the backward reaction of H_2O formation from H_2 and O_2 on the Rh core. Rh/Cr nanoparticle co-catalysts could nearly double the photocatalytic activity of InGaN/GaN nanowire heterostructures. The better performance was observed due to reduced recombination and better charge carrier separation. Ebaid et al.[103] used InGaN/GaN multiple quantum well (MQW) nanowire heterostructures as a photoanode grown by using MOCVD. They observed a 5-fold enhancement in photocurrent density in InGaN/GaN MQW NWHs compared to bare GaN

NWs, due to increased absorption of light. A threefold increase in the generation of molecular hydrogen was also obtained. Li et al.[104] investigated PEC properties on varying indium composition in $In_xGa_{1-x}N$ epilayer with x=0.2 and 0.4. They observed the high photocurrent density in case of InGaN with the highest indium concentration compared to the one with low indium, due to better absorption of light. Similarly, many researchers reported enhancement in PEC performance of photoelectrodes with different morphology due to their large active surface area, such as, nanopores[105], nanocones[106], nanowall network[107], nanocolumns[108], nanopyramids[109], etc.

Our group had extensively worked and investigated the properties of nanostructures of GaN on Si as well as on Sapphire substrates. Among those nanostructures, GaN nanowall network (NWN) is studied extensively. It is a well-connected GaN nanowall network with single-phase and epitaxial in nature with a large surface area that is grown spontaneously without any use of a catalyst. This morphology has shown very interesting properties for use as a SERS substrate for biochemical sensing. The properties that depended on bandgap engineering made us curious to explore its photoelectrochemical by growing InGaN nanowall network with high indium composition, and its interface with other relevant thin films motivated us to undertake this exploration.

Chapter 2
Experimental Details

Since the motivation of the work discussed in the thesis is to study the dependence of the properties of InGaN films with various growth parameters, we use the sophisticated MBE for film growth, and later characterized by several other techniques. This chapter deals with the basic information of the various experimental methods and the physical basis of the instruments used for both synthesis and characterization.

This chapter is organized as follows: first, the thin film growth methods used, namely the Plasma Assisted Molecular Beam Epitaxy (PAMBE), Atomic Layer Deposition (ALD), and Physical Vapor Deposition (PVD) are discussed in detail. Next, the characterization techniques used in the thesis are explained. For morphological and structural characterization, Field Emission Scanning Electron Microscopy (FESEM) and High-Resolution X-ray Diffraction (HRXRD) are used and for optical characterization Cathodoluminescence (CL), Photoluminescence (PL) and UV-Vis-NIR Absorption Spectroscopies are used. For analyzing the chemical state of the elements and to determine the Fermi level of the semiconductor, X-ray Photoelectron Spectroscopy (XPS) is used. Hall Effect measurement system is used to determine the mobility and concentration of the majority carriers, and a Photoelectrochemical cell with a source meter is used to study the photoelectrochemical properties of the grown films as electrodes.

Thin film growth:

The PAMBE system is the primary growth technique used to grow III-Nitride thin films. The ALD system is employed to deposit titanium dioxide thin films, and to deposit metal ohmic contacts for device fabrication, a high-vacuum PVD system is used.

2.1 Plasma Assisted Molecular Beam Epitaxy (PAMBE)

The word epitaxy comes from a Greek (epi- above and taxis- in ordered manner), which means deposition of a single crystalline film on a single crystalline substrate so that a geometrical relationship between the two respective unit cells is established. Such deposited films are called as epitaxial films or epitaxial layers or epilayers. Epilayers can be grown by using precursors that are in the form of either gas, liquid, or solids. In epitaxial growth, the layer which can be deposited on a substrate material of the same or different composition, which are called homoepitaxial or heteroepitaxial growth processes, respectively.

MBE was developed in the 1960s in Bell Laboratories[110], which contributed significantly to the fabrication of tailored compound semiconductor structures with the precision of an atomic layer. The demonstration of a blue-violet laser diode fabricated by using MBE in Sharp Laboratories in 2004[111] showed the potential of MBE to compete with the MOVPE technique also for commercial applications. However, for industrial III-V epitaxy, MOVPE has advantages due to its versatility for the gas sources, its large range of controllable growth rates and its high productivity with high uniformity attained during deposition on large surface areas. In contrast, MBE has the upper hand over the other important growth techniques, since it is operated in an ultrahigh vacuum (UHV) environment that is favorable to in-situ growth analytics, less consumption of the source materials, and its ability for precise control of deposition rate. This effective as a research growth tool, is independent of the use of precursors. The growth temperature of MBE is usually low due to non-dependent on precursor cracking.

Figure 2.1 (a) and (b) show a photograph of Plasma Assisted Molecular Beam Epitaxy (PAMBE) growth system manufactured by SVTA, USA. in our laboratory and the schematic diagram of the growth chamber of the MBE system, respectively.

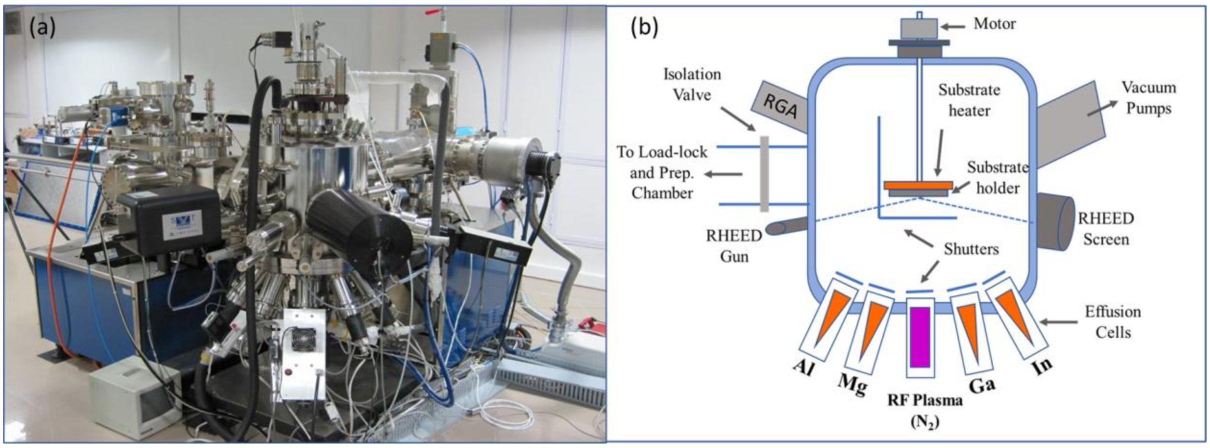

Figure 2.1 (a) A photograph of PAMBE system by SVTA,USA used in this work, (b) Schematic diagram of PAMBE growth chamber.

The system is evacuated by different vacuum pumps like turbo, cryo and ion pumps (turbo and cryo pumps exclusively during the growth) which are connected to the growth chamber for achieving UHV condition (10^{-11} torr), as measured by an ion gauge placed inside the growth chamber. Loading and unloading of the substrates are carried out through a load-lock system equipped with a turbo molecular pump. All the substrates are chemically pre-cleaned using acetone and then isopropyl alcohol (IPA) before being introduced in the load-lock chamber. The preparation chamber has a water-cooled substrate heating/degassing facility, where the temperature of the heater goes up to 700 ˚C. The main chamber where growth takes place, consists of a cryo-panel around it, which is cooled by liquid nitrogen during growth to prevent degassing of atoms from the walls of the chamber, which also acts as a cryo pump. The heater, attached with the growth manipulator, can achieve the temperature up to 1200 ˚C at the substrate, mounted on a manipulator is cooled by water circulation. The rotation of the growth manipulator is controlled by the magnet assembly attached to a motor which is equipped with an ON/OFF switch, with an option to select clockwise and counterclockwise rotation. Active nitrogen radicals are generated by a radio frequency inductively coupled plasma source. Group-III metals (In, Ga and Al) and dopants (Si and Mg) are supplied by effusion cells and their fluxes are controlled by the temperature of the cells. Shutters placed in front of the opening of effusion cells permit direct control of the epitaxial growth surface at a monolayer level by changing the incoming beam with the opening and closing of the shutter. Growth can be monitored in-situ by a Reflection High Energy Electron Diffraction (RHEED) system. Up to 3-inch substrate can be mounted on the growth stage, achieving a growth uniformity of better than 1% over the diameter of 2.8 inch. The growth temperature is monitored by a thermocouple, which is calibrated using a pyrometer. The growth temperature, metal flux-rate, plasma power and nitrogen flowrate, all these together determine the growth rate and the morphology of the films being grown. The operation of the MBE system can be carried out through the panel control board as well as computer automation. In case, any part of MBE is reassembled for troubleshooting or any other purpose, the system has to be baked at 150 ˚C for at least 48 hrs to remove water vapors and other contamination, before film deposition.

2.1.1 Effusion Cells

To furnish Group-III metal flux, water-cooled standard effusion cells (Knudsen Cells or, more generally known as K-cells) are utilized. An effusion cell consists of a radiatively heated crucible containing the solid or liquid evaporant. To prevent magnetic interference with electron diffraction facilities in the MBE system, the electrically insulated heater filaments are wound non-inductively, either spirally or end-to-end. The temperature of the source material is measured by a thermocouple that is precisely positioned to ensure intimate contact with the crucible. After flux calibration, the source temperature can be employed to keep the flux rate constant, albeit periodic recalibration is required due to source material depletion, charge material redistribution, and changes in the thermal environment. The K-cells are composed of pyrolytic Boron Nitride (PBN) crucibles and high purity (99.9999 %) metal ingots. All effusion cells were momentarily degassed to roughly 10% above the maximum intended operating temperature after being loaded with metal. Flux gauge is used to calibrate flux from effusion cells, where the change in metal BEP corresponds to the change in K-cell temperature. The temperature of the water is kept at 16 ˚C by a chiller, and the cold water is circulated around the K-cells to remove surplus heat during growth.

2.1.2 Nitrogen Plasma Source

Since nitrogen is inert at the temperatures required for development, the N2 molecule must be activated by a plasma or ion source. A radio frequency inductively linked plasma source was used as the principal source in this study (RF-4.5 by SVTA). Figure 2.2 depicts the basic structure of an RF plasma source. An inductively coupled plasma source is essentially a multi-turn copper coil with cooling water running through it to dissipate the heat generated during the operation. The induction plasma is formed inside a confinement tube, which in our instance is made of pyrolytic Boron Nitride (PBN). The plasma is maintained on a continuous gas flow, thus one end of the PBN tube is open. A 0–10 sccm (standard cubic centimetres per minute) mass flow controller controls the flow of ultra-high pure (99.9995 %) nitrogen gas into the cavity via the inlet. The generator provides an alternating current (ac) of radio frequency (RF) to the copper coil during induction plasma operation, and this ac generates an alternating magnetic field inside the coil, according to Ampere's law (for a solenoid coil): $\varphi_B = \mu_0 I_c N \pi r_0^2$, where φ_B is the magnetic field flux, μ_0 is the permeability constant (4π x 10^{-7} Wb/A.m), I_c is the coil current, N is the number of coil turns per unit length, and r_0 is the coil turns' mean radius. The alternating field accelerates charged particles, causing them to collide with other species and form plasma. A change in magnetic field flux induces a voltage, or electromagnetic force, according to Faraday's Law: E = N(dφ/dt), where N is the number of coil turns and the item in bracket represents the rate at which the flux is changing. Because the generated plasma is conductive, the electromagnetic force, E, will drive a current in closed loops to resist the magnetic field change. According to Ohm's Law, the energy transmitted to the plasma is dissipated via Joule heating, which is analogous to heating a metal rod in an induction coil. In practise, plasma ignition under low pressure conditions (< 300 torr) is nearly spontaneous, and a stable induction plasma is created once the RF power applied on the coil reaches a particular threshold value (depending on the source configuration, gas flow rate, etc.). In the case of atmospheric ambient pressure conditions, ignition is frequently achieved with the help of a Tesla coil, which produces high-frequency, high-voltage electric sparks that induce local arc-break inside the source and stimulate a cascade of plasma gas ionisation, eventually resulting in a stable plasma.

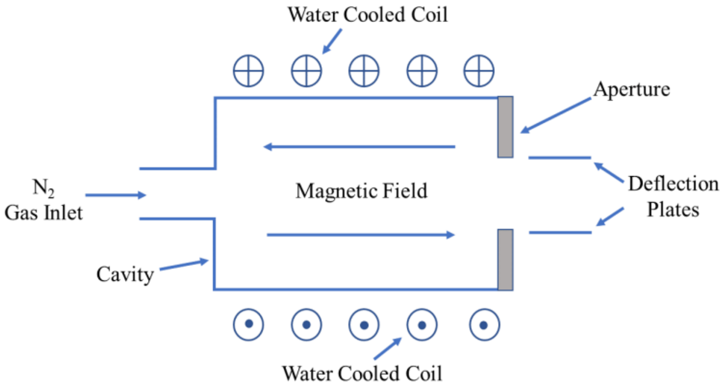

Figure 2.2 Schematic diagram of radio frequency inductively coupled plasma source.

For the growth of our films, the source was typically operated at RF powers of 300–400 W and a flow rate of 1–8 sccm. At different plasma operating conditions and from different source geometries, the species created by an RF plasma source can vary significantly. A deflection plate is also included in the plasma source, which is utilised to deflect charged species as needed.

2.1.3 Residual Gas Analyzer

A Residual Gas Analyzer (RGA) is a quadrupole mass spectrometer connected directly to a vacuum system and its function is to analyse the gases inside the vacuum chamber[112]. It uses the difference in mass-to-charge ratio (m/q) of ionized molecules or atoms to separate them from each other. Again, the quadrupole probe consists of three parts as shown in the Figure 2.3 which are: the ionizer, the quadrupole filter, and the ion detector. All these parts are housed in the vacuum space where the gas analysis is carried.

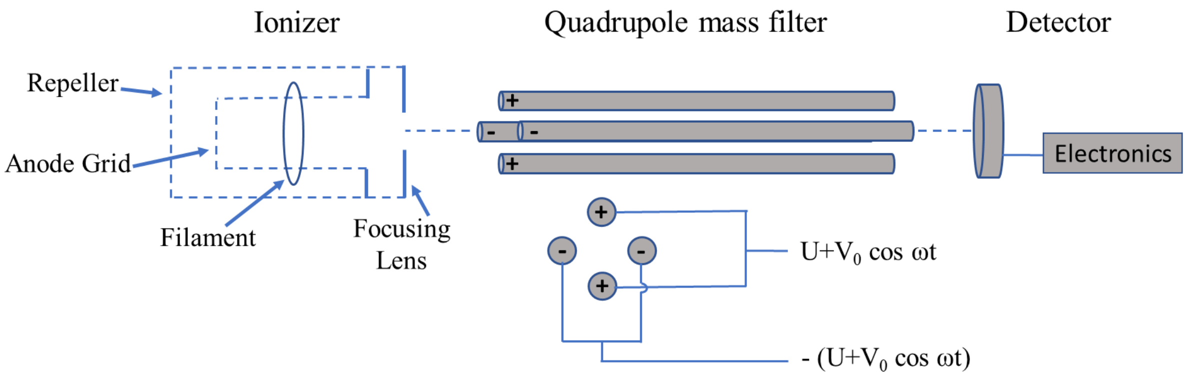

Figure 2.3 Schematic representation of main components of residual gas analyser.

In the Ionizer region, the filament is resistively heated to emit electrons, which are then accelerated towards the anode grid cage with a wire mesh design. As a result, most electrons do not strike the anode right away, but instead pass through the cage, where they make ions via electron impact ionisation, and so tend to stay within the anode grid structure once the ions are formed. The focus plate is kept at a negative potential (relative to ground) and draws the ions out of the anode cage into the filter section. The ionizer's repeller, which entirely encloses it, is biased negative in relation to the filament, preventing electron loss from the ion source.

The quadrupole mass filter's general principle of action can be qualitatively depicted as follows: One rod pair (X-Z plane) is connected to a positive DC voltage, which is then overlapped with a sinusoidal RF voltage. The opposite rod pair (Y-Z plane) is connected to a negative DC voltage, which is then superimposed with a sinusoidal RF signal that is 180 degrees out of phase with the first set of rods. The potentials are represented by the expression: $\mathbf{V_{x/y} = +/- (U + V_0 \cos\omega t)}$ where U is the magnitude of the DC voltage applied to either pair of rods, V_0 denotes the amplitude of the RF voltage applied to either pair of rods, and ω is the RF's angular frequency (= 2πf). The alternating component of the field can be followed by light ions (low m/q ratio). In the X direction, those ions will remain in phase with the RF drive, gain energy from the field, and oscillate with increasing amplitudes until they encounter with one of the rods and are discharged. As a result, the X axis is a high-pass mass filter: Only high masses will pass through the quadrupole's other end without impacting the X electrodes. Heavy ions will be unstable in the Y direction due to the DC component's defocusing impact, while some lighter ions will be stabilised by the alternating component provided its magnitude and amplitude are such that it corrects the trajectory anytime its amplitude starts to increase. As a result, the Y direction acts as a low-pass mass filter, allowing only low masses to pass to the other end of the quadrupole without colliding with the Y electrodes. The combination of the two directions yields a mass filter appropriate for mass analysis: The filter can be configured to discriminate against both high and low mass ions to the required degree by selecting an appropriate values of RF/DC ratio. The mass of the ions that follow stable trajectories down the filter is determined by the magnitude and frequency of the RF voltage. Heavy ions begin to oscillate in phase with the RF as the RF amplitude increases, colliding with the rods. The filter selectivity is determined by the DC/RF ratio value. The negative DC component defocuses heavier ions as the DC increases (at constant RF).

In detector part, positive ions that pass through the quadrupole successfully are redirected towards the detector by an exit aperture that is held at ground potential. The detector measures ion currents directly (Faraday Cup) or an electron current proportional to the ion current using an optional electron multiplier detector and converts the measured current into an equivalent partial pressure. The operation of RGA is controlled by the ECU, which handles the data and transmits it to the computer to carry out analysis and to display. RGA (from Stanford Research Systems) attached to our system can monitor gaseous species up to 200 a.m.u.

2.1.4 RHEED

Reflection High Energy Electron Diffraction (RHEED) is a very powerful *in-situ* real time characterization technique to monitor growth of thin films[113]. We have a STAIB RHEED set up attached to our MBE system. It consists of a high energy electron gun with a focused beam energy of 8 kV and a phosphor coated screen with a camera on the other side of the growth chamber to capture the RHEED patterns, shown in the Figure 2.4a. This technique makes use of the high energy electron beam's grazing angle (1 – 4°) incidence (Figure 2.4(a)), in which the electron's wavelength is comparable to typical atomic spacing (Approx. 0.1 - 1 nm), making it a surface sensitive tool. Within the initial few nanometres of the film and interface, electrons scatter constructively and destructively off different atomic planes, forming a diffraction pattern on the phosphor screen. The structural and morphological features of the developing crystal can be monitored in real time using this diffraction pattern.

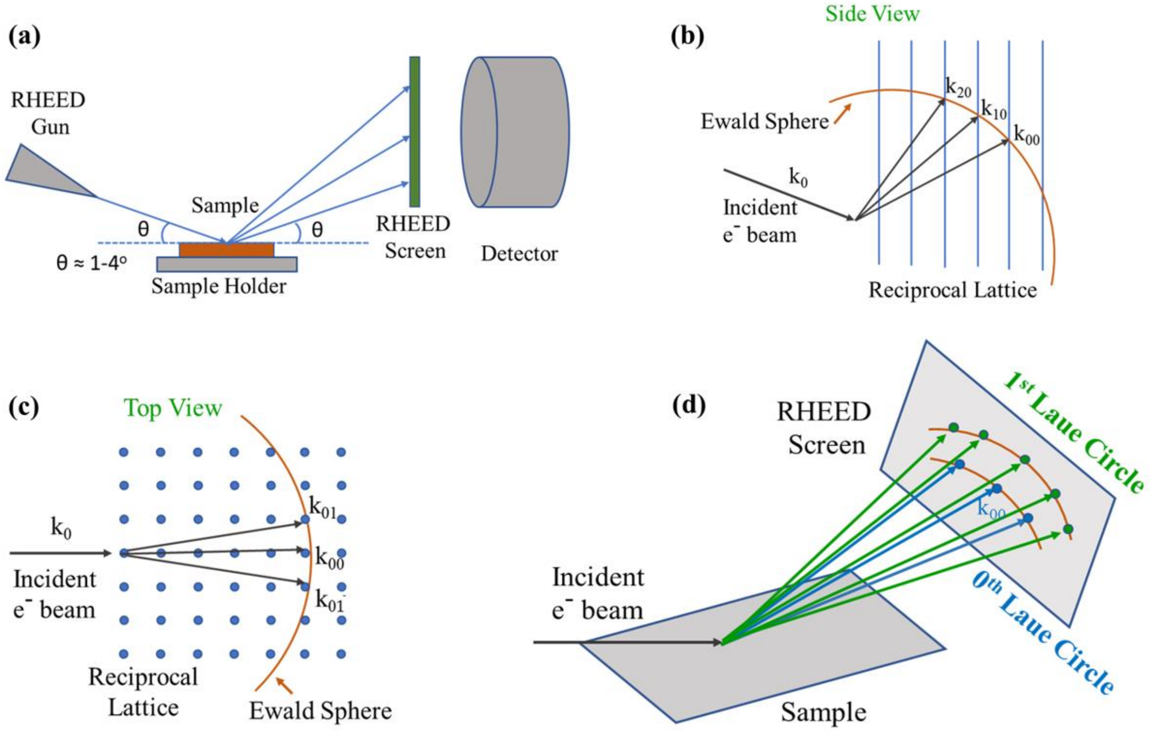

Figure 2.4 (a) Schematic RHEED system. (b) and (c) side and top view of RHEED construction of the Ewald's sphere at sample surface. (d) Laue pattern formed on the phosphor screen of RHEED during experiment.

As the spots of a perfect pattern to the Ewald's sphere are related to the reciprocal lattice of the sample surface, the construction of Ewald's sphere is used to identify the crystallographic properties of the sample surface[114]. Bulk crystals' reciprocal lattices are consisting of a series of points in three-dimensional space. In RHEED, however, only the first few layers of the material contribute to diffraction, therefore no diffraction conditions exist in the dimension perpendicular to the sample surface. The reciprocal lattice of a crystal surface is a sequence of infinite rods extending perpendicular to the sample's surface due to the lack of a third diffracting condition. With a radius equal to the reciprocal of the incident electrons' wavelength, Ewald's sphere is centred on the sample surface. Where the reciprocal lattice rods touch Ewald's sphere as shown in Figure 2.4b, diffraction conditions are satisfied.

The RHEED system is built in such a way that only low orders of diffraction are incident on the detector, despite the fact that many reciprocal lattice rods meet the diffraction criteria. The intersections that form the shortest angle with the sample surface and have the maximum intensity are referred to as 0th order beams. A higher order reflection is defined as the intersection of a rod and a sphere that is more away from the sample surface. Because the incident beam has a very short wavelength due to its high-energy electrons, the radius of Ewald's sphere is much larger than the spacing between reciprocal lattice rods, and as a result, rows of reciprocal lattice rods actually intersect the Ewald's sphere as an approximate plane, shown in the Figure 2.4c.The Figure 2.4d shows Laue circles are formed by the intersections of these effective planes with Ewald's sphere. The RHEED pattern is a collection of points on the perimeters of concentric Laue circles over the centre point. Yet, Interference effects between diffracted electrons, on the other hand, produce strong intensities at single spots on each Laue circle.

In RHEED, reciprocal lattice streaks and Kikuchi lines dominate the pattern of single crystalline surfaces. Film/substrate blockage is shown by the shadow edge. The separation between this and a direct beam indicates the angle of incidence of the beam. The roughness of the growth front can be gauged by the appearance of the streaks in the patterns[115]. On a nm scale, the streaky RHEED pattern indicates the film's smoothness, and the patterns are entirely attributable to diffraction or reflection. If, on the other hand, the pattern appears spotty, it implies that there is roughness on the nm scale, in which case some electrons are transported through three-dimensional surface features, resulting in an interference pattern. The growth rate can be estimated using RHEED intensity oscillations, the period of which corresponds to the growth of one monolayer.

In this thesis, RHEED technique is mainly used to determine the single or poly crystalline nature of the film surface and to know whether the surface of grown film is either atomically flat or rough.

2.2 Atomic Layer Deposition (ALD)

Process of Atomic Layer Deposition (ALD) concept was first proposed by Prof. V.B. Aleskovskii in 1950s in the Soviet Union[116]. Later, in 1970s in Finland, Prof. Tuomo Suntola and his colleagues invented ALD technology[117]. With the ability to control layer thickness and composition at the atomic level, ALD is regarded as one of the most promising deposition methods for creating ultra-thin, conformal coating on substrates/films, hence ALD process is very much useful in fabrication of microelectronics to deposit thin and high-k (high-permittivity) gate oxides.

To deposit a film using ALD technique, there are four important phases in an atomic layer deposition cycle. First, exposure of precursor. Second, purging of the precursors or any by-products present in the growth chamber. Third, Exposure of reactant species such as oxidants or reagents. And fourth, Purging of reactants and by-products molecules from the growth chamber. The growth cycles are repeated until the desired film thickness is achieved. Typically, a reaction cycle in the synthesis of binary compounds such as metal oxides consist of two reaction stages. The metal compound precursor is permitted to react with the surface in one step and with the oxygen precursor in the other. Between each step, a purge is carried out to remove any excess precursor or reaction by-products.

Gases, volatile liquids, or solids can all be used as ALD precursors. The vapour pressure must be sufficiently high to facilitate mass movement and chemical reaction; all solid and some liquid precursors must be heated to achieve the optimal vapour pressure. Metal precursors such as halides, especially chlorides, alkyl compounds, and alkoxides are often used in ALD. Organometallic compounds such as cyclopentadienyl complexes and alkyl and silyl amides have received more interest in recent years[118]. Water, hydrogen peroxide, and ozone are utilised as nonmetal precursors for oxygen; hydrides are used for chalcogens; ammonia, hydrazine, and amines are used as nonmetal precursors for nitrogen; and hydrides are used for group V elements[119].

Figure 2.5 A photograph of Beneq TFS-200 ALD system installed at JNCASR, Bengaluru, India

Our institute is equipped with a Beneq TFS-200 ALD system manufactured by Beneq Oy of Vantaa, Finland, Shown in the Figure 2.5. It features three distinct modes of material deposition: thermal, remote plasma, and fluidized bed reactor (FBR), as well as an ozone generator that allows for the use of ozone as a co-reactant in place of any oxygen source. We have used this deposition technique to grow Titanium dioxide (TiO_2) to form heterostructure with nitride films.

2.3 Physical Vapor Deposition (PVD)

Physical Vapor deposition is one of the methods for depositing thin films in which the source material is transformed to its vapour phase and then re-condensed onto a substrate for film formation. To obtain the vapour phase, a variety of techniques are used such as sputtering, evaporation, and laser ablation. We have used a PVD system which is kept at high vacuum ($\approx 10^{-8}$ torr) to maintain purity of chamber, to deposit films using thermal evaporation and electron beam/e- beam evaporation methods, equipped in our laboratory supplied by SVTA, USA. The PVD system employed in this work is depicted in the Figure 2.6a, along with schematic diagram of e-beam evaporation set up present inside the system (Figure 2.6b).

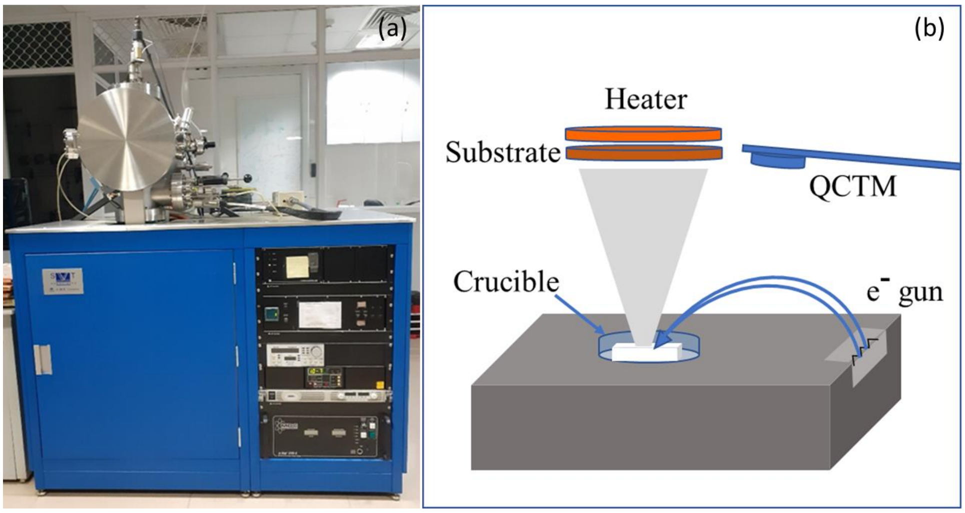

Figure 2.6 (a) A photograph of PVD system by SVTA, USA, at JNCASR, Bengaluru. (b) Schematic diagram e-beam evaporation set up.

Electron beam evaporation is an excellent technique for depositing materials with a high melting point such as Titanium, Platinum etc. During deposition the material is placed in a crucible and the substrate is positioned above it with the substrate facing the crucible as shown in Figure 2.6b. By heating a filament, an electron gun generates a beam of electrons that are subsequently accelerated to high energies using a 5.5 kV potential. The electron beam is guided onto the material inside the crucible using a magnetic field. Graphite, tungsten, and molybdenum etc can be used as crucibles depend on the material of interest to be deposited. The real time thickness of the sample is determined by a quartz crystal thickness monitor (QCTM) which is attached inside the chamber. It utilises a piezoelectric quartz crystal that oscillates when subjected to an alternating voltage. The deposition of a thin layer on a quartz crystal alters its resonance frequency, which can be used to determine its thickness.

In this thesis, PVD system was largely employed to deposit metal contacts such Titanium, Indium and Aluminium, onto the samples deposited by PAMBE.

2.4 Field Emission Scanning Electron Microscope

To analyse surface morphology of deposited films, FESEM is used[120]. Figure 2.7 shows the schematic representation of FESEM. A typically it consists of an electron gun as a source of electrons, a column of condenser lenses to regulate the intensity of the electron beam and direct it onto the specimen, and a detector that detects the secondary electron generated by the bombardment of high energy electron beams and produces the image.

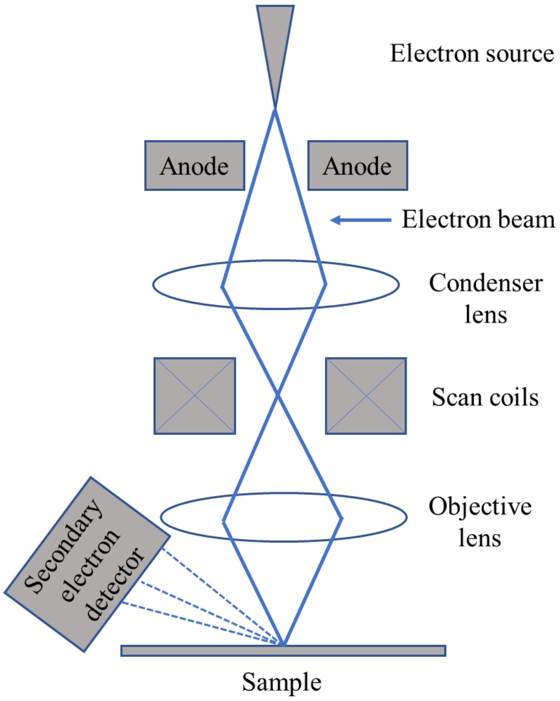

Figure 2.7 Schematic diagram of Field Emission Scanning Electron Microscope

In standard electron microscopes, electrons are generated by heating tungsten (W) filament over more than 2000 ^{o}C by passing electric current and these microscopes have less resolution. In a situation like mounting a lanthanum hexaboride (LaB6) crystal on tungsten filament results in producing high electron density in the beam which improves the resolution much better than conventional devices. Specifically, in a FESEM, a cold source is used, where an extremely thin and sharp tungsten needle with tip diameter 10 - 100 nm acts as a cathode in front of a primary and secondary anode. The voltage between anode and cathode can be varied from 1 kV to 30 kV. Since diameter of electron beam produced by FE source is much smaller than the standard microscope, the obtained image quality will be extremely good. This whole column is kept in high vacuum ($\approx 10^{-8}$ torr) to reduce the scattering process. The microscope used for our studies is supplied by Quanta 3D FEG which consists of FE electron source, which is heated as well as called Schottky source. Zirconium oxide coated tungsten filament is used to lower the work function of cathode material.

The electron beam is focused to sharp tiny spot by the electromagnetic lenses and apertures present in the column. This lens system consists of condenser lens, scan coils, objective lens, and stigmator coil. In condenser lens, the current determines the beam diameter. i.e., lower the current smaller the diameter, larger the current larger the beam. The scan coils deflect the electron beam. The objective lens focuses the electron beam on the object. And stigmator coils are used to correct irregularities in x and y deflection of the electron beam to obtain round shaped beam. If the beam is not circular but elliptical then image looks stretched and blurred. When the well-focused electron beam incident on the object, the secondary electrons are emitted from the object's surface at a particular velocity. This velocity is dictated by the levels and angles at the object's surface. The secondary electron signal generated by the beam-sample interaction is collected and used to create an image by scanning a cathode ray tube. Point-by-point measurements are used to create an image that depicts the varying efficiency with which a certain signal is generated and collected at various locations on the specimen's surface. The secondary electrons' characteristics influence where and how much the image is illuminated. Digital images can be formed from this contrast in real time, and this image can be used for further processing of the item. The back scattered electrons by atoms after incidence on the object are also used phase contrasting imaging. These back scattered electrons are originated in deeper region of sample which are having energies more than 50 eV with majority electrons are having 3/4th of incident beam energy. The numbers of back scattered electrons are greatly dependent on mean atomic numbers of the specimen at incident spot of beam which implies, as the atomic number increases, more the back scattered electrons will be originated. These electrons give depth information and atomic number contrast in the image. Hence, these images can provide information about elemental distribution in sample. When an inner shell electron is removed from a sample by an electron beam, a higher energy electron fills the shell and releases energy as a distinctive X-ray with characteristic energy. Energy Dispersive Spectroscopy (EDS) is used to determine the atomic composition and estimate the abundance of elements in the sample using these distinctive X-rays.

In this thesis, we have used Quanta 3D FEG (FEI, Netherlands) FESEM to obtain the images. Energy Dispersion Spectrometer (EDS) attached to FESEM, for elemental mapping. The system also consists of Cathodoluminescence (CL) and Focused Ion Beam (FIB) setups.

2.5 Atomic Force Microscopy

The atomic force microscopy was invented by Binning, Quate and Gerber in 1986. It is one of the earliest techniques capable of detecting distances in fractions of a nanometre. The AFM made it possible to see all kinds of surfaces with a high precision, even those that were insulating. AFM offers information on surface quality in terms of root-mean-square roughness, as well as morphology and average grain size. In the contact mode, the AFM principle is based on the detection of a short-range interaction between the sample and the probe, which is dependent on the distance between them. Typical tips used are silicon tips of pyramid shape with opening angles of 10^o-15^o near the apex and a maximum radius of 5 nm, resulting in pictures with lateral resolution of ≈5 nm. The tip of a cantilever is scanned across the sample's surface, which moves up and down along its topography. To construct an image, the displacement caused by the atomic forces of the features at various points on the surface can be measured[121]. The van der Waals force between the tip and the surface is measured by the AFM, which can be either the short-range repulsive force, in contact mode or the longer-range attractive force, in non-contact mode.

To characterize sample, AFM can be used in three different modes such as contact mode, tapping mode, and non-contact scanning mode. For a contact mode scan, the tip is in direct touch with the surface being scanned, and the resultant image is formed by a repulsion force. To capture an image while tapping, the tip briefly presses down on the surface of the sensor. During non-contact mode, the tip moves above the sample and the picture is formed by the forces between the tip and sample. The tip is scanned across a surface using feedback mechanisms that allow the piezoelectric scanners to maintain the tip at a constant force to get information about height or height above the sample surface for information regarding force. In this thesis, to characterize InGaN thin films, we used an AFM system supplied by Vecco, USA.

2.6 High Resolution X-ray diffraction

X-ray diffraction is a non-destructive technique. It is extensively used in solid state physics and material science research. X-rays with energy of several thousands of electron volts (~keV) have the wavelength in the order of few angstroms (Å) as same order as atomic spacing in crystals. This makes XRD, a powerful technique to investigate microscopic properties of solids such as structure of crystal, defects, chemical components, and stress[122–124].

X-ray diffraction patterns are produced when the X-rays diffracted from crystal lattice and the outcoming X-rays interfere constructively. It is only when X-rays meet the conditions of Bragg's Law that constructive interference occurs, which is mathematically stated as: $2d\ sin\theta = n\lambda$, where λ is the wavelength of the X-ray, 2θ is the angle between incident beam and diffracted beam (diffraction angle), d is the spacing of reflection planes and n is the order of reflection. Bragg's Law enables us to determine the crystal structure in detail. The Miller indices (hkl) of the family of planes determine the interplanar distance, d. For cubic crystal with lattice parameter a, the distance d is given by, $d = \frac{a}{\sqrt{(h^2+k^2+l^2)}}$ and for hexagonal crystal such as wurtzite GaN, it is given by, $d = \frac{1}{\sqrt{\left[\frac{4}{3}\frac{(h^2+hk+k^2)}{a^2}+\frac{l^2}{c^2}\right]}}$

2.6.1 HRXRD Setup

Figure 2.8a shows the schematic representation set up of the HRXRD diffractometer. The incident CuK_α X-ray beam (wavelength, λ= 1.540595 (2) Å) is generated by an X-ray tube with a copper cathode and a four-bounce Ge (220) monochromator in the diffractometer. Figure 2.8b shows the angle, ω formed by the incident X-ray beam and the crystal's surface. The crystal to be studied is held in place by a sample holder called as Euler cradle which can then be rotated around the Euler angles ω, φ and χ as represented in the Figure 2.8b. The angle φ

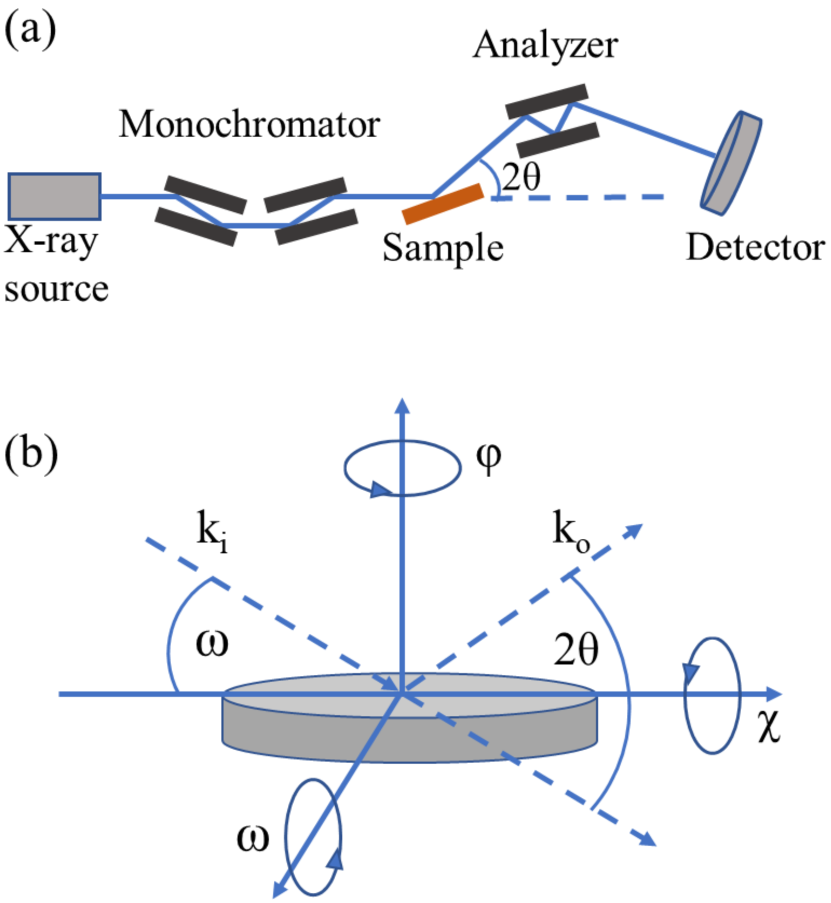

Figure 2.8 (a) Schematic representation of HRHRD setup (b) the geometry of goniometer with Euler angles of rotations

measures the azimuthal rotation around the surface, ranging from 0 – 360°, normal to the mounted sample. The angle χ represents the angle between surface of the sample and the plane of interest, which varies from 0-90°. The scattered beam from the sample can be detected by an X-ray detector at angle 2θ made with incident beam. Suppose the incident and diffracted beam vectors k_i and k_o make suitable angles with respect to the crystal then the scattering vector ($S = k_i - k_0$) will end at a reciprocal lattice point and therefore the scattering vector (S) can thus be varied by altering ω and the position of the detector as shown in the Figure 2.8b, and the entire crystal can be investigated.

2.6.2 HRXRD Scan types

In HRXRD, the different kinds of scans are possible which provide more information about the samples, and are as follows:

Detector scan: Align 2θ position of detector to observe the X-ray beam that falls directly from source or diffracted from crystal planes.

Z scan: After setting a sample to proper X and Y positions, suitable value of Z (height) can be obtained from bisecting X-ray beam by sample.

Rocking curve or ω scan: The sample will be rotated about ω axis while detector is kept in fixed position. The rocking curve is a representation of the scattered X-ray intensity as a function of ω. The crystallite size and tilt in relation to one another impact the width of the symmetric rocking curve. The asymmetric rocking curve in a mosaic crystal broadens due to the twisting of the crystallites. Because of this, the FWHM of the rocking curve is frequently used as a measure of the tilt and twist of crystallites in an epitaxial film. In general, the smaller the FWHM, the more aligned the individual crystallites are and the greater the crystals' sizes become.

2θ-ω scan: The sample (or X-ray source) is rotated by ω and the detector is rotated by 2θ with an angle ratio of 1:2. This scan can be used to determine if the crystal has other crystallographic phases.

ω-2θ scan: It is 2θ-ω scan with ω in the x-axis, which is same as the typical scan type for reflectivity and high-resolution work. Reciprocal space map is widely used to map a two-dimensional region of the reciprocal space by combining a ω-2θ scan and a ω scan. The a and c lattice constants of the epitaxial layer of interest can be determined using a reciprocal space map of an asymmetrical reflex.

2θ scan: The detector is moved while the sample and source remain still. This scan is most commonly used to align the epitaxial film under investigation.

φ scan: The sample is rotated around the φ axis which is usually in the plane of the sample. The in-plane epitaxial relationship between the substrate and the overgrown film can be established by doing a 360^o φ-scan for the substrate and the thin film on top.

χ scan: The sample is rotated around the axis (plane of the sample rotated with respect to the incoming beam), this scan is also commonly utilised to pre-align the epitaxial film under investigation.

2.6.3 Diffraction Geometry for 2θ-ω scan

Symmetric: Planes parallel to the sample surface are studied in this geometry. The incoming and outgoing beams' ω and 2θ with respect to the sample surface are both changed at the same time, where $\omega = \theta$.

Asymmetric: An asymmetric 2θ-ω scan can be performed for the planes having tilt (τ) with respect to the sample surface. As in the case of a symmetric scan, the detector is placed at an angle of 2θ with respect to the incoming beam. The incoming beam, however, makes an angle of ω with respect to the sample surface. Since $\omega = \theta \pm \tau$, grazing incidence (-) or grazing exit (+) 2θ-ω scans can be collected in this asymmetric geometry.

Skew-symmetric: An alternative way of getting the asymmetric scan is in the skew-symmetric geometry, where the sample is tilted over a fixed angle around the χ-axis instead of the ω-axis. The rest of the procedure to acquire the 2θ-ω scan in skew-symmetric geometry is same as symmetric scan.

In this thesis HRXRD is mainly used to extract the following information:

i. The crystalline nature of the film and its epitaxial relation with the substrate
ii. Indium concentration of samples by using c-parameters of the sample

2.7 Raman Spectroscopy

Raman spectroscopy is the study of matter by the inelastic scattering of monochromatic light (Ex. Laser), where scattered light is used to measure the vibrational modes of sample. It is named after a physicist C. V. Raman, for which he was awarded Nobel prize in 1930. When the laser light interacts with molecular vibrations, phonons, or other excitations in the system, resulting in the energy of the laser photons being shifted up or down. The shift in energy gives information about the vibrational modes in the system. A Raman spectrum consists of a series of peaks displaced to lower and higher frequencies from the incident light. The peaks which are at lower frequency are known as the Stokes lines and those at higher frequency are known as anti-stokes lines, which are usually weaker than the stokes line. The appearance of lines in the Raman spectrum is governed by selection rules, and the gross selection rule is that to be Raman active a molecule must have anisotropic polarizability, i.e., polarizability of the molecule should change as it vibrates. A nonlinear polyatomic molecule containing N atoms has 3N-6 modes of vibration, called as normal modes, each mode is associated with symmetry and a specific fundamental vibrational frequency which provides chemical and structural information of samples.

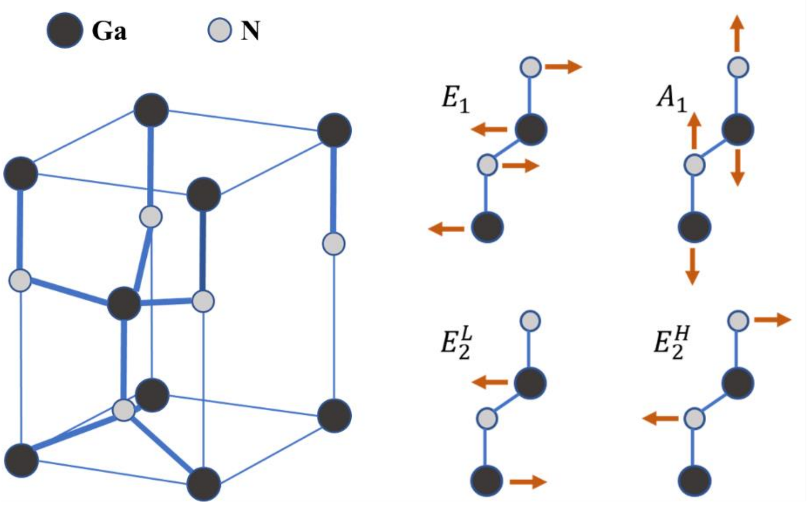

Figure 2.9 Wurtzite crystal structure of GaN and its Raman active modes

In III-nitride semiconductors, the vibrational states are sensitive to crystalline quality, alloy composition, stress, electron concentration etc. and the group theory calculations predict a total of 8 normal modes at gamma point (zone centre): $2A_1+2E_1+2B_1+2E_2$ for the hexagonal wurtzite structure. Among these modes A_1, E_1 and E_2 modes are Raman active. Figure 2.9 shows the crystal structure of GaN and its Raman vibrational modes. To observe different Raman modes different geometries are essential. For instance, to observe A_1 (LO) and E_2 modes the geometry should be $z(x,x)\bar{z}$ and to observe E1 (TO) and E1 (LO) modes requires $x(y,z)y$ geometry. The geometry notations are understood in following illustration. In $\alpha(\beta,\gamma)\delta$ geometry, the incident light α with polarization direction β and direction of scattered light δ with polarization direction γ.

The E_2 mode has high Raman scattering cross section and it is used to determine crystalline quality. Its width determines the quality of crystal, implies, narrower the width of peak better is the crystal quality. Also, biaxial strain in c-plane of wurtzite GaN is commonly probed by observing shift in E_2^H mode frequency (for GaN, 568 cm^{-1}), as it is sensitive to biaxial strain in the c-plane and has strong signal in spectrum[125,126].

2.8 Ultraviolet-Visible-Near Infrared Absorption Spectroscopy

The bandgap of grown III nitride films in this study is measured by using ultraviolet-visible-near infrared (UV-Vis-NIR) spectroscopy technique[127]. In this technique, the incident light is split into two rays of equal intensity by using beam splitter. Both the rays fall on two identical detectors while the sample is inserted in the path of on of the two rays. The ratio of the two intensities recorded by the detectors is plotted against energy (E) of incident light. Intensity of light passing through sample with thickness d is given by

$$I_t(E) = I_o \exp\left(-\alpha(E)d\right)$$

where I_o is intensity of incident beam and α is the absorption coefficient of a sample and it is given by

$$\alpha(E) = C\,(E - E_g)^n$$

where E_g is the bandgap of the material, C is the constant and n values denote the nature of transition; for example, for direct transition n=1/2 and for indirect transition n=2. A Tauc plot[128] pioneered by J Tauc and he proved that momentum is not conserved even in direct optical transition[129]. This plot consists of the energy E of incident light in x axis and $(\alpha h\upsilon)^n$ in y axis. By extrapolating the linear region in the plot to the energy axis at $(\alpha h\upsilon)^n = 0$, results in obtaining the energy of optical bandgap of material. In this work, we carried out absorption measurements at room temperature using Perkin Elmer Lambda 900 UV-VIS-NIR spectrometer with Xenon lamp source.

2.9 Photoluminescence and Cathodoluminescence spectroscopy

Photoluminescent spectroscopy is a nondestructive, noncontact method of investigating the electronic structure, defect levels and impurities of semiconductor materials via light emission[130,131]. When a suitable laser or filtered light (for example, a Xenon lamp) with a photon energy higher than the bandgap of the semiconductor is incident onto a sample, it is absorbed and photo excitation occurs, causing the electrons to jump to a higher electronic state, from which it then releases energy (in the form of photons), allowing it to relax and return to a lower energy level (recombination). The emission of light, or luminescence through this process is called as photoluminescence (PL). Some of the observed recombination pathways are shown in Figure 2.10.

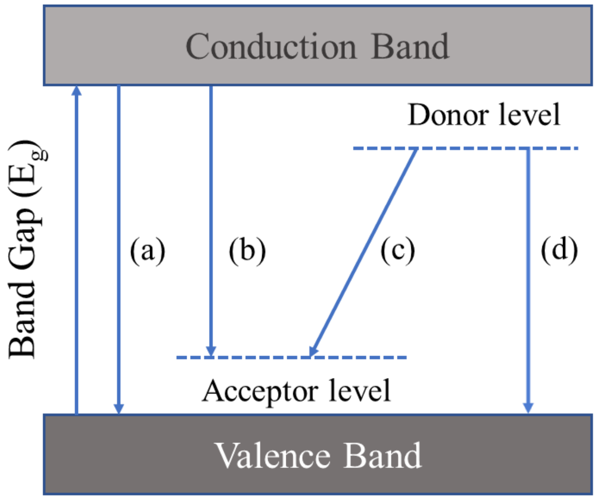

Figure 2.10 Examples of radiative recombination transitions in semiconductors: a) band to band transition, (b) free electron to acceptor level transition, (c) donor acceptor pair recombination, and (d) donor bound electron and free hole recombination.

In cathodoluminescence (CL), unlike photoluminescence energetic electrons are used as excitation source[132]. Commonly, CL set up is attached to SEM system. An electron probe is very flexible due to ease of scanning, focusing and the large depth of field. When compared to photons, the interaction volume inside the material for electrons is bigger and which has advantage in varying the electron beam energy to change the penetration depth.

In this thesis, we have used customized Edinburgh instrument for photoluminescence. He-Cd 325 nm laser has been used as excitation source whereas, a Gatan MonoCL4 detector attached to Quanta 3D FEG (FEI, Netherlands) FESEM system is used to carry out CL measurements.

2.10 X-ray Photoelectron Spectroscopy

X-ray photoelectron spectroscopy (XPS) is widely used technique to analyse the surface, which provides valuable quantitative and chemical state information from sample's surface[133–135]. This technique also referred as Electron Spectroscopy for Chemical Analyses (ESCA). XPS spectra of a sample are acquired by irradiating the surface with mono energetic Al/Mg-K_α X-ray beam, which have energy of 1253.3/1486.6 eV, while simultaneously measuring the emitted electrons' kinetic energy from top of surface (1-10 nm) and analysed by an electron energy analyser. The photoemitted electrons are collected by using concentric hemispherical analyser as shown in the Figure 2.11a. The XPS spectrum is recorded by counting the number of electrons that are ejected over a range of electron kinetic energies. Peaks show up in the spectrum when atoms emit electrons with a specific characteristic energy. The energies and intensities of the photoelectron peaks allow for the identification, chemical state, and quantification of all the surface elements. Depth profile also carried out along with XPS with the help of ion sputtering.

2.10.1 Photoemission Process

X-ray photoelectron spectroscopy (XPS) is a surface sensitive quantitative spectroscopic technique based on photoelectric effect. When a high-energy photon interacts with matter, an electron is ejected from an atomic orbital or a band and reaches the vacuum level, triggering photoemission from a solid sample and the schematic is given in Figure 2.11a. The excitation energy must be large enough to overcome the sample's work function. The initial state of photoelectron can be either a core level state or valence band. The kinetic energy (K.E.) of the photoelectron is expressed as

$$K.E. = h\upsilon - B.E. - \varphi$$

Where, $h\upsilon$ is the energy of incident photon, $B.E.$ is the binding energy of electron and φ is the work function of the material, which is the difference between the Fermi level and the Vacuum level (Figure 2.11b). If we know $h\upsilon$ and φ then K.E. is measured and from which we can obtain the B.E. of characteristic core levels in the sample. A sample's chemical composition is conveyed by the core levels of each element, as each element has a unique set of core levels. It is also possible that adsorbates may alter the B.E. shift due to the type of bonding, oxidation state, or other chemical environment prior to the photoemission event.

2.10.2 Analytical Information acquired from XPS

Many analytical information can be obtained by XPS measurements and are as follows[136,137].

Survey Scan: Energy peaks in the survey scan identify the elemental composition of the topmost layer of the analysed surface. In this scan all, except Hydrogen and Helium, are detected.

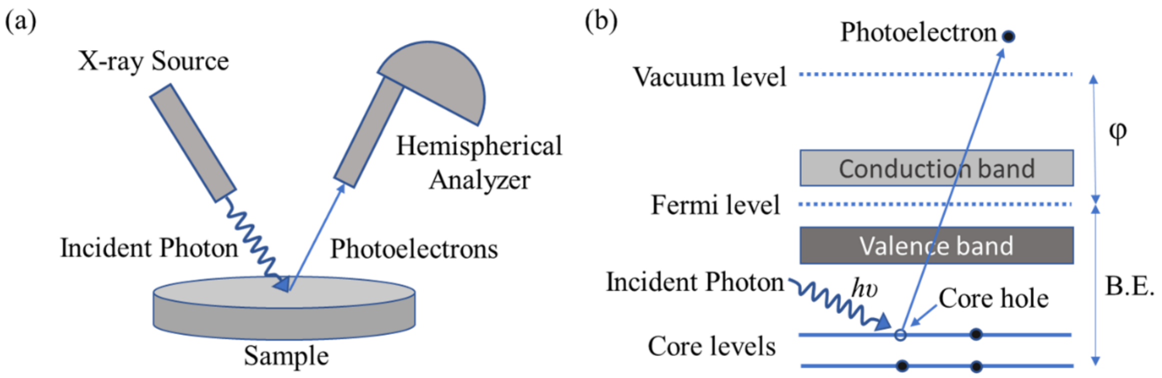

Figure 2.11 schematic diagram of (a) XPS (b) the photoemission process

High Resolution Core Level Scan: The chemical state of each element assessed through binding energies of core electron. By fitting the peaks of spectra, the binding energies can be determined, precisely. The shifts observed in the spectrum are attributed to atom's oxidation state, chemical bond, or crystal structure.

Valence Band Scan: Position of valence band maxima (VBM) of the sample can be determined by this scan and it is usually carried out in the lower binding energy region, 0-30 eV. Electronic structural information in metal, semiconductor and insulators and the nature of doping in semiconductors (p-type or n-type) can be obtained by VBM scan.

Quantification: The concentrations of elements are calculated by integrating the area under the characteristic peak in survey scan or core level scan for each element. The elemental concentration values determined by sensitivity factors applied to the peak. The atomic fraction of any constituent in a sample is given by

$$X_a = \frac{I_a/S_a}{\sum I_i/S_i} \times 100\%$$

Where, I_a is the area/intensity of the peak of element A, S_a is the atomic sensitivity factor for the element A and the summation represents over all the constituent elements of the surface.

Depth profile: With the help of ion sputtering the material can be removed from the sample surface to measure the elemental composition as a function of depth into the sample.

Elemental Mapping: A relative concentration of elements is determined as a function of lateral position on surface of sample.

In this thesis, we have used Omicron XPS system to identify, quantify different constituent elements and to determine chemical state of the elements. The Fityk an open-source software is used to fit the peaks by considering physical aspects like position and FWHM.

2.11 Resistivity and Hall Effect Measurement

Electrical measurements have been carried out in this work using Versa Lab Physical Property Measurement System (PPMS) by Quantum Design, to determine the carrier concentration, mobility, and resistivity of the samples.

2.11.1 Resistivity

To determine the resistivity of a sample, we have used four-probe method[138] which provides more accurate value compared to a two-probe method. Four ohmic contacts lying in the same line, are deposited with equal spacing (s) between two contacts. The current is passed through two outer probes and measures the voltage through inner probes as shown in the Figure 2.12a. Resistivity calculation of sample depends on the dimension like bulk or thin film. In case of thin films, the thickness (t) of sample is very small compared to that of bulk (s).

For a bulk sample the resistivity is given by

$$\rho = 2\pi s \,\frac{V}{I}$$

In case thin films, the sheet resistance or surface resistance is a common electric property used and measure in ohms per square ($\Omega/\square$). It is calculated by

$$R_s = \frac{\pi}{\ln{(2)}}\frac{V}{I} = 4.532\frac{V}{I}$$

Which is again related to resistivity as $\rho = R_s t$. Most of the samples used in this work of ≤ 1μm thus the formula is valid for our samples.

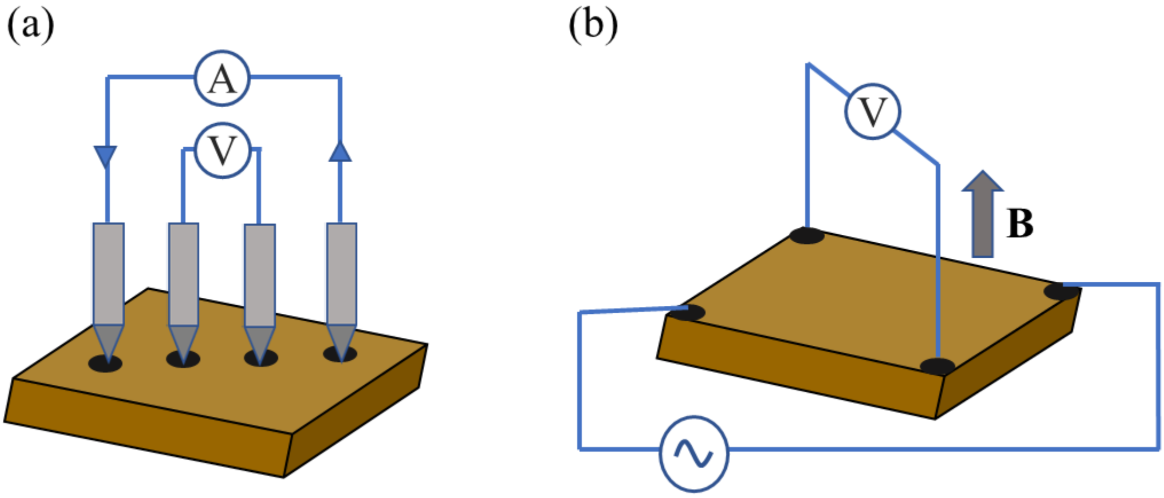

Figure 2.12 Schematic diagram showing (a) four-probe method resistivity measurement (b) Hall measurement

2.11.2 Hall Effect Measurement

Hall effect describes what happens to current flowing through a conducting material (metal, semiconductor) if it is exposed to a magnetic field B[139]. This phenomenon was discovered by Edwin Hall in 1879 and it is also considered as an extension of Lorentz force, which is the force exerted on a charged particle moving through magnetic field. Figure 2.12b shows the van de Pauw geometry[140] of Hall measurement. If a current I_x passes through a conducting material along a positive x direction, under the applied magnetic field in z direction then a voltage difference V_H appears along y direction, and it is called Hall voltage, and is given by

$$V_H = \frac{I_x B_z}{nqt} = R_H \times \frac{I_x B_z}{t}$$

where, q is charge of charge carrier, n is charge carrier density and t is thickness of the sample. The term, $R_H = 1/nq$ is called Hall coefficient and is negative if the electrons are majority charge carriers and positive if holes are majority charge carriers. By knowing Hall voltage, magnetic field strength, current and thickness of the sample, we can calculate Hall coefficient and from which we can calculate carrier concentration by using relations, $n = -1/qR_H$ for carrier concentration of electrons and $p = 1/qR_H$ for holes. Hall mobility can be calculated by knowing carrier concentration n and the conductivity σ, and it is given by $\sigma = nq\mu_H$.

2.12 PEC Measurement setup:

A typical three electrode configuration photoelectrochemical (PEC) cell consists of a working electrode (WE), a counter electrode (CE) and a reference electrode (RE). Figure 2.13 shows a schematic of three electrode configuration PEC cell. The basic PEC test setup consists of a light source, optical filters (ex. AM 1.5 G), shutter or chopper (optional), a photoelectrochemical cell, and an electrical measurement instrument. Many types of light bulbs are available, but xenon and tungsten bulbs are most commonly used due to their broad energy range. PEC cell should be made of transparent material to illuminate light (In case of UV irradiation, quartz windows must be used). The distance between all the electrodes should be less to avoid effect of electrolyte resistance.

The choice of the counter electrode based on type of working electrode. For n-type semiconductors as WE, H^+ is reduced to H_2 by means of hydrogen evolution reaction at CE. In this instance, platinum (Pt) foils or mesh with large surface area make good CEs. For p-type WE, water is oxidized into H^+ and O_2 by means of oxygen evolution reaction at CE. In this instance oxide materials like RuO_2, are much suitable as CE, which can reduce overpotentials compared to noble metals. REs are required to measure the potential of WE on a well-defined electrochemical scale, versus normal hydrogen electrode (NHE). Many REs are available but silver- silver chloride in saturated KCl (Ag/AgCl, with $E^{o}_{Ag/AgCl}$=+0.197 V vs. NHE at 25 ^{o}C) and saturated calomel electrode (SCE, with E^{o}_{SCE}=+0.241 V vs. NHE at 25 ^{o}C) electrodes are typically used[141].

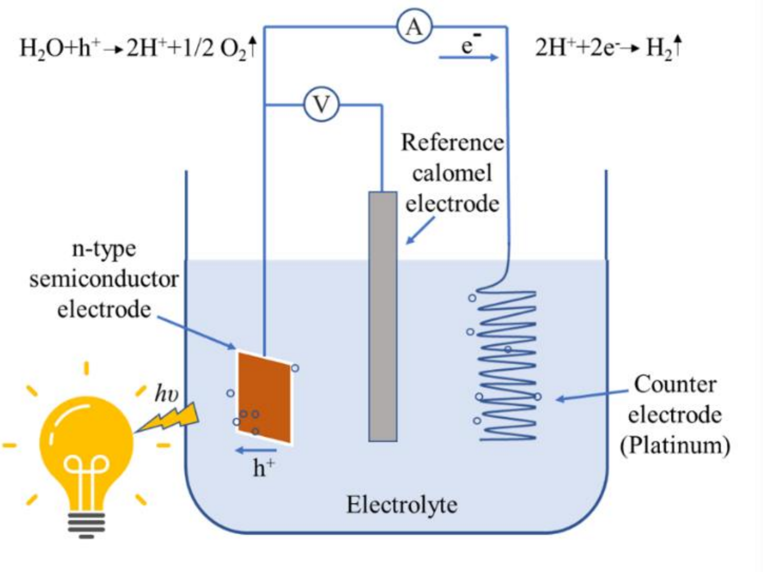

Figure 2.13 Schematic representation of photoelectrochemical cell setup

The working principle of PEC measurement is, for n-type semiconductors (WE, photoanode), the light will incident on the surface of the semiconductor, and it produces electron-hole pairs, the electrons move towards CE (Pt) where reduction of H^+ takes place and the hole will move towards the surface of WE and oxidize water.

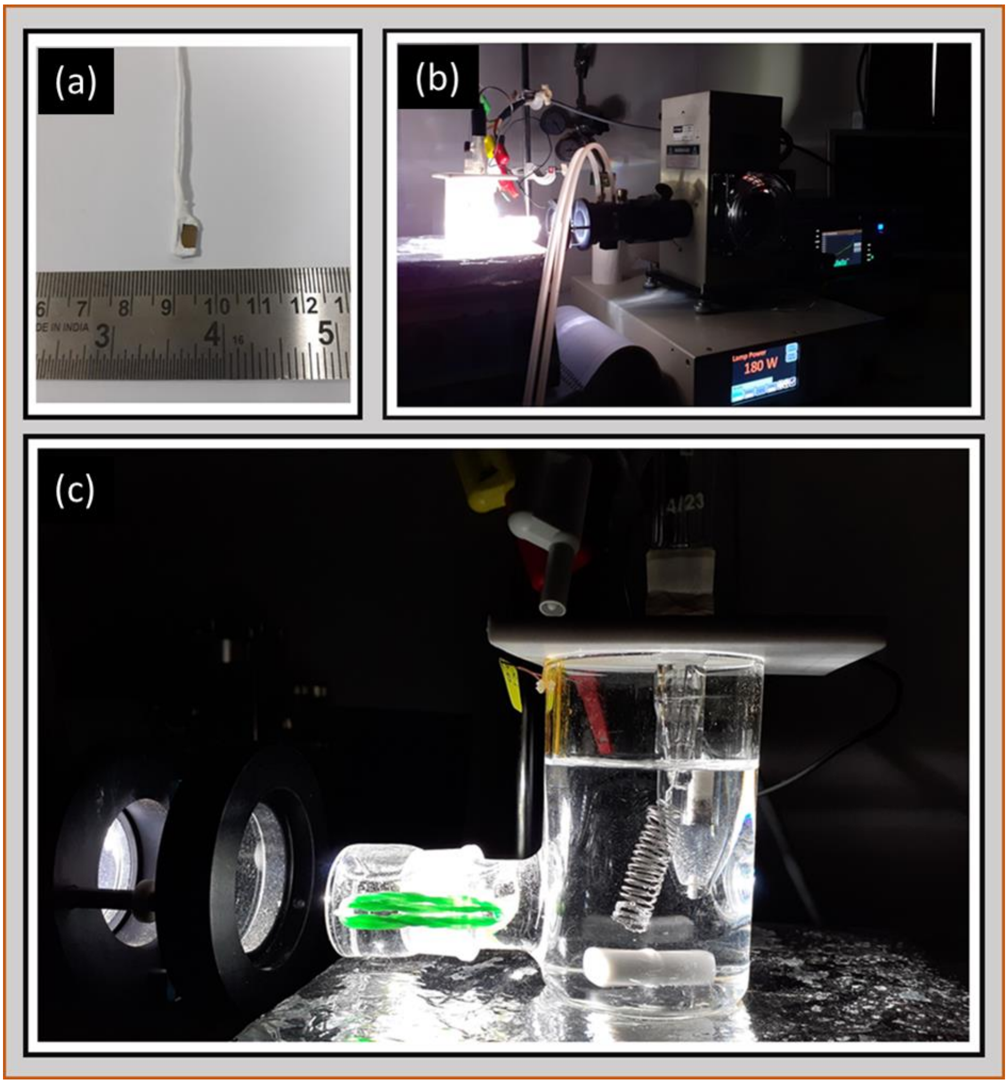

Figure 2.14 Photograph of (a) photoelectrode device (b) PEC measurement setup used in this study and (c)an event of hydrogen bubble generation in PEC cell.

In this thesis, we have used MBE grown III-nitride samples as WEs, by giving ohmic contact [ex. Ti (20 nm)/Al (100 nm) on GaN] and covered it with insulating epoxy and later with Teflon as shown in Figure 2.14a. Saturated calomel electrodes as RE and platinum as CE. We have used different electrolytes such as Na_2SO_4, HCl and NaOH of 1M. Figure 2.14b shows the experimental setup used in these studies, which consists of a xenon lamp supplied by Newport, PEC cell with three electrodes and Keithley source meter to measure the photocurrent (between WE and CE). An event of observed hydrogen bubble generation during the experiment is shown in the Figure 2.14c. during the experiment the electrolyte is stirred with magnetic stirrer to avoid the accumulation of bubbles on the surface which reduce the electrochemically active surface area.

Chapter 3
Heterostructure photoelectrodes for efficient charge carrier separation

This chapter discusses about the separation of photogenerated charge carriers by forming heterostructures of GaN and InGaN thin films with TiO_2. Also, the morphologies, structural and optical properties of the grown films

3.1 GaN/TiO_2 heterostructure photoelectrodes[*]

3.1.1 Introduction

The production of hydrogen via solar water splitting in a photoelectrochemical cell (PEC) is seen as a possible efficient and simple remedy for the imminent energy crisis. GaN is a promising electrode material that is extensively explored for water splitting applications not only because of its wide direct band gap and chemical stability but also because of its tunable band gap by alloying with Indium[142–145]. However, being a homogeneous direct band gap semiconductor, its recombination probability of the photoexcited electrons and holes is high, thus reducing the charge separation efficiency. Several strategies are reported in the literature to improve light absorption and charge separation efficiencies, and one among them is increasing the surface area by growing nanostructures. Another approach to improve efficiency is the fabrication of type II semiconductor heterostructures[146–148]. Type II heterostructures whose interfacial band-structure electrostatically changes, will facilitate the enhancement of water splitting efficiency by extending the light absorption range and the charge separation process. The key characteristic requirement of a semiconductor heterostructure, to be used as a photoelectrode for water splitting, is the built-in electric field at the space charge region (SCR) which helps in the transfer and separation of the photogenerated electrons and holes.

---

[*] **Kubakaddi, Shivaram B.**, et al. "Nanostructured p-TiO2/n-GaN heterostructure as a potential photoelectrode for efficient charge separation." Nanotechnology 29.50 (2018): 50LT02. ©IOP Publishing. Reproduced with permission. All rights are reserved.

In this section, a semiconductor heterostructure, GaN/TiO_2 is discussed as a promising photoelectrode material and we compared the structural, morphological, optical, and photoelectrochemical properties of GaN epilayer/TiO_2 (TGE) and GaN NWN/TiO_2 (TGN) structures.

3.1.2 Experimental Details

GaN NWN is grown on the c-sapphire substrate by using plasma-assisted molecular beam epitaxy. The Gallium Knudsen cell during the growth is held at 1030 ^oC and an RF nitrogen plasma generator with a forward power of 375 W is used as the active nitrogen source. The N_2 flow rate during growth is kept at 4.5 sccm. The substrate temperature is held constant at 630 ^oC during the entire growth and the approximate thickness of GaN NWN is 1µ. TiO_2 thin films are conformally coated on the MBE grown GaN NWN, by ALD (Beneq, TFS-200) to form the heterostructure. High purity chemical precursors $TiCl_4$ and double distilled water are employed as Ti and O sources respectively. Ultrapure N_2 gas, used as process and carrier gas, is allowed into the reactor at a flow rate of 600 sccm. The pulse and purge times of $TiCl_4$ and double distilled water are 200 ms and 2 s, respectively. The reactor temperature is maintained at 300 ^oC and the deposition is carried out for 2000 cycles, to obtain 100 nm thick TiO_2.

3.1.3 Results and discussion

The Deposited samples are characterized with different techniques and results are discussed here.

3.1.3.1 FESEM Morphology and RHEED pattern

The top view FESEM image of MBE grown GaN thin film is as shown in the Figure 3.1a. and can be seen that the morphology has high surface to volume ratio. Figure 3.1b shows the RHEED pattern of the same sample after the deposition while the sample is still in the growth chamber. The dotted pattern indicates that film three-dimensional growth of GaN.

The properties of a semiconductor device depend on the morphology of the grown thin films. Figure 3.2 a & b show the FESEM images at the lateral interface region of the

TGE and TGN heterostructures, showing both the GaN and TiO_2 in the masked and unmasked regions. In TGE, the GaN epilayer showed a smooth surface morphology whereas, in TGN, GaN grown by MBE showed the uniformly distributed interconnected

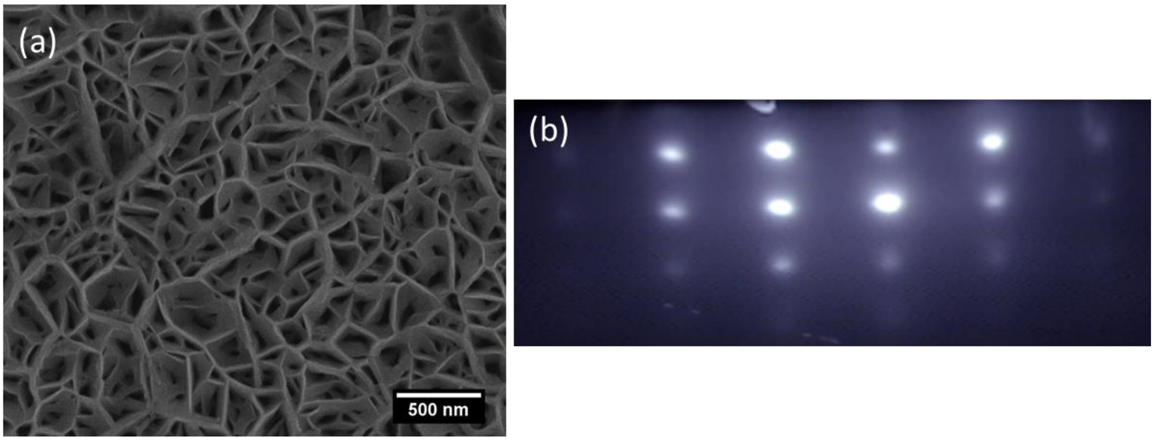

Figure 3.1(a) Top view FESEM image of GaN nanowall network (b) in-situ RHEED pattern of GaN

GaN NWN structure. The NWN structures possess certain advantages over a flat layer, like higher surface to volume ratio, high electron mobility and lower defect density. The ALD grown TiO_2 showed conformal coating with the same morphology as that of the underlying layer. Because of the higher surface to volume ratio, light absorption will be more in the case of TGN compared to the smooth surface morphology of the TGE structure. Our previous studies of the bare NWN [149] have shown that light trapping in the cavities between the nanowalls enhances both absorption and emission of light. Also, in the GaN/TiO_2 heterostructure, the band bending promotes charge separation. This system increases charge-carrier lifetimes that can positively influence photocatalytic activity.

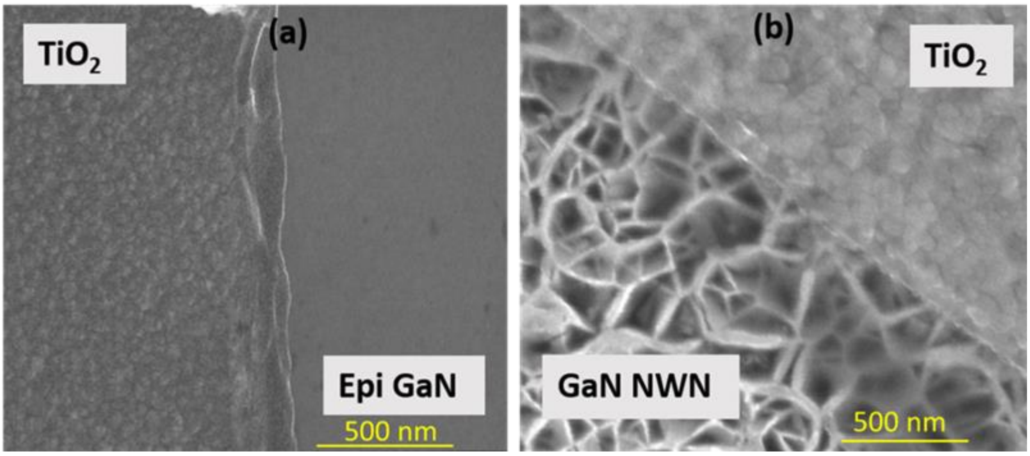

Figure 3.2 Top view of (a) TiO_2/GaN epilayer and (b) TiO_2/GaN NWN heterostructures.

3.1.3.2 Structural Properties

Anatase TiO_2 is the appropriate phase for most efficient water splitting as compared to the rutile and brookite phases[150]. X-ray diffraction recorded using a Panalytical X-ray diffractometer, revealed the crystalline quality and phase formation of the grown TiO_2 thin films. The XRD pattern of the heterostructures TGE and TGN are shown in Figure 3.3a. The high intensity (002) peak (around 34.5^o) of GaN and (004) peak (around 37.8^o) of TiO_2 indicate that the growth of GaN and TiO_2 is along the c-direction. All the peaks are indexed to either the hexagonal wurtzite phase of GaN (ICSD file No. 894921) or the tetragonal anatase phase of TiO_2 (ICSD file No. 882361) and did not show the presence of any rutile or brookite phases of TiO_2. To further confirm the crystallinity and phase formation of the grown TiO_2 and GaN, Raman spectra were recorded using 532nm Nd:YAG laser using Jobin Yvon LabRam HR spectrometer and the results are illustrated in Figure 3.3b. The Raman modes at 142 cm^{-1}, 196 cm^{-1}, 639 cm^{-1} correspond to the three E_g modes, and the 396 cm^{-1} is the B_{1g} and 516 cm^{-1} corresponds to A_{1g}/B_{1g} the modes of anatase TiO_2 [151]. The peak around 569 cm^{-1} corresponds to the characteristic mode of bulk GaN (E_2^{High}) and is observed in both TGE and TGN heterostructures. The lesser intensity in Raman peak in the case of TGN is due to the mosaic and porous structure of NWN. Because of the porous NWN structure, the number of atoms excited by the laser will be less compared to the planar structure._The vibrational mode around 734 cm^{-1} is assigned to the A_1(LO) mode of GaN[152]. The Raman spectra of TGN show the absence of A_1(LO) mode, which may be due to the high carrier concentration[153] (~10^{19} cm^{-3}) as compared to the epi GaN (10^{16} cm^{-3}) as observed by Hall measurements. The observed characteristic modes of TiO_2 confirm that

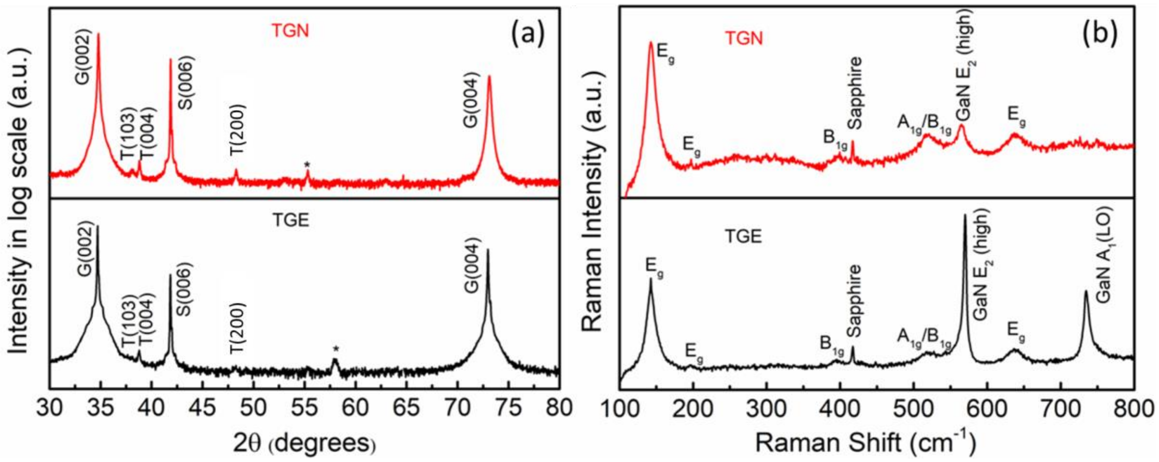

Figure 3.3 (a) XRD patterns and (b) Raman spectra of TGN and TGE heterostructures

the growth of TiO_2 thin film is in the anatase phase in both the structures. Hence, Raman spectra together with the XRD pattern confirm the anatase phase of TiO_2 in both the structures.

3.1.3.3 Optical Properties

To study the optical absorption and emission properties of the samples, we carried out UV-Visible spectroscopy and Cathodoluminescence measurements. Figure 3.4a shows the absorbance spectra of TGE and TGN heterostructures. TGN showed better absorbance than TGE and is due to the nanowall network morphology, where incident light can undergo multiple scattering inside the pores and will enhance light absorption. Thus, the morphology of the NWN structures contributes towards enhancing light absorption. The energy band gaps extracted from the absorbance spectra of TGN and TGE from the Tauc plot (shown in the inset of Figure 3.4a) are found to be 3.56 eV and 3.39 eV, respectively. The exponential tail observed near the band edge in the case of TGN indicates the presence of the extended localized defect states near the edge of conduction and valence bands within the energy band gap. The CL spectra for TGE and TGN structures acquired at an accelerating voltage of 3 kV are shown in Figure 3.4b. Both the structures showed a weak band-to-band emission around 3.4 eV and a strong and broad defect-related emission centering around 2.4 eV. The lower intensity in the band-to-band emission implies that the fabrication of heterostructure reduces the charge recombination and enhances charge

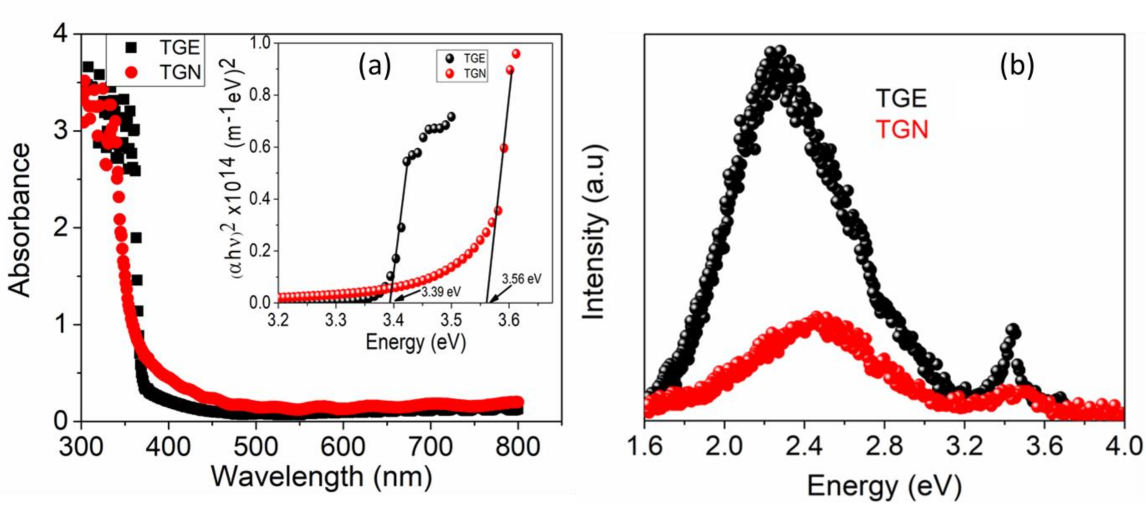

Figure 3.4 (a) Absorption spectra and Tauc's plot in the inset, (b) Cathodoluminescence spectra for TGE and TGN

carrier separation. As compared to the TGE, TGN heterostructures showed lower CL intensity, which can either be attributed to the reduced electron-hole recombination or due to higher charge separation induced by higher band bending at the interface.

3.1.3.4 XPS Studies

To unveil the effect of band-bending, XPS studies are undertaken. Figure 3.5 shows the valence band (VB) spectra obtained by XPS, of GaN epilayer and GaN NWN structure and the inset shows that of the TiO_2 layer. The valence band maximum (VBM) position was obtained by extrapolating a linear fit of the edge of the valence band photoemission to the baseline. The difference between Fermi level and the VBM for the epilayer is 2.7 eV and that for NWN is 3.2 eV, both showing n-type character. It is evident from the figure that the VBM of GaN NWN shifts to higher binding energy than in GaN epilayer due to the high charge carrier concentration. Similarly, the difference between Fermi level and VBM for TiO_2 is 1.2 eV, thus closer to VB, due to the p-type TiO_2, which has also been confirmed by room temperature Hall measurements. The p-type conductivity of as-grown TiO_2 thin films by ALD has been reported earlier [154].

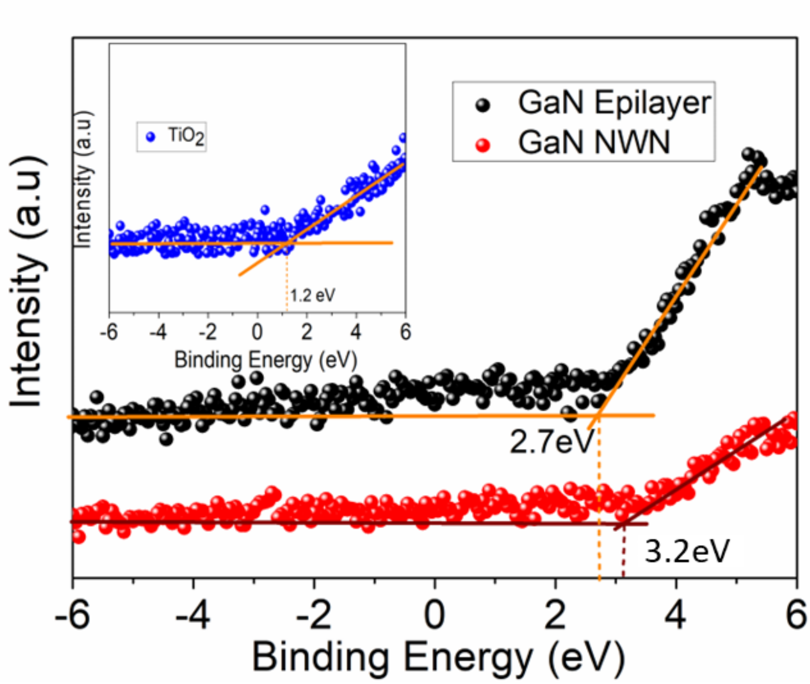

Figure 3.5 Valence band spectra for GaN NWN, GaN Epilayer and TiO_2

3.1.3.5 Photoelectrochemical Studies

To evaluate the charge separation and the feasibility of the heterostructure electrodes for water splitting applications, we have studied the photoelectrochemical properties. Figure 3.6a shows the linear sweep voltammogram (LSV) for TGE and TGN heterostructures under dark and illumination conditions. In both cases we observed a significant difference in photo current density as compared to dark current density. The photocurrent observed for TGE is 0.24 mA/cm^2 and that for TGN is 0.65 mA/cm^2 at 1.24 V and at an incident power of only 13 mW/cm^2 as compared to the 100 mW/cm^2 which is normally used in similar studies. The photo current densities observed for these structures are comparable to those reported earlier for GaN nanostructures or TiO_2 structures. For example, GaN with nanowire [143] and nanopore [155] structures showing photocurrent densities of 0.09 mA/cm^2 at 0 V and 0.32 mA/cm^2 at 10 V, respectively at a power of 100 mW/cm^2 and nanopyramid [156] with photocurrent density of 1 mA/cm^2 at 200 mW/cm^2 are reported. Similarly, TiO_2 with nanorod, nanowire and branched structures [157–159] with photocurrent densities of 0.018 mA/cm^2 at 1 V, 2.6 mA/cm^2 at 0.22 V and 0.85 mA/cm^2 at 0.65 V respectively, are also reported (The incident power in all these cases is 100 mW/cm^2).

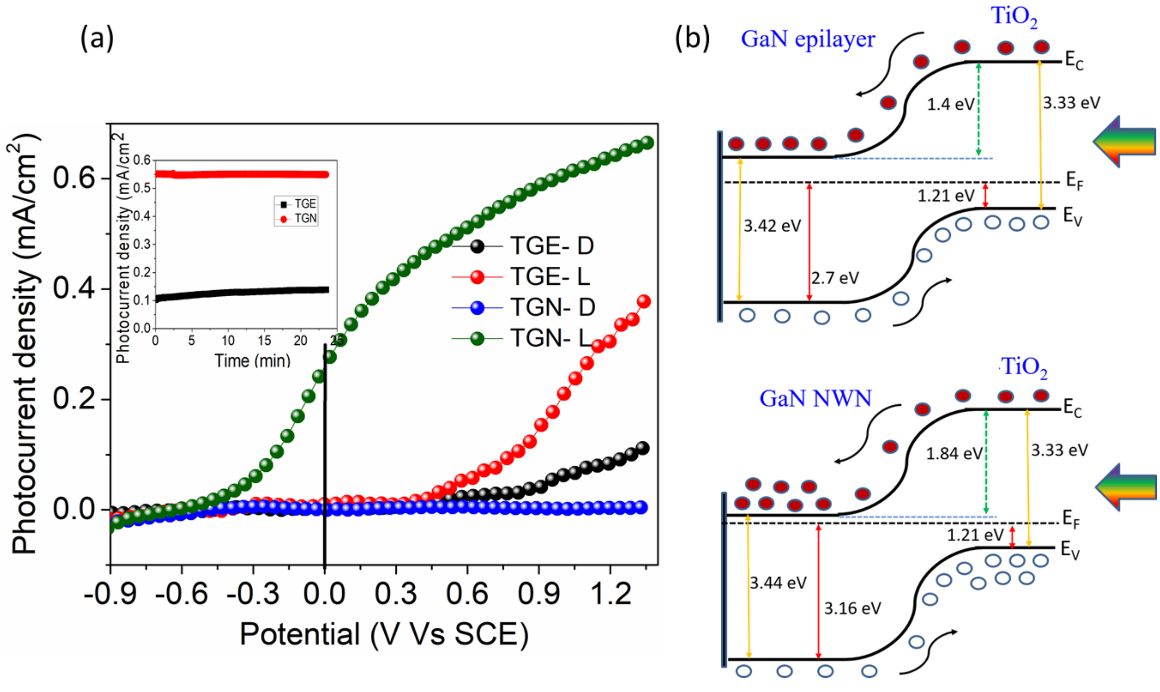

Figure 3.6 (a) Shows current density as a function of applied potential and inset shows chronoamperometric analysis at an applied bias of 0.8 V for 25 minutes (stability), (b) Schematic band diagram for TGE and TGN heterostructures.

The photocurrent onset potential (the voltage where J>0) (V_{onset}) for TGE is -0.43V and that for TGN is -0.56V. The shift in the cathodic onset potential of TGN towards more negative indicates enhanced charge separation. Also, the observed trend of the plot (Figure 3.6a) shows that the voltage required to attain the plateau photocurrent in the case of TGN is lower than that required for TGE. That means a lower electric field is enough to separate the electrons and holes in TGN, indicating the superiority of TGN to TGE. The photoelectrochemical stability of the photoelectrodes are tested by chronoamperometric analysis (see the inset of Figure 3.6a), by recording the photocurrent density over a time period of about 25 minutes at an applied bias of 0.8V. We did not observe any degradation in photocurrent density and the results show the stability of the photoelectrodes. Our results show a comparatively higher photocurrent density and stable hydrogen evolution even at a lower incident power of 13 mW/cm^2, which will further increase by increasing the input power.

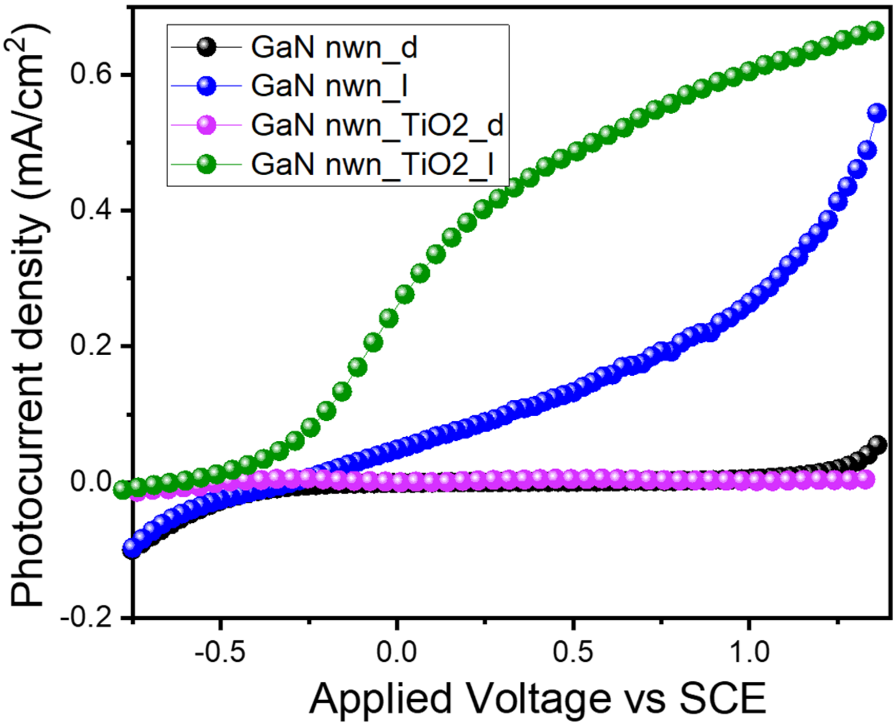

Figure 3.7 Photocurrent density vs applied voltage for GaN nwn and GaN nwn/TiO$_2$

Also, the Incident Photon to Current Conversion Efficiency (IPCE) is calculated by using the formula [142,160]

$$IPCE = 1240 * J(mA/cm^2)/(\lambda(nm) * P(mW/cm^2))$$

where J is the photocurrent density, λ is the wavelength of incident light and P is the power of incident light. The IPCE values estimated at an incident wavelength of 360 nm and power of 13 mW/cm^2 are estimated to be 17% and 6% for TGN and TGE structures, respectively at 1.24V, indicating the improved light absorption and enhanced charge carrier separation for TGN. Thus, the NWN morphology based heterostructures show enhanced performance both in light absorption and carrier separation.

By using the experimental results obtained from the absorption, CL and the XPS-VB spectra, we draw a band diagram for TGE and TGN heterostructures under illumination and are shown in Figure 3.6b. The band edge positions of TiO_2 and GaN suggest that the TiO_2/GaN heterostructures is in type II form, which is the most favorable for water splitting applications. For n-type GaN semiconductors, the Fermi level is close to the CB and for p-type TiO_2 the Fermi level is close to the VB. When a p-n junction is formed, the Fermi levels align (at the equilibrium state), resulting in band bending. As evident from the figure, the upward band bending in n-GaN and the downward band bending in p-TiO_2 is more for TGN (1.84 eV) compared to those in TGE (1.4 eV). Therefore, in TGN, upon light excitation, transfer of the photogenerated charge separation is more and is further enhanced with the application of an external bias to show an overall improvement in water splitting efficiency of TGN. Also, Figure 3.7 show the comparison of photocurrent densities of GaN nwn and GaN nwn/TiO_2 heterostructure, and the heterostructure showed better performance compared to GaN nwn due to band bending in heterostructure as mention earlier.

3.1.4 Inferences

The XRD and Raman experiments confirm the anatase crystal structure of TiO_2, and SEM images show the conformal coating of TiO_2 on GaN. The photoelectrochemical properties of TiO_2/GaN heterostructure with two different morphologies of GaN were studied, and the structure with GaN nanowall network morphology (TGN) showed a better photoelectrochemical response with a photocurrent density of ~0.65 mA/cm^2 and an IPCE of 17% compared to 0.24 mA/cm^2 and 6% of planar GaN based heterostructure (TGE), at an applied bias of 1.24 V and at an incident power of only 13mW/cm^2. The chronoamperometric analysis also showed very high stability of both electrodes. The better photo response in TGN was shown to be due to the appropriate band bending at the interface, and the improved light absorption was attributed to the NWN morphology. The p-n diagram showed a higher barrier height for TGN structure which favors photogenerated charge separation. For this system Hydrogen bubbles were observed.

The study clearly demonstrates that the water splitting efficiency can be greatly enhanced by fabricating TiO_2/InGaN heterostructures. Optimizing the thickness of TiO_2 and indium concentration (band gap engineering) to tune the band gap to an appropriate value can lead to very high efficiency in photochemical activity.

3.2 InGaN/TiO_2 Heterostructure photoelectrodes†

3.2.1 Introduction

Among the semiconducting materials that are investigated to be fabricated as photoelectrodes for water splitting, GaN is an important material due to its ability to tune the energy bandgap across the entire solar spectrum by alloying with indium and its suitable alignment of the band edge for water oxidation and reduction under visible irradiation, render it as a highly potential candidate for solar water splitting. The energy conversion efficiency for III-nitride semiconductors is still low and a maximum theoretical STH conversion efficiency of 27% is predicted for $In_xGa_{(1-x)}N$ with an energy bandgap around 1.7 eV with appropriate conduction and valence band edge positions[161–163]. The large difference in interatomic spacing between GaN and InN and the low dissociation temperature of InGaN, makes the growth of InGaN alloys challenging, as it gives rise to compositional inhomogeneity and strains that strongly affect the optical properties of the InGaN layers. InGaN with different In compositions significantly improves the solar light absorption from UV to the visible region. Also, the fabrication of suitable hetero junctions enhances the extraction of photo-generated electrons and holes to the respective electrodes by reducing the interfacial resistance.

In the previous section, TiO_2/GaN nanowall network heterostructure as a potential photoelectrode for efficient charge separation[164]. The combination of InGaN with optimum In concentration and the fabrication of its heterostructure would lead to hydrogen generation with good conversion efficiency. Here, we discuss on the growth of single crystalline InGaN nanostructures on sapphire at a low substrate temperature of 350 ˚C with two different indium incorporation of 13 and 16% with good optical and electronic properties and evaluate its performance as a photoelectrode for water splitting. Also, we investigate the photoelectrochemical performance of InGaN nanostructures with the two different In compositions by forming hetero structures with a TiO_2 coating deposited by atomic layer deposition (ALD), which shows a significant enhancement in its photoelectrochemical performance.

---

† **Shivaram, B. K.**, Saraswathi Chirakkara, and S. M. Shivaprasad. "Effect of minute compositional variations on the photoelectrochemical properties of InGaN/TiO2 heterostructure electrodes." Applied Surface Science 539 (2021): 148251. © 2020 Elsevier B. V. All rights reserved.

3.2.2 Experimental methods and characterization:

InGaN nanostructures with different In compositions were directly grown on (0001) sapphire substrates by PAMBE system. InGaN/TiO_2 heterostructures ($In_{0.13}Ga_{0.87}N/TiO_2$ called as HS1 and $In_{0.16}Ga_{0.84}N/TiO_2$ called as HS2) were fabricated by depositing TiO_2 on InGaN nanostructures by ALD. The sapphire substrates are thermally degassed at 600 ˚C for 1 hour in the preparation chamber and then at 800 ˚C for 30 minutes in the growth chamber, prior to the growth of InGaN. The Gallium K- cell during the growth was held at 1075 ˚C ($3.97x10^{-7}$ torr) and the N_2 flow rate during growth is maintained at 1.5 sccm while an RF nitrogen plasma generator with a set power of 300 W is used to generate the nitrogen plasma. The substrate temperature during the entire growth was held constant at 350 ˚C and the In composition in the films was controlled by varying the In K cell temperature as 770 ˚C (BEP ~$1x10^{-7}$ torr) and 780 ˚C (BEP~ $1.2x10^{-7}$ torr) by keeping all the other growth parameters constant. A 70 nm of TiO_2 was coated using the same parameters as discussed in the previous section of this chapter.

3.2.3 Results and discussion

The Deposited samples are characterized by different techniques discussed here.

3.2.3.1 Morphology

In a previous report, we have shown that the GaN/TiO_2 heterostructure is a promising photoelectrode for efficient water splitting[164]. In the present study, we incorporate In in GaN in a controlled manner and evaluate the feasibility of the InGaN/TiO_2 heterostructures as a photoelectrode. Since the optoelectronic properties of any device depend on its surface morphology, we first record the morphology of the grown nanostructures by FESEM and AFM. Figure 3.8 a&b shows the top view FESEM images for samples S1 and S2. The sample with high In content (S2) showed larger grain sizes and improved crystallinity. The EDS elemental mapping acquired from the samples (shown in Figure 3.8 c&d) exhibits the uniform distribution of Ga, In and N and the In composition in S1 and S2 are found to be 12% and 16%, respectively. The AFM images (Figure 3.8 e&f) of S1 and S2 also showed granular morphology with average RMS roughness to be 40 nm and 42 nm, respectively. Figure 3.9 shows a selected area surface morphology of the heterostructures HS1 (Figure 3.9a) and HS2 (Figure 3.9b), with a clear interface of InGaN and TiO_2 visible. The inset of Figure 3.9a and Figure 3.9b shows the magnified image of TiO_2 for better clarity.

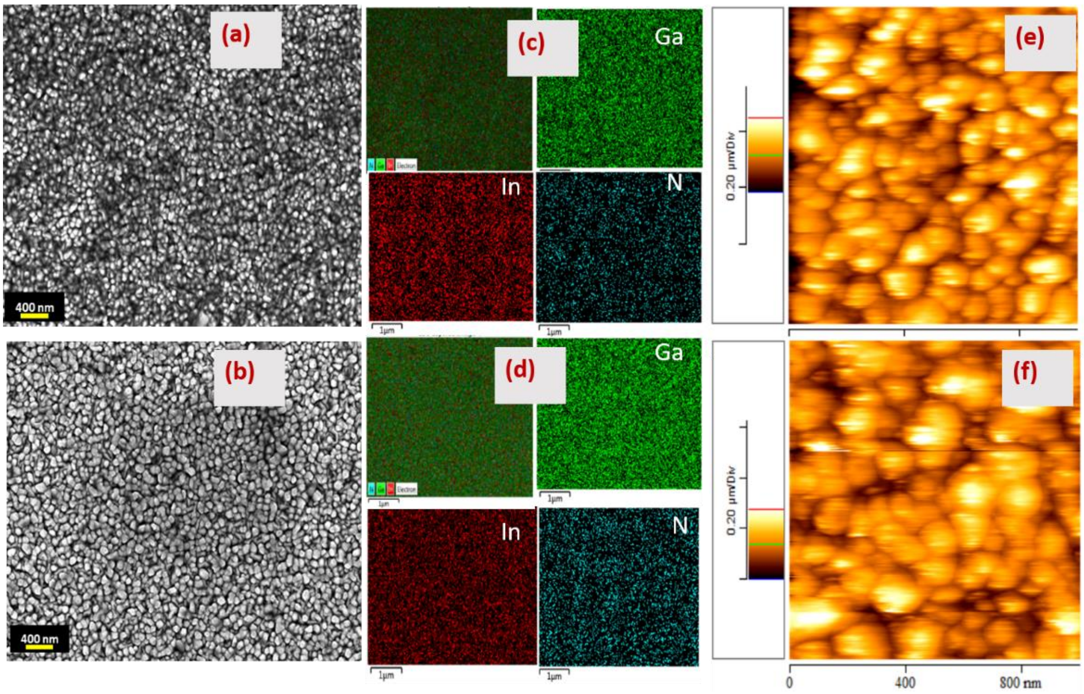

Figure 3.8 (a) and (b) show the FESEM surface morphology and (c) and (d) show the elemental mapping of the InGaN samples S1 and S2. (e) and (f) show the atomic force micrograph (AFM) of samples S1 and S2 at a scan area of 1X1 μm^2

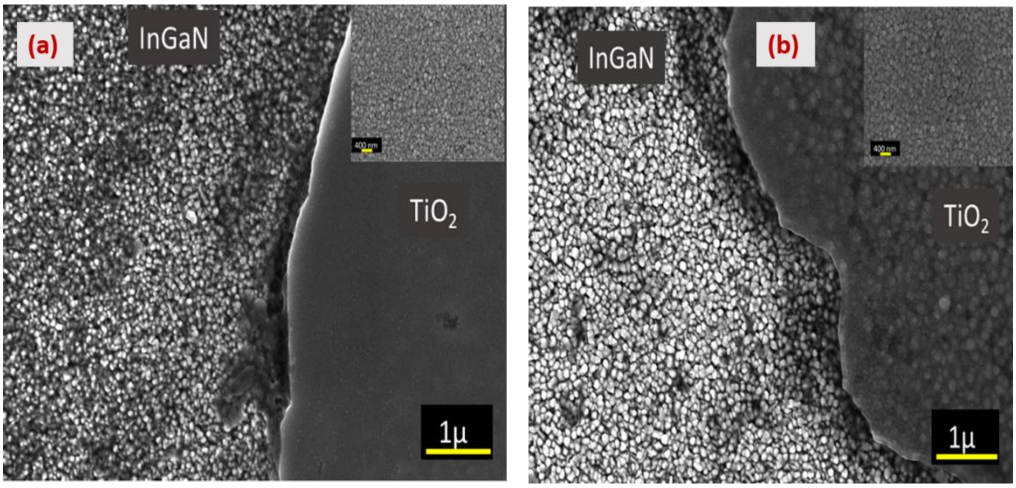

Figure 3.9(a) and (b) the surface morphology of the heterostructures HS1 and HS2. The inset shows the magnified image of TiO_2 *for better clarity.*

3.2.3.2 RHEED and Structural Properties

InGaN samples S1 and S2 are characterized by using the RHEED technique in the MBE chamber after the completion of deposition. The patterns are shown in Figure 3.10, which shows dotted patterns, indicating the three-dimensional growth of InGaN thin films. The crystalline and structural quality of the samples are analyzed by XRD. The XRD of the heterostructures HS1 and HS2 are shown in Figure 3.11. The XRD pattern shows that all the peaks are indexed to either the hexagonal InGaN phase or the tetragonal anatase TiO_2 phase making it suitable for efficient water splitting[150]. The small shift in the (0002) peak position suggest that there is a difference in In incorporation in the samples with slightly different lattice parameters. The InGaN (0002) peak for the samples S1 and S2 are broad with multiple peaks that appear due to the presence of different compositional phases. The peak is de-convoluted into three peaks, and the In composition is extracted by using Vegard's law.

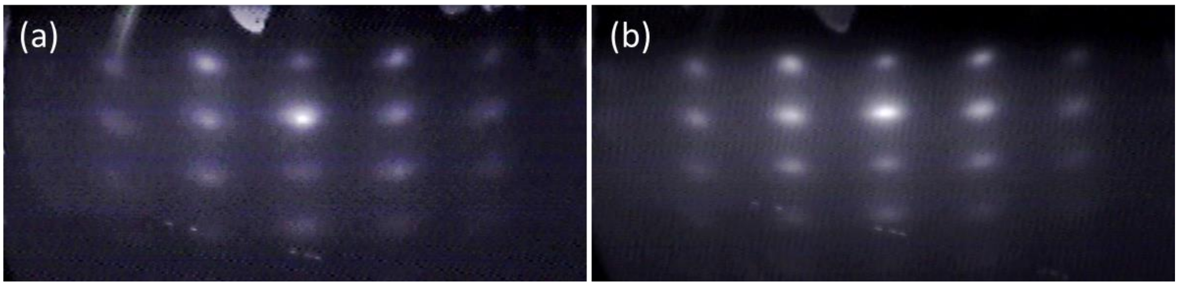

Figure 3.10 RHEED patterns of the grown samples (a) S1 and (b) S2.

$$c^{In_xGa_{(1-x)}N} = x c_o^{InN} + (1-x) c_o^{GaN} \tag{3.1}$$

where 'c' is the lattice parameter of InGaN and c_o^{InN} and c_o^{GaN} are the lattice parameters of InN (5.7064 Å)[165] and GaN (5.1852 Å)[166]. 'x' is the composition, and the values of 'x' are extracted to be 13% for sample S1 and 16% for sample S2, respectively.

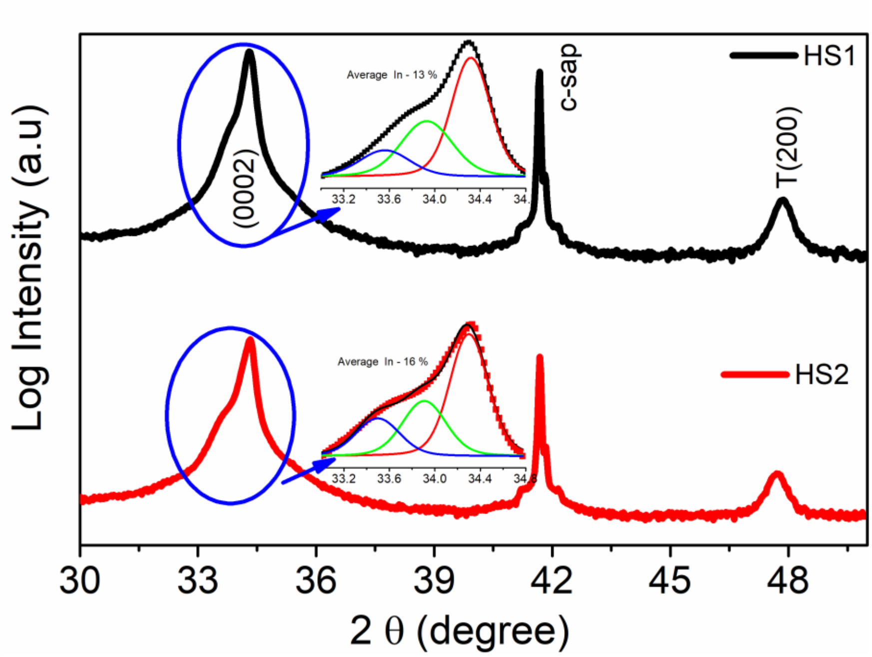

Figure 3.11 X-Ray diffraction of the InGaN/TiO_2 Heterostructures. The inset shows the magnified and de-convoluted (0002) peak.

3.2.3.3 XPS Studies

We performed the XPS to study the variation in the electronic structure and to estimate the In incorporation in the grown structures by looking at the core levels and the valence band spectra. Figure 3.12(a,b,c) shows the core level spectra of In3d, Ga 2p and N 1s for samples S1 and S2. A small shift in binding energy with increasing In concentration is observed in all the core level spectra. The N1s core level spectra are also de-convoluted into multiple peaks using Shirley baseline correction and Voigt fitting. The peak around 398 eV in S1 and 397 eV in S2 correspond to the N-Ga bonding whereas the other two peaks in both samples are the Ga Auger peaks. Using the atomic sensitivity factors the In composition in all the grown structures is extracted and is found to be 12 % and 15 %, which is fairly in good agreement with values obtained by EDS and XRD.

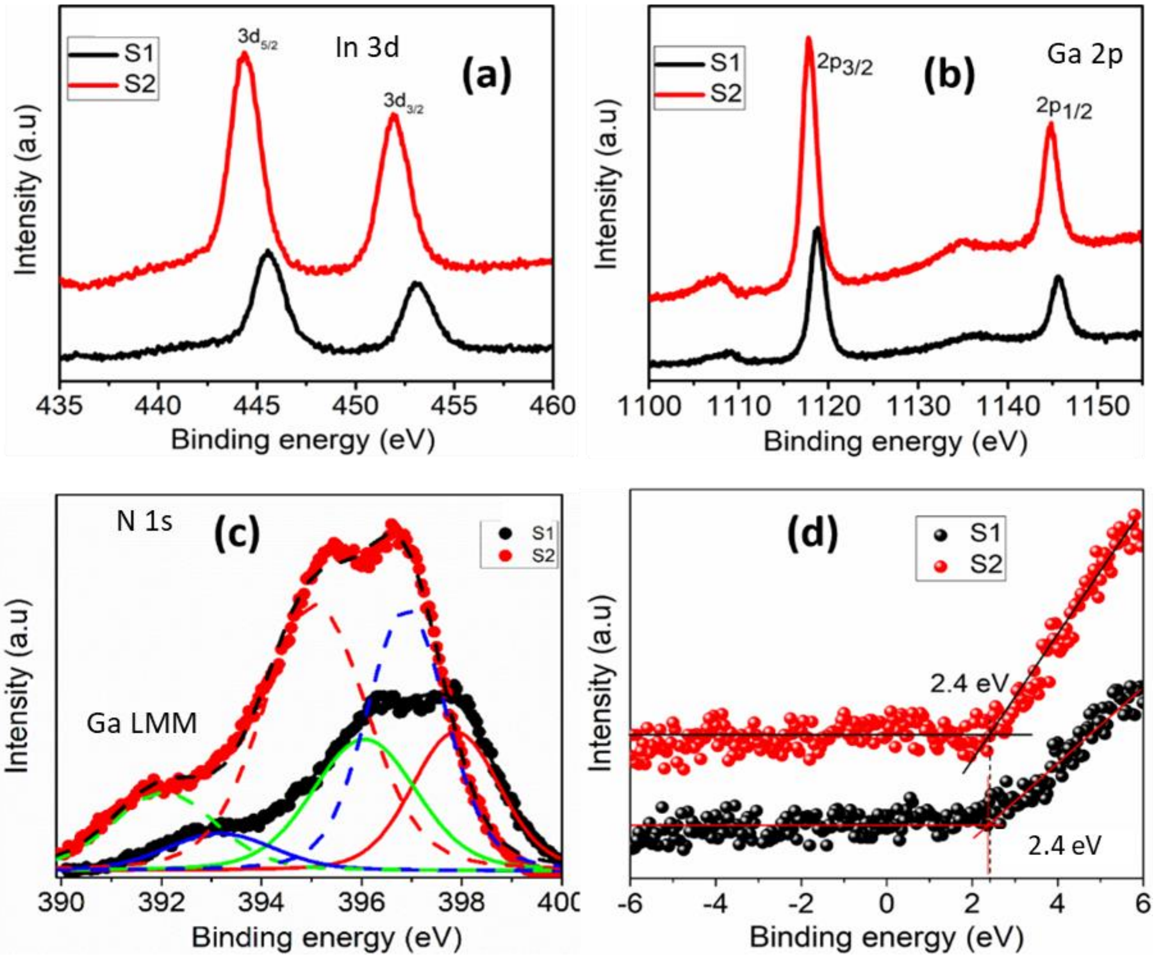

Figure 3.12(a,b,c) shows the core level spectra of In, Ga, and N, and (d) shows the valence band spectra from samples S1 and S2. In (c) the dashed and the solid curves show the de-convoluted N1s spectra for both the samples.

XPS was also utilized to determine the separation of the surface Fermi level from the valence band maximum (VBM) for the InGaN samples. The valence band spectra of the samples with different In concentrations are shown in Figure 3.12d. The position of the VBM with respect to the surface Fermi level was determined by extrapolating the leading edge of the valence band photoemission spectra to the intersection with the background. This yielded a VBM to surface Fermi level separation of 2.4 eV for both S1 and S2. The small shift in VBM shows a slightly increased charge carrier concentration in S2.

3.2.3.4 Optical Properties

In order to study the optical properties of the heterostructures, we have used UV/Vis absorption and photoluminescence (PL) spectroscopy. Figure 3.13a shows a systematic change in absorption edge towards the visible band with increased In incorporation. The energy band gaps extracted from the Tauc plot of the heterostructures, yield values of 2.92 and 2.82 eV for InGaN of the two different In compositions, with the solar absorption range now in the visible region. Figure 3.13b shows the room temperature PL spectra of the samples with different In concentrations. We observe a significant change in the PL spectra of InGaN compared to the GaN (3.4 eV). PL shows a broad emission in the visible region with a peak center around 2.35 eV and 2.22 eV for samples S1 and S2, depicting the change in bandgap with the incorporation of indium. Broader emission peaks can originate from the compositional phase variations, which was also evident from the de-convoluted XRD peaks (refer to figure 3).

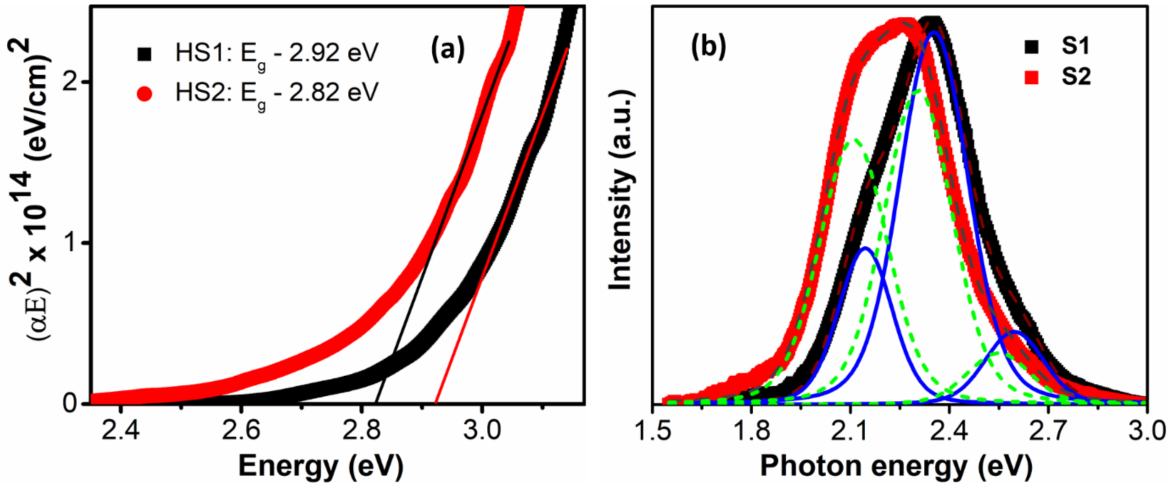

Figure 3.13(a) shows Tauc's plot extracted from the Uv-Visible spectroscopy for HS1 and HS2 and (b) the room temperature PL emission from samples S1 and S2.

The PL band edge emission peaks are de-convoluted into three peaks with centers at 2.15 eV, 2.35 eV and 2.60 eV for S1 and 2.11 eV, 2.30 eV and 2.55 eV for S2 as shown in figure 1.8 (b). From the absorption and the PL studies, we can see a positive Stokes shift with a value of around 0.57 eV and 0.60 eV for S1 and S2, respectively. This is attributed to the carrier localization in the Urbach tail states [167] that appear near the band edge of the material, as seen in XPS valence band spectra. For InGaN system, the Stokes shift increases with increasing In incorporation. Such shifts have implied in the literature[168,169] the presence of localized carrier states, which arise from the random distribution of In atoms or due to the formation of In-rich quantum dots. For higher In content, the In segregation increases and the localized states go deep, resulting in an increased red shift.

3.2.3.5 Photoelectrochemical and Hall Measurement Studies

To study the influence of In content and the impact of heterojunction on the photoelectrochemical properties, we performed solar water splitting experiments on InGaN and its heterostructures, by electron beam evaporation coating of Ti/Al (30/70 nm) ohmic contacts and annealed at 700 °C for 5 minutes. Figure 3.14a shows the photocurrent density as a function of applied potential for the samples S1, S2, HS1 and HS2 photoanodes in 1M Na_2SO_4 solution under both dark and illuminated (A.M 1.5G one sun) conditions. The photocurrent density increased with the applied potential, and with increased In content (inset of Figure 3.14a), and is attributed to the enhanced light absorption because of the reduced energy gap and the improved photo-generated charge separation. Because of the reduced bandgap, with In content, the conduction band edge shifts towards the reduction potential of water and consequently favors PEC water splitting. Also, the effects of change in In composition on the electrical properties of InGaN thin films are studied by room temperature Hall measurement system. The electrical measurements showed a significantly improved electron mobility of 123 $cm^2V^{-1}s^{-1}$ for S2 compared to 10 $cm^2V^{-1}s^{-1}$ for S1 at room temperature. The morphology in figure 1 shows that the grain size of S2 is larger than in S1, which appears to facilitate reducing the grain boundary scattering, and consequently enhancing the electron mobility.

As shown in Figure 3.14a, compared to the structures S1 and S2, the heterostructures HS1 and HS2 showed better photocurrent. Figure 3.14b shows the variation in photocurrent for S1 and HS1 and (c) for S2 and HS2 for better clarity and comparison. In a previous section, we stated that because of the interfacial band bending the photocurrent density improves with the use of GaN/TiO_2 heterostructure as a photo anode[164]. The Hall measurements show that the InGaN films have n-type and TiO_2 has p-type conductivity.

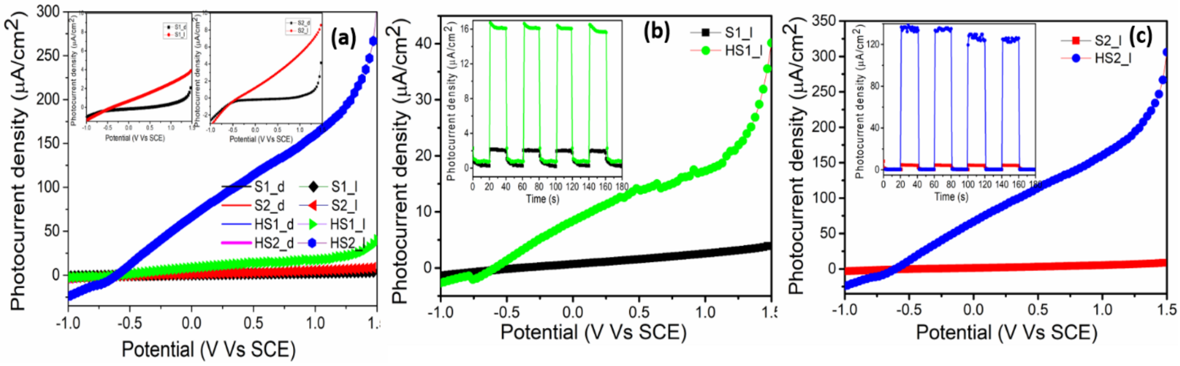

Figure 3.14(a) Photoelectrochemical (PEC) properties of InGaN and heterostructure photoelectrodes under AM 1.5 G 1 sun illumination. Inset shows PEC of samples S1 and S2 for better clarity. Figure (b) shows the variation in photocurrent for S1 and HS1 and (c) for S2 and HS2 for better clarity and comparison. The inset of (b) and (c) shows the transient response of InGaN and their heterostructures under illumination ON/OFF conditions under a constant applied potential of 0.8V Vs SCE. _d and _l postscript indicate dark and illuminated conditions.

Also, as per the band edge positions of InGaN and TiO_2, their heterostructure will be in type- II form. In Figure 3.15, we have sketched the band diagram of the system by using the data from UV-Vis and XPS valence band spectra. From XPS valence band spectra we obtained the VBM for S1 and S2 as 2.37 and 2.40 eV, respectively. We reported the VBM for ALD grown TiO_2 as 1.21eV[164]. The observed improvement in current density in HS1 and HS2 may thus be attributed to the interfacial band bending as shown in figure 1.10. Also, from the figure we can see that the band bending is more for HS2 than HS1, thus making HS2 yield better photocurrent density than HS1. Among all the photoelectrodes studied, HS2 showed the highest photocurrent density of ~160 μA/cm^2 at 1.0 V and an onset potential of -0.6 V vs SCE. The onset and saturation potential shifts slightly negative for InGaN/TiO_2 with respect to the InGaN photoanodes.

To understand more on the recombination or the charge separation process happening in the two compositions, we have done the transient photo response studies of the device by turning the light ON and OFF periodically at a fixed applied bias potential. The insets of Figure 3.14 b&c demonstrate the temporal photo response measured for InGaN and their heterostructure photoelectrodes under illumination with 20 seconds on/off conditions at an applied potential of 0.8 V_{SCE}. Every sample showed a fast response upon ON and OFF conditions, while the photocurrent density is significantly different with the fabrication of heterostructures.

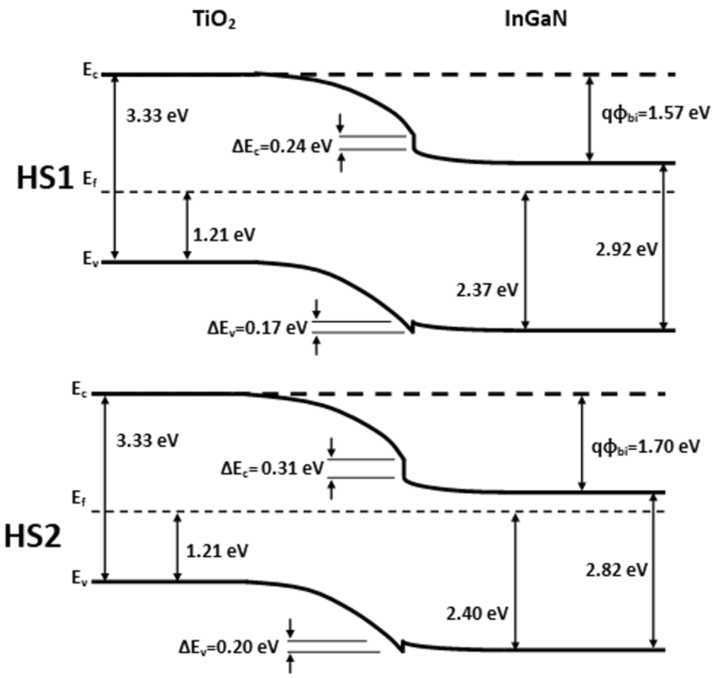

Figure 3.15 Band diagram for heterostructures HS1 and HS2 under equilibrium condition

3.2.4 Inferences

In summary, a highly controlled growth of InGaN nanostructures at a relatively low substrate temperature of 350 °C with a very small (3 to 5 %) In composition difference and the fabrication of InGaN/TiO_2 heterostructures by coating it with TiO_2 by ALD, were discussed. The structural, morphological, optical, and photoelectrochemical properties were studied. The In concentrations were extracted to be 13% and 16% from XRD by using Vegard's law. The energy band gap extracted from the Tauc plot and the emission peak observed from room temperature photoluminescence showed absorption and emission in the visible region and good transient photo response characteristics. The InGaN/TiO_2 structure with higher In composition showed a higher photocurrent density due to improved light absorption and enhanced charge separation because of interfacial band bending. A small variation in In composition is observed to make a significant difference in the photocurrent density of heterostructures.

Chapter 4
$In_xGa_{1-x}N$ thin films grown on c-sapphire

This chapter discusses the growth of InGaN on c-Sapphire using different growth parameters like growth temperature, nitrogen flow rate, thickness, and metal fluxes (indium and gallium) and describes their effect on properties like crystal quality, morphology, optical properties, and mainly photoelectrochemical properties.

4.1 Role of surface morphology on PEC properties of $In_xGa_{1-x}N$ grown on c-sapphire

4.1.1 Introduction

The optoelectronic properties of semiconductor nanostructures strongly depend on their surface morphology, crystal structure, and composition. Semiconductor nanostructures with a high surface area to volume ratio, good crystalline quality and good light absorption or extraction properties are desirable for many optoelectronic devices such as solar cells,[170] photodetectors,[171–173] and photoelectrochemical hydrogen generation,[142,146,159,174–179] etc. Converting solar energy into storable chemical energy by photoelectrochemical (PEC) water splitting is a clean, renewable and attractive approach. Generally, the incident photon conversion efficiency (IPCE) for PEC water splitting is low owing to certain limiting factors such as low absorption, weak charge carrier separation, or weak chemical reaction at the electrode-electrolyte interface.

PEC hydrogen generation by solar water splitting is intensely being pursued by researchers to find semiconductor photoelectrodes that enable high-efficiency water splitting. In recent years, GaN has received great research interest in PEC water splitting because of its outstanding electrical properties like carrier mobility, conductivity, and high chemical stability along with its ability to alloy with In to tailor its band-gap in the visible spectral region.[142,172,174,175,177,180] Since the photocurrent density exhibited by a semiconductor photoelectrode for PEC water splitting is primarily determined by the band-gap energy (Eg) of the semiconductor, the formation of InGaN structures with the desired band-gap enables the optimization of the optoelectronic properties. Further, fabricating InGaN nanostructures also results in an increased surface area that adds to its efficiency.[181,182] The effects of In composition on the optical bandgap of InGaN alloys are reported theoretically and experimentally by many groups using different tools/methods.[169,172,183–185] The formation of single-phase crystalline InGaN films at relatively low temperatures is a challenge to crystal growers, due to the low dissociation energy and low miscibility of In, resulting in phase separation which has deleterious effects on their electrical and optical properties of the material[186–188]. InGaN nanostructures have been extensively applied for the fabrication of PEC water splitting devices owing to their tunable bandgap, large surface area, and good chemical stability.[176,189,190] From the published literature, it can be inferred that appropriate nanostructures have great potential for the improvement of photocatalytic activities.[190–192] The photocurrent density can be influenced by the morphology or the surface-to-volume ratio, crystal orientation, thickness, mobility, and electrical conductivity of the semiconductor photoelectrode. Many researchers have tried to optimize these factors to enhance the light absorption of the photoelectrode material as well as to reduce the electrical losses, that reduce the electrochemical reaction.[163,193,194]

In the previous chapter, we discussed the fabrication of GaN nanowall network structures and their improved visible light absorption efficiency due to the increase in the surface area to volume ratio.[164] Here, we worked on the fabrication of InGaN nanostructures with different In composition and morphology by MBE and evaluate their utility as a photoelectrode in a PEC water splitting set-up. In order to improve solar energy utilization, we have grown InGaN with different In concentrations, which is achieved by varying the substrate temperature systematically. Different morphologies with a difference in surface areas are achieved by controlling the growth parameter like N_2 flow rate and growth duration. We have analyzed the structural, morphological, optical, and electronic properties of InGaN structures by SEM, XRD, UV-Vis Spectroscopy, Physical Property Measurements System (PPMS), etc. We test the photoelectrochemical properties by using these InGaN nanostructures as photoelectrodes and observe the PEC activity, which reveals that the InGaN structures with a high surface to volume ratio show a remarkable increment in the generated photocurrent density.

4.1.2 Experimental methods and characterization techniques

The InGaN structures are grown on epi GaN templates by PAMBE operating at a base pressure of 10^{-10} torr by systematically varying the growth parameters. In this work, we have grown 7 InGaN samples, of which 3 are formed at different substrate temperatures and in the remaining 4 cases the substrate temperature is maintained at 350 °C while other parameters are varied. Out of these four, 2 samples have different growth durations (different thicknesses) and the others are formed at different N_2 flow rates. In all the cases the plasma forward power is kept at 300 W and the In-K cell temperature is held at 840 °C and the Ga-K cell temperature is held at 1000 °C. The experimental growth parameters are tabulated below in Table 4.1.

Table 4.1 Experimental parameters for thin film growth of InGaN with different substrate temperature, thickness, and nitrogen flow rate.

Set	**Sample/ Label**	**Sub. Temp. (°C)**	**Ga K cell temp. (°C)**	**In K cell temp. (°C)**	**N_2 flow (sccm)**	**Duration**	**N_2 Plasma power (W_f)**
Set 1	350 °C	**350**	1000 ($4x10^{-7}$ torr -BEP)	840 ($3.4x10^{-7}$ torr -BEP)	1.5	1hr (400 nm)	300
	375 °C	**375**					
	400 °C	**400**					
Set 2	190 nm	350	1000	840	1.5	**½ hr(190 nm)**	300
	1000 nm				1.5	**3 hr(1000 nm)**	
	2.5 sccm				**2.5**	1hr (400 nm)	
	3.5 sccm				**3.5**	1hr (400 nm)	

Prior to the growth, the epi GaN coated sapphire substrates are chemically cleaned and thermally degassed inside the preparation chamber for an hour at 600 °C and followed by annealing in the growth chamber at 800 °C for 30 minutes. All the fabricated samples are analyzed using different preliminary characterization techniques. FESEM is used to examine the morphology. The crystal quality of the InGaN structures is identified by HRXRD. The room temperature optical properties of the structures are characterized by UV-Vis Absorption Spectroscopy and Photoluminescence Spectroscopy. The preliminary experiments using InGaN structures enabled the examination of the Photoelectrochemical (PEC) activities of each structure and studied its variation with In composition and morphology. The PEC properties are measured by using a Keithley 2450-EC lab system. The experiments were performed with a conventional three-electrode system, using a saturated calomel electrode (SCE) as the reference, a platinum coil as the counter electrode, and the fabricated InGaN devices as the working electrodes, and the external electrical contacts are made on the InGaN structures. 1M Na_2SO_4 solution with a pH of 8.2 is used as the electrolyte and 300 W Xe lamp as the light source. The excitation power density was set constant in all the experiments (where the input power is 180 W) and the light irradiation on the sample is controlled with a visible band-pass filter to nullify the absorption from the bottom epi-GaN substrate. The temperature-dependent electrical properties like mobility, resistivity, and carrier concentration of the grown structures are analyzed by using the Physical Property Measurement System at a temperature span from 50 to 400 K.

4.1.3 Results and discussion

4.1.3.1 FESEM, HRXRD and AFM

We fabricate InGaN thin film photoelectrodes with different In composition and with different morphologies for photoelectrochemical water splitting. The In incorporation in InGaN is controlled by varying the substrate temperature, and the growth parameters such as thickness and N_2 flow rates are varied to obtain films of different morphology and thus different surface to volume ratio.

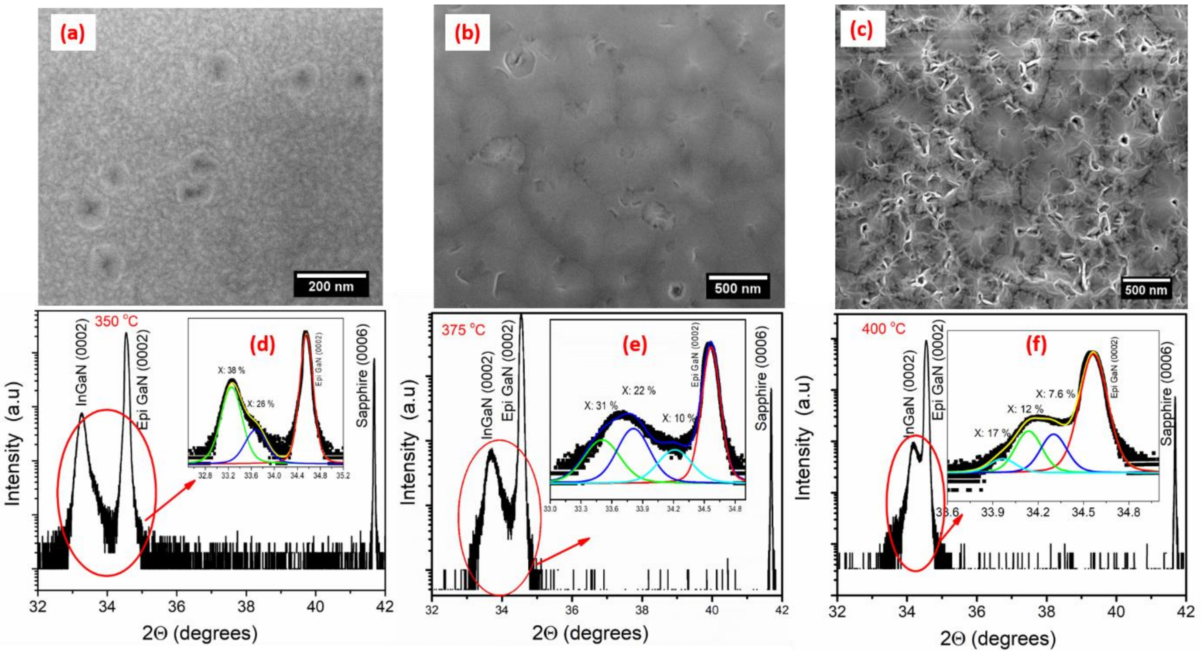

Figure 4.1 (a, b, c) Illustrate the FESEM images and (d, e, f) the symmetric 2θ-ω scans acquired by HRXRD for samples grown at different substrate temperatures 350 °C, 375 °C, and 400 °C. The inset shows the magnified and deconvoluted InGaN (0002) peak along with epi GaN (0002) marked

Figure 4.1 (a, b, c) shows the FESEM images, and (d, e, f) shows the HRXRD patterns of the InGaN samples grown at different substrate temperatures. The In compositions from EDS are noted to be 46, 32, and 14% for substrate temperatures 350, 375, and 400 ^{o}C, respectively, showing a decrease in In incorporation with an increasing substrate temperature, due to the low In-N bond energy. The images reveal that with increasing substrate temperature the surface roughness of the films is enhanced. At 400 ^{o}C, narrow thread-like formations cause an increase in the surface to volume ratio. The HRXRD measurements were used to understand the variation in crystallinity, structure quality, and In compositions of the grown thin films. The symmetric 2θ-ω scans are plotted in log scale for these samples and are shown in Figure 4.1 (d, e, f). It confirms that all the films are single crystalline wurtzite c-oriented structures. The peak observed at 41.68^{o} is from sapphire (0006) and the peak around 34.4^{o} is from the epi-GaN. The absence of any reflections from the InN confirms that crystalline InN phases are not present in the grown films. The InGaN peak positions are used to determine the c-lattice parameters and to calculate the In composition using Vegard's law.[165,166,195] The width of the

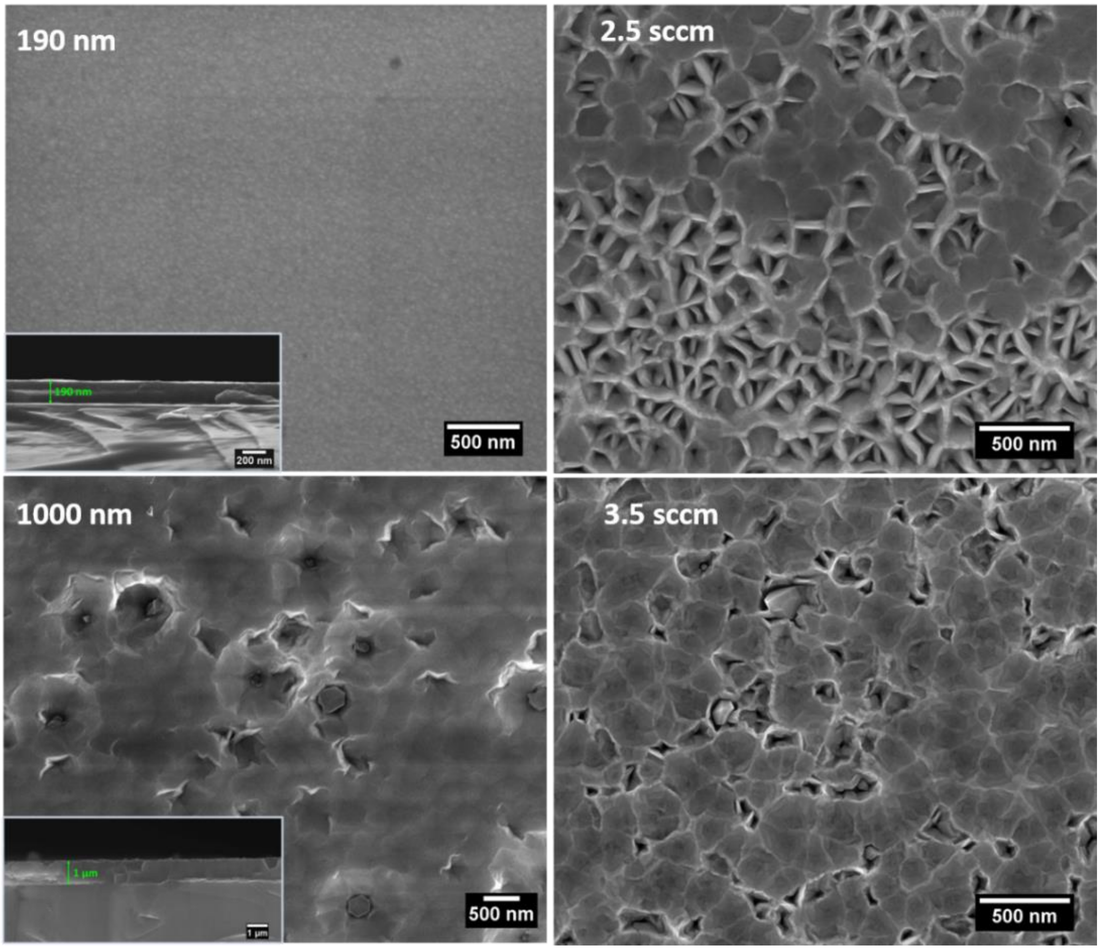

Figure 4.2 The FESEM images showing the difference in morphology of InGaN thin films with different thickness 190 and 1000 nm and different N_2 flow rates of 2.5 and 3.5 sccm. The inset of the figures shows the cross-sectional images of samples grown with different thickness

InGaN (0002) peak, reflects the phase separation in samples, which is seen to increase with increase in substrate temperature. The average In composition in all samples is estimated after de-convoluting the InGaN peaks into phasal components as shown in the inset of each XRD pattern. The intensity (area under the curve) of each phase reveals their respective In composition using Vegard's law and are marked in the respective patterns. The In compositions are found to be 35, 32, and 14 % for substrate temperatures 350, 375, and 400 ^{o}C, respectively. Though the sample grown at 400 ^{o}C showed an In incorporation of only 14 %, it also exhibited a high surface to volume ratio compared to the other two morphologies.

The photocatalytic activity of a photoelectrode can be improved by increasing the surface to volume ratio. In the first set of growth i.e by varying the substrate temperature, we have seen that the sample grown at 350 ^{o}C showed the highest In incorporation (35%), with relatively less phase separation but poorer surface to volume ratio. The growth parameters such as N_2 flow rates and the growth duration are varied in the second set of growth, to improve the surface to volume ratio of InGaN thin films without altering the In composition (~35 %) by holding the substrate temperature at 350 ^{o}C. Figure 4.2 shows the FESEM images for the samples grown in the second set i.e, at two different thicknesses (190 and 1000 nm) and two different N_2 flow rates (2.5 and 3.5 sccm). The images reveal that the morphology changed from a smooth to a rough nanowall networked structure with increasing growth duration. An increase in the N_2 flow rate also changed the surface roughness with the formation of nanowall network structure, but a further increase in N_2 flow rate reduced the surface roughness due to the filling of networks. As compared to Figure 4.1a, the surface to volume ratio is increased by increasing the growth duration and also by increasing the N_2 flow rate.

The HRXRD of the samples grown with different thicknesses and different N_2 flow rates (constant substrate temperature of 350 ^{o}C) are shown in Figure 4.3. These samples also showed broad c-oriented (0002) peaks with the wurtzite crystal structure and the average In compositions, extracted from the de-convoluted peaks using Vegard's law, are 35 and 31 % for 190 and 1000 nm thickness samples and 32.3 and 31.5 % for samples grown at 2.5 and 3.5 sccm, respectively. The result shows that the InGaN structures formed in set 2 have different morphology, but similar In composition (32 to 35 %). The insets in Figure 4.3 show InGaN phases with different In compositions.

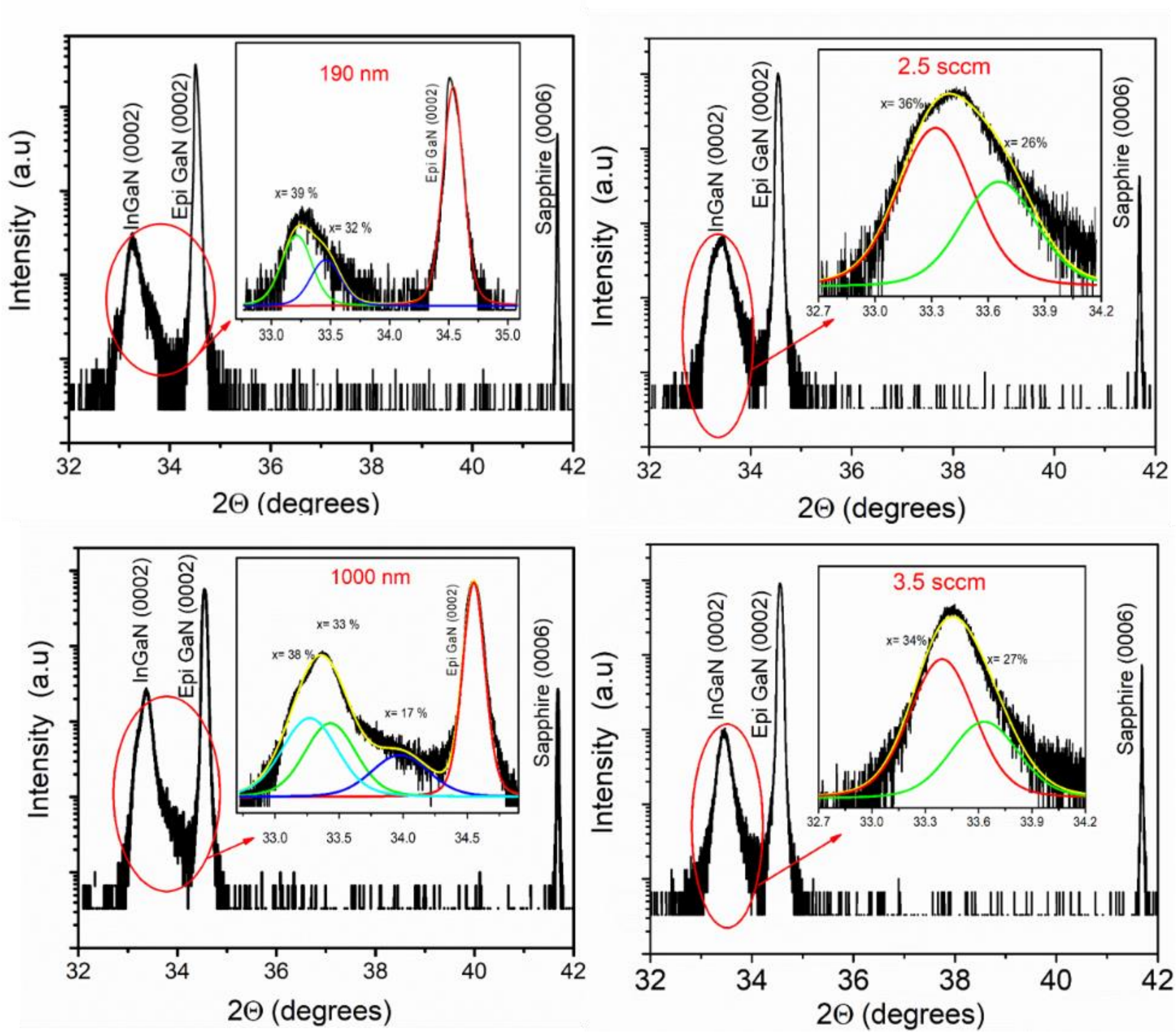

Figure 4.3 Symmetric 2θ-ω scans acquired by HRXRD from samples grown with different thicknesses and different N_2 flow rates.

To measure the surface roughness of the samples grown in the second set, we carried out AFM studies. Figure 4.4 shows the morphologies of these samples along with the reference sample. The measured roughness of these samples is tabulated in Table 4.2. As we increase the nitrogen flux and thickness of the samples, the roughness also increased.

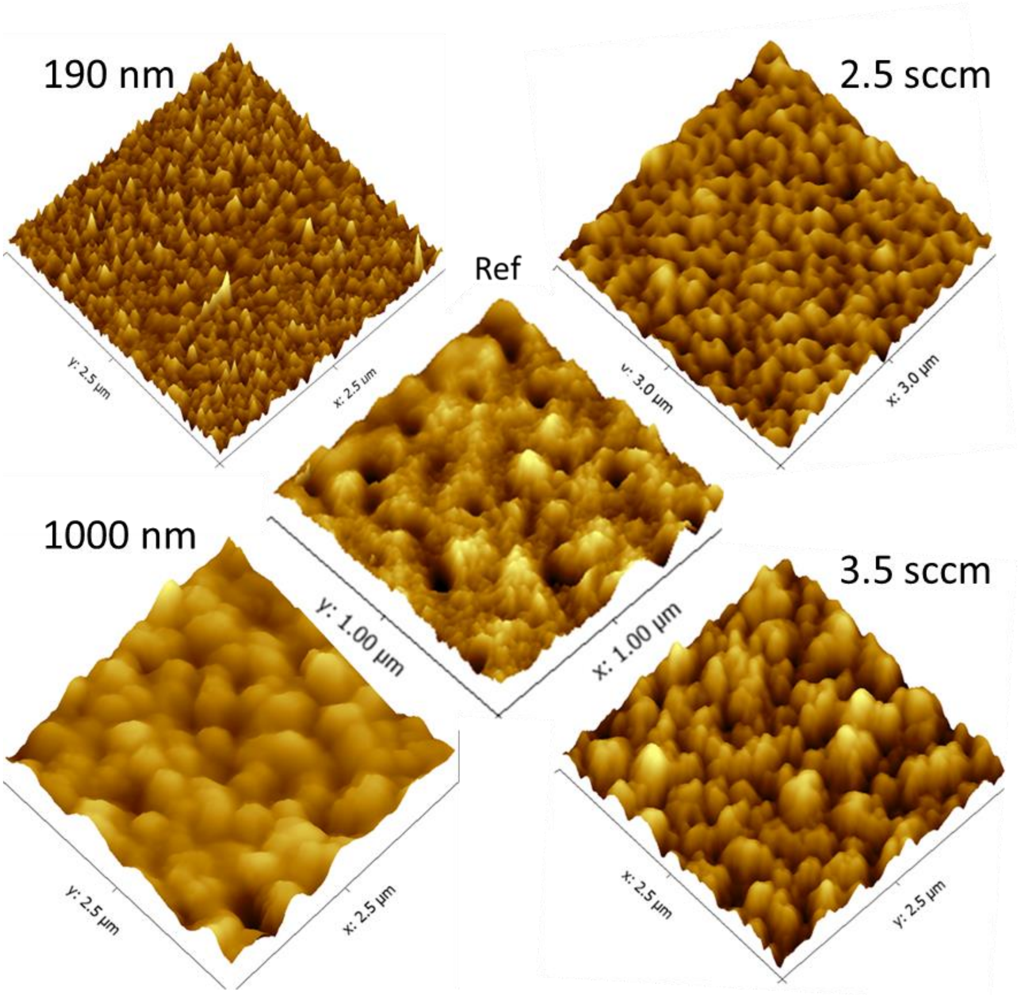

Figure 4.4 AFM images of the samples.

Table 4.2 Measured roughness of the samples.

Sample	**Rms Roughness (nm)**
190 nm	2.5
Ref.	3
3.5 sccm	26
2.5 sccm	31
1000	35

4.1.3.2 Optical properties

To understand the behavior of InGaN structures with different In incorporation and morphology, the optical properties of all the samples are studied first by UV-Visible absorption spectroscopy. The spectroscopic experiments are conducted in the absorption mode. The Tauc plots for InGaN samples grown in the first set (at different substrate temperatures) are shown in Figure 4.5a and those for the samples grown in the second set (with different thicknesses and N_2 flow rate) are shown in Figure 4.5b. We observe a systematic change in optical energy gap as a function of substrate temperature, indicating the variation in In content which is also evident from the XRD and EDS experiments. The extracted optical energy bandgaps from Tauc's plot are 2.30, 2.64, and 2.96 eV respectively, for 350, 375, and 400 °C substrate temperatures. The optical energy bandgap for the samples grown in the second set did not show much variation in the UV absorption characteristics. The energy bandgap values are 2.30 and 2.38 eV for 190 and 1000 nm thick films and 2.35 and 2.33 eV respectively, for those grown with 2.5 and 3.5 sccm N_2 flow rates. This implies that the In incorporation does not vary much with an increase in N_2 flow and thus there is not much change in the bandgaps of these samples.

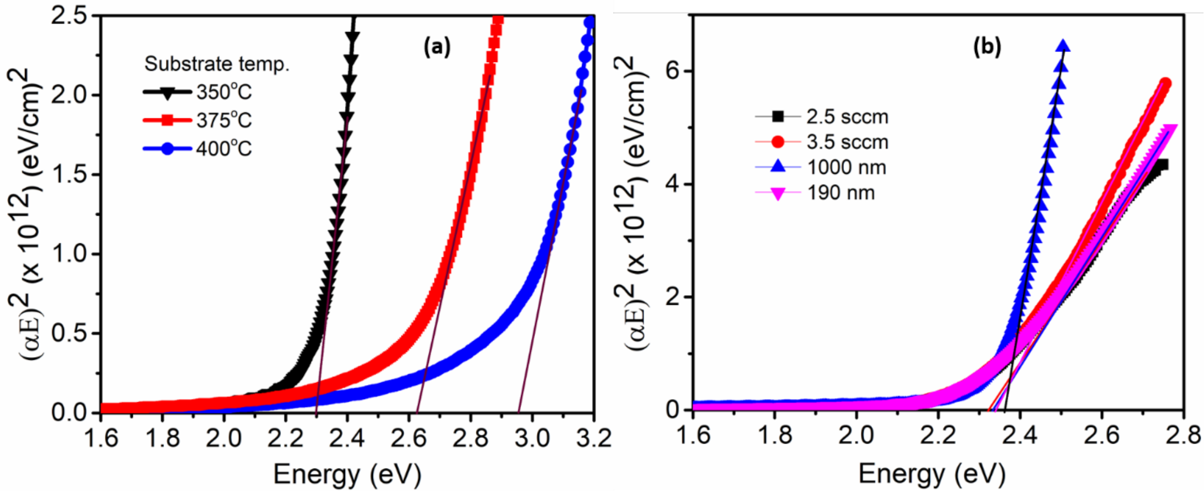

Figure 4.5 The Tauc plot for InGaN samples (a) grown at different substrate temperatures (b) at different thicknesses and different N_2 flow rates.

Further, to study the effect of In composition and morphology on the optical properties, we carried out room-temperature photoluminescence (RT-PL) experiments. As observed from absorption studies, the RT-PL also showed significant changes in peak positions for InGaN samples grown at different substrate temperatures, due to variation in In content (Figure 4.6a) PL showed a broadband edge emission and the broadness increased with the increase in substrate temperature. Broader emission indicates the compositional phase separation, which is increasing with the increase in substrate temperature, corroborating with the XRD results. The PL peaks are de-convoluted into two peaks for samples grown at 350 and 375 °C, and those grown at 400 °C were resolved into three components. The peak centers are at 2.17 and 2.04 eV for 350 °C and 2.45 and 2.12 eV for 375 °C, and for those grown at 400 °C are 2.20, 2.70 and 3.01 eV. As shown in Figure 4.6b, the PL spectra do not change much in peak position and width with the increase in thicknesses or with the increase in N_2 flow rates, suggesting similar phase compositions. The peak positions of 2.01 and 2.08 eV are observed for films of thickness 190 and 1000 nm, respectively, while the peak position is 2.03 eV for both 2.5 and 3.5 sccm N_2 flow rates. The optical studies showed that all the fabricated InGaN thin-film structures have their energy band in the visible region and that the samples grown at different N_2 flow rates and durations had differences only in their morphology but not in the In composition.

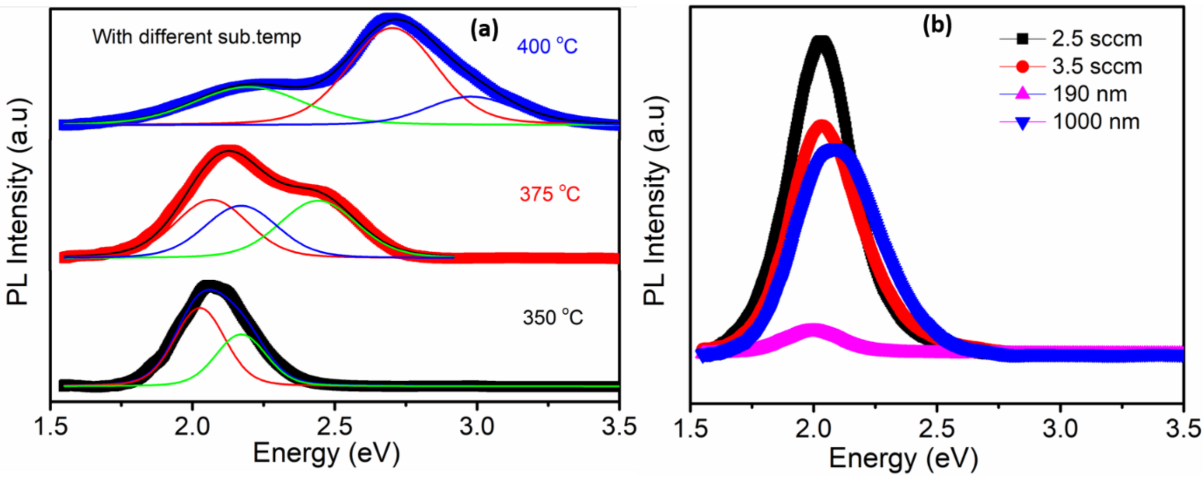

Figure 4.6 (a) shows the room temperature Photoluminescence of InGaN grown at different substrate temperatures (the peaks are de-convoluted into multiple peaks are shown) (b) for different thickness and N_2 flow rate together.

4.1.3.3 PEC and electrical Properties

To see the effect of change in the In composition due to different substrate temperatures and morphology on the photoelectrochemical properties, we carried out water-splitting experiments in a photoelectrochemical cell. Figure 4.7 shows the variation in photocurrent density as a function of applied potential using InGaN with different In concentrations (grown at different substrate temperatures, set 1) as working electrodes. In all the samples, we have seen a negligible dark current density and that the photocurrent density increases for films grown with increasing substrate temperature (ie, decreasing In composition). A photocurrent density of only 0.25 mA/cm^2 at 1V vs SCE is observed for the sample (grown at 350 ^{o}C) with the highest In content (35%) as compared to the 1.1 mA/cm^2 for the sample (grown at 400 ^{o}C) with the lowest In content (14%). Samples with the highest In content or lowest band-gap energy are expected to show high photocurrent density, but, in our case, the sample with the low In content has showed the highest photocurrent density (or good photoelectrochemical property).

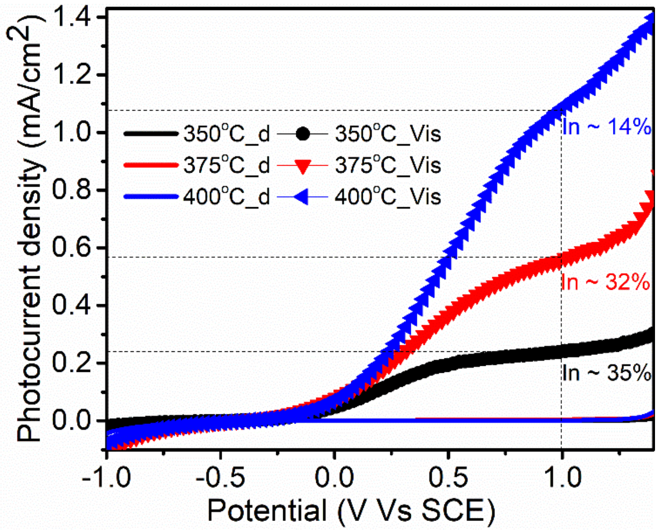

Figure 4.7 the variation in photocurrent density as a function of potential for InGaN photoelectrodes grown at different substrate temperatures (_d and _Vis indicate the dark and illumination condition with the use of a visible band-pass filter)

To understand this behavior, we studied in detail the electrical properties like mobility and conductivity of the formed InGaN structures by temperature-dependent Hall measurements (using PPMS). Figure 4.8 shows the variation in mobility and conductivity as a function of temperature for samples grown with different substrate temperatures. As shown in Figure 4.8 a&b the electron mobility and conductivity of the InGaN sample grown at substrate temperature 400 ^{o}C (~158 cm^2/Vs and 86 Ω^{-1}cm^{-1} at 300 K) are smaller compared to those of the sample grown at 350 ^{o}C (211.87 cm^2/Vs and 121.65 Ω^{-1}cm^{-1} at 300K). That means the electrical properties of the sample grown at 350 ^{o}C are better than those of the sample grown at 400 ^{o}C. Thus, we cannot attribute the higher photocurrent density observed in the sample grown at 400 ^{o}C only to the good electrical properties of the photoelectrodes, but the surface morphology also appears to play an important role in determining the photoelectrochemical activities. As seen from the FESEM (Figure 4.1c), because of the enhanced surface to volume ratio, the sample grown at 400 ^{o}C has got good electrode-electrolyte interactions. Upon light irradiation on the photoelectrode, with a large surface area, increased photogenerated electron-hole pairs are formed and the separated electrons move to the metal counter electrode and the holes diffuse to the semiconductor-electrolyte interface. Thus, the enhanced electron-hole pair formation due to the large surface area and electrode-electrolyte interaction appreciate the photoelectrochemical activity, compared to the sample grown at 350 °C, though having higher In incorporation.

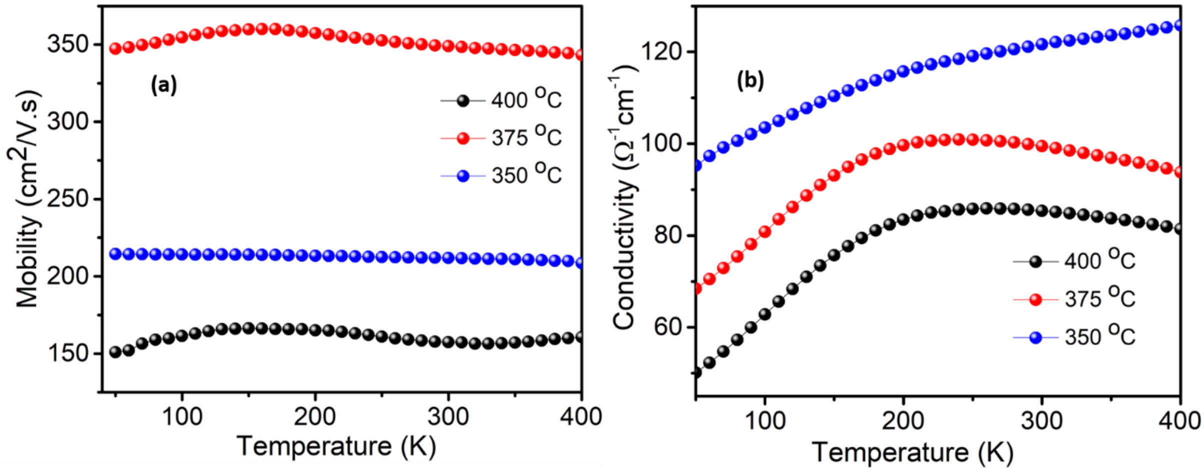

Figure 4.8 shows the variation in mobility and conductivity as a function of temperature for the InGaN samples grown at different substrate temperatures

Our study demonstrates the importance of photoelectrode morphology on photoelectrochemical properties. To understand more about how the morphology of the photoelectrode affects the photoelectrochemical activity, we have studied water-splitting experiments using InGaN samples having similar bandgaps but different morphologies. For this, we used the samples grown in the second set ie, at different thicknesses (190, 1000 nm) and different N_2 flow rates (2.5 and 3.5 sccm), whose SEM showed a difference in morphology with the same In incorporation. Figure 4.9 shows the variation in photocurrent density using InGaN photoelectrodes with different morphologies. For better clarity in comparison, the photocurrent density of the reference sample (the sample grown at 350 °C having a smooth surface morphology with an In composition of 35%) is also shown. All the samples showed better photocurrent density than the reference sample, except for the sample with a thickness of 190 nm. The photocurrent density increases from 0.25 (reference sample) to 0.90 mA/cm^2 (sample with thickness 1000 nm) at a potential of 1V vs SCE, just by varying the surface morphology.

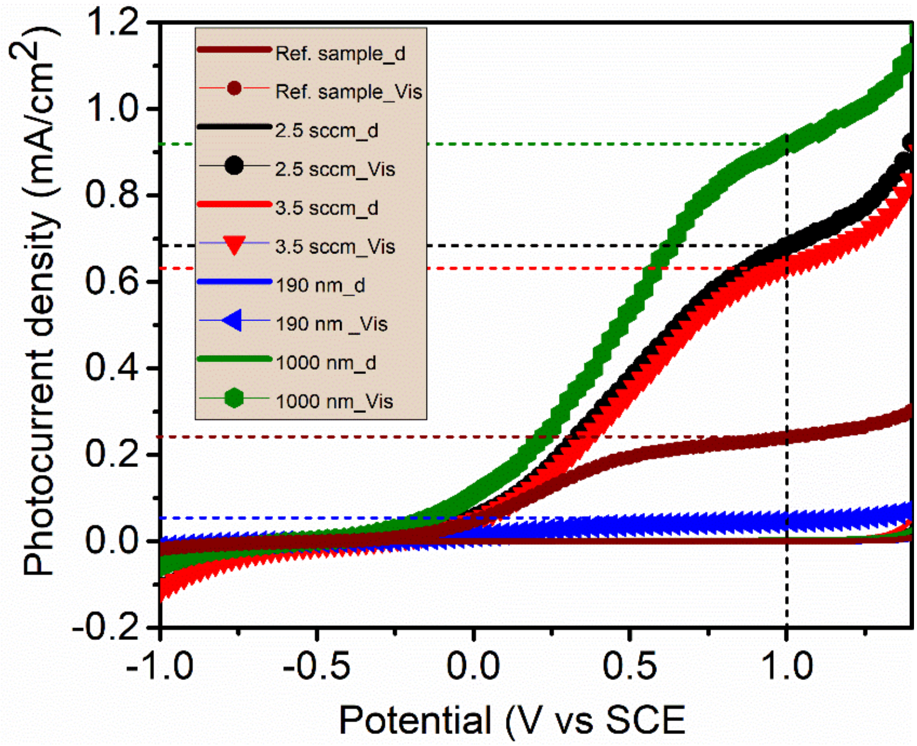

Figure 4.9 The variation in photocurrent density (under dark and illumination using visible band filter) as a function of potential for InGaN photoelectrodes with different morphology or samples grown with different thicknesses 190 and 1000 nm and different N_2 flow rates 2.5 and 3.5 sccm. The photocurrent density for the sample grown at 350 °C (reference sample) is also shown in the figure for a better understanding

To understand the effect of morphology on the electrical properties and thereby on the photoelectrochemical activities, we carried out the temperature-dependent Hall measurements of samples grown in set 2 with different morphologies. Figure 4.10 shows the variation in the mobility and conductivity as a function of temperature for samples grown with different morphologies. The sample with a thickness of 1000 nm showed good crystallinity, high mobility (~598 cm^2/V.s at 300 K), high conductivity (~142 Ω^{-1}cm^{-1} at 300 K), a better surface to volume ratio, and hence good photoelectrochemical activity. The sample with a thickness of 190 nm showed poor crystallinity, low mobility (~76 cm^2/V.s at 300 K), low conductivity (~24 Ω^{-1}cm^{-1} at 300 K), and lesser surface to volume ratio because of the smooth morphology and consequent poor photocatalytic activity. The samples grew at higher N_2 flow rates (2.5 and 3.5 sccm) with the same In content also showed an enhanced photocurrent density than the reference sample, which was grown at 1.5 sccm. From Figure 4.9, we can also observe that, when compared to the sample grown at 3.5 sccm, the sample grown at 2.5 sccm showed a slightly higher photocurrent density. Even though the conductivity of sample grown at 2.5 sccm is less (~87 Ω^{-1}cm^{-1} at 300K) compared to samples grown at 1.5 (121.9 Ω^{-1}cm^{-1} at 300K) or

3.5 (242 $\Omega^{-1}cm^{-1}$ at 300K) sccm, because of the nanowall network structure, the electrode-electrolyte interaction is more and hence showed higher photocurrent density. With increasing N_2 flow rate from 1.5 to 2.5 sccm the nanowall network structure formed, which posseses on increased surface to volume ratio. Further, increase in N_2 flow rate, the voids of nanowall network structures are filled (ref. SEM Figure 4.2) and reduces the surface to volume ratio, and hence the semiconductor/electrolyte interaction decreases and consequently the photocurrent density. From this study, it is clear that the surface morphology of InGaN photoelectrodes significantly affects the photocurrent density, though they have the same In composition or better electrical properties.

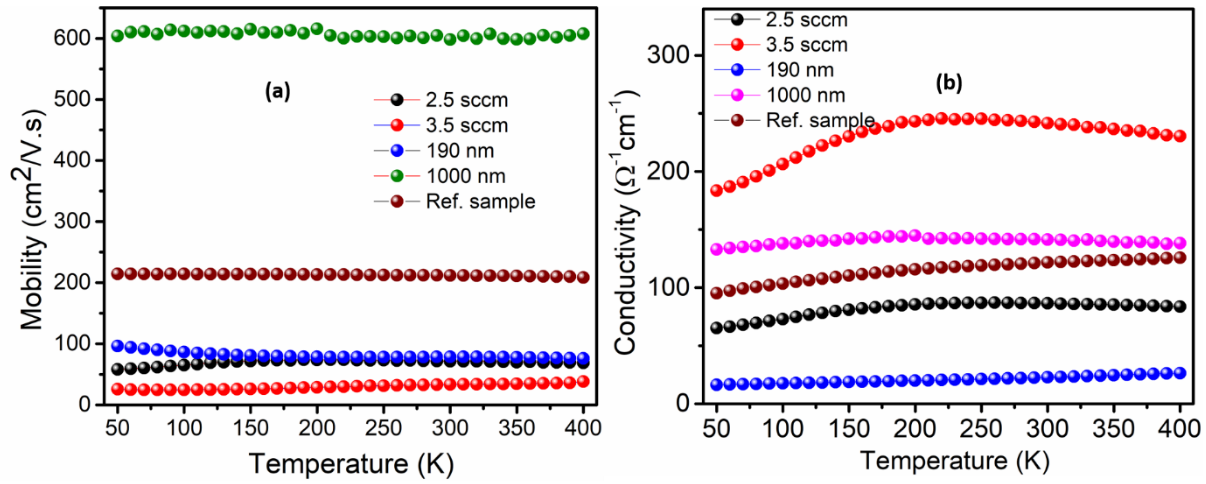

Figure 4.10 shows the variation in resistivity and mobility as a function of temperature for samples grown with different thicknesses and different N_2 flow rates

Also, from AFM surface roughness we compared how photocurrent densities vary with the roughness of the film and it is observed from Figure 4.11 that as the roughness of the samples increases the photocurrent densities also increased. Thus, surface morphology is playing a major role in these samples to get good photoelectrochemical performances.

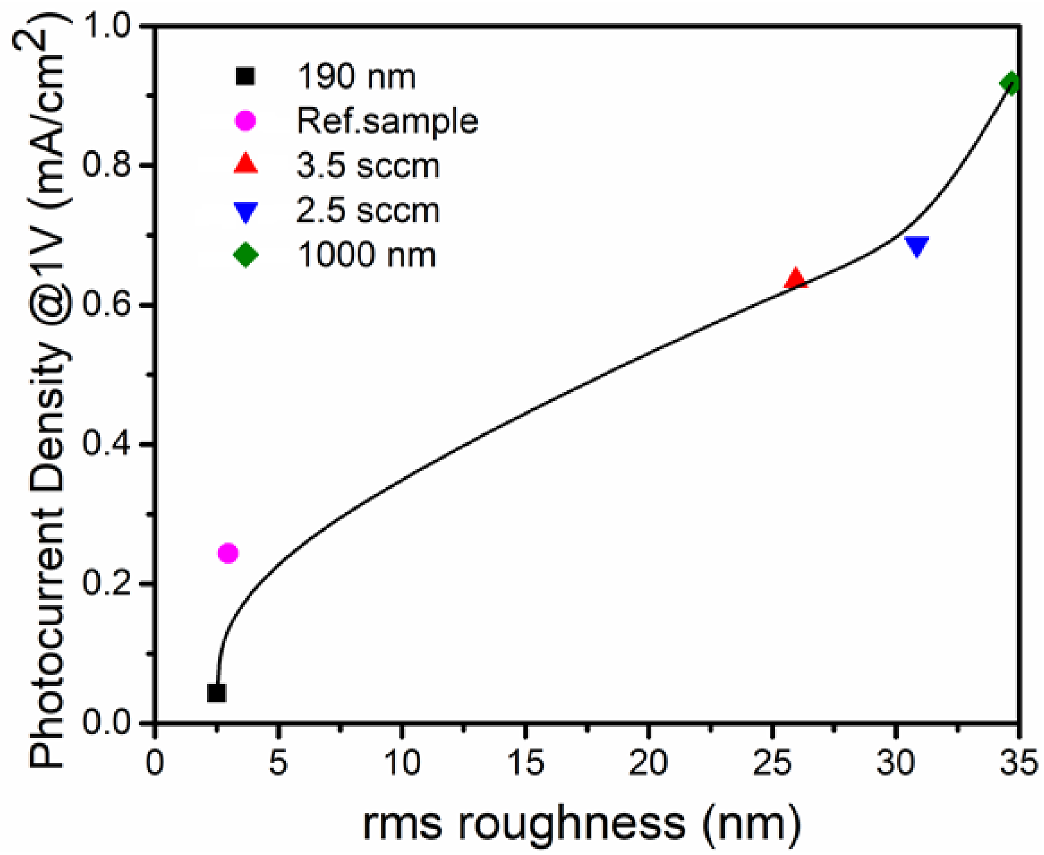

Figure 4.11 Plot of photocurrent density against the roughness of samples

Chronoamperometric experiments are carried out on all the samples to understand the photoresponse and to study the photo and electrolyte stability of InGaN electrodes. Figure 4.12a shows the transient photo responses at a potential of 0.8 V Vs SCE using a visible band filter for the InGaN photoelectrodes fabricated at different substrate temperatures and Figure 4.12b shows the same for the samples grown at different thicknesses and different N_2 flow rates along with the sample grown at 350 ^{o}C as a reference. All the samples showed a quick photo response upon illumination and the overshoot in photocurrent density in photoresponse related to efficiency of hole transport from photoelectrode to electrolcyte. The chronoamperometric stability results acquired at a potential of 0.8 V Vs SCE shown in Figure 4.12c indicates relatively good stability for all the samples for approximately over one hour.

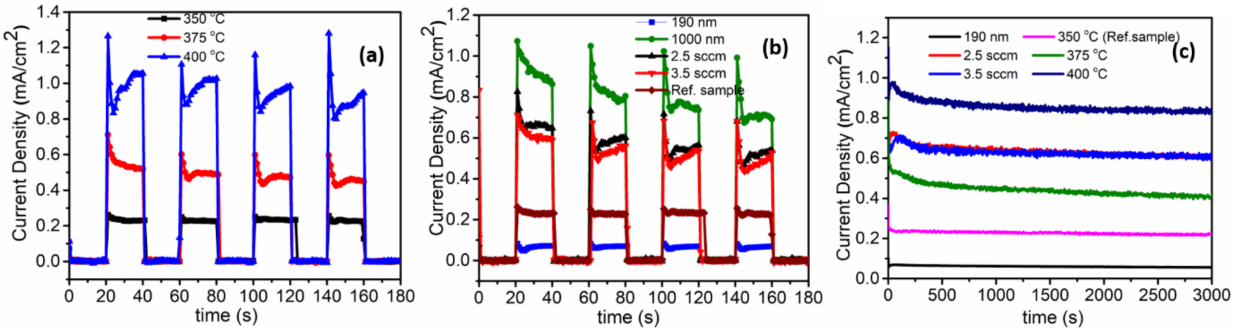

Figure 4.12 The transient photoresponse at a potential of 0.8 V Vs SCE using visible band filter for the InGaN photoelectrodes fabricated (a) at different substrate temperatures (b) at different thicknesses and N_2 flow rates along with the reference sample and (c) shows the stability of the electrodes for an hour approximately

4.1.4 Inferences

To understand the role of composition and surface properties on photoelectrochemical water splitting, we fabricated InGaN photoelectrodes with different In compositions and different morphologies by systematically changing the growth parameters. The In concentration in InGaN was controlled by varying the substrate temperature and different morphologies for samples with similar In composition were achieved by varying the film thickness and N_2 flow rates. The HRXRD showed the variation in In composition and the FESEM images confirmed the variation in surface morphology with different growth parameters. The optical absorption and emission studies showed that the fabricated thin-film structures have energy bands in the visible region. The samples grown at different substrate temperatures showed a systematic change in optical energy, whereas the samples grown at different N_2 flow rates and thicknesses showed a difference only in the morphology but not in the In composition. Our results show that the photoelectrochemical properties not only depended on the In incorporation but also on the surface morphology. Photoelectrochemical measurements showed a significant increase in the photocurrent density by changing the surface morphology. We have seen that the photocurrent density increases nearly 4 times from 0.25 to 0.90 mA/cm^2 at a potential of 1V vs SCE by varying the morphology, demonstrating that the surface to volume ratio plays an equally as significant role as the bandgap of the material, in determining the photoelectrochemical properties. The chronoamperometric analysis showed the electrodes are fast responsive to light and their stability is good under the experimental conditions.

4.2 Effect of Indium concentration on PEC properties of $In_xGa_{1-x}N$ photoelectrodes

4.2.1 Introduction

InGaN ternary alloys are interesting materials for photoelectrodes. Because of their band gap tunability, band edges that straddle the H_2 and O_2 redox potentials, higher carrier mobility, and chemical stability[19], By altering the In concentration, the band gap of InGaN may be adjusted from 0.7 eV (InN) to 3.4 eV (GaN), allowing absorption to be modulated from UV to IR [13]. Furthermore, the valence and conduction band edges of InGaN straddle both the hydrogen and oxygen evolution reaction potentials up to a 50% In content for better performance, implying that it can even induce direct unassisted water splitting [101]. InGaN has a high carrier transport and chemical stability due to its extremely crystalline structure and strong ionic bonding. Nanostructuring InGaN thin films while maintaining higher indium composition and preserving good quality of crystallinity improves light-matter interactions by increasing the semiconductor/electrolyte interface area while decreasing carrier transfer distance to the interface, hence improving photoelectrode PEC performance.

In this section, we have grown InGaN nanowall network and other structures using PAMBE, by varying the indium flux and measured their structural, optical and photoelectrochemical properties.

4.2.2 Experimental details

Table 4.3 below shows the growth parameters of the InGaN thin films grown on c-sapphire substrates by using PAMBE. Prior to growth, the substrates were cleaned chemically by acetone and isopropyl alcohol, and thermally degassed in the preparation chamber at 600 ^{o}C for an hour and at 800 ^{o}C in the growth chamber for 30 min. and then maintained growth temperature throughout film deposition.

Table 4.3 growth parameters of InGaN with different indium flux

Samples	Substrate Temp. (^oC)	Ga K cell temp. (^oC)	In K cell temp. (^oC)	N_2 flow (sccm)	Duration	N_2 Plasma power (W_f)
1 2 3	350	1000 ($4x10^{-7}$ torr -BEP)	800 820 840	1.5	3 hr (1000 nm)	300

All these grown samples are then probed using various complementary characterization techniques like FESEM, HRXRD, Optical absorption, Photoluminescence and Hall measurements.

4.2.3 Results and discussions

4.2.3.1 FESEM: Morphology and HRXRD

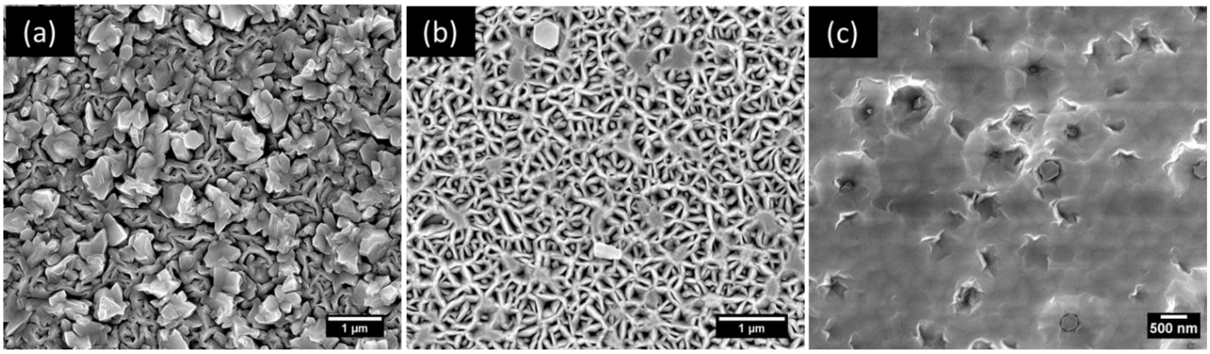

Figure 4.13 FESEM images of InGaN with varying k-cell temperature of Indium (a) 800 °C, (b) 820 °C and (c) 840 °C

We know that the morphologies of the thin films play a significant role in improving the performance of photoelectrochemical properties. The morphologies of grown thin film samples with different indium flux (In k-cell temperature) are shown the Figure 4.13 (a-c). The figures show that the morphologies are different with rough surfaces as we can see an underlying network like structure with nanorods in (a), Nanowall network (b) which we can see from chapter 4 the promises it can show in improving the performance and kind of filled nanowall network like structure in (c).

To study the structural properties and to determine the indium composition of the grown films, we carried out HRXRD measurement, The recorded 2θ-ω scans are shown in Figure 4.14. All three samples show wurtzite crystal structure and grown epitaxially with the substrate along the c direction of the substrate (i.e., InGaN (0002) || Sapphire (0006)). The shoulder peaks in the patterns belong to InGaN (0002) peak and the nature of these peaks shows the presence of phase separation in InGaN thin films. We deconvoluted these peaks into multiple peaks by peak fitting as shown in the inset of these figures, which correspond to different phases. By using Vegard's law, we calculated the composition of indium in each phase and calculated the average of the composition by considering areas under the peaks and the composition of each phase. The calculated average indium composition is found to be 9%, 21% and 31% for the k-cell temperatures (or Indium flux) of 800 °C, 820 °C and 840 °C, respectively. As expected, the indium incorporation in InGaN thin films was found to be increased with an increase in In flux.

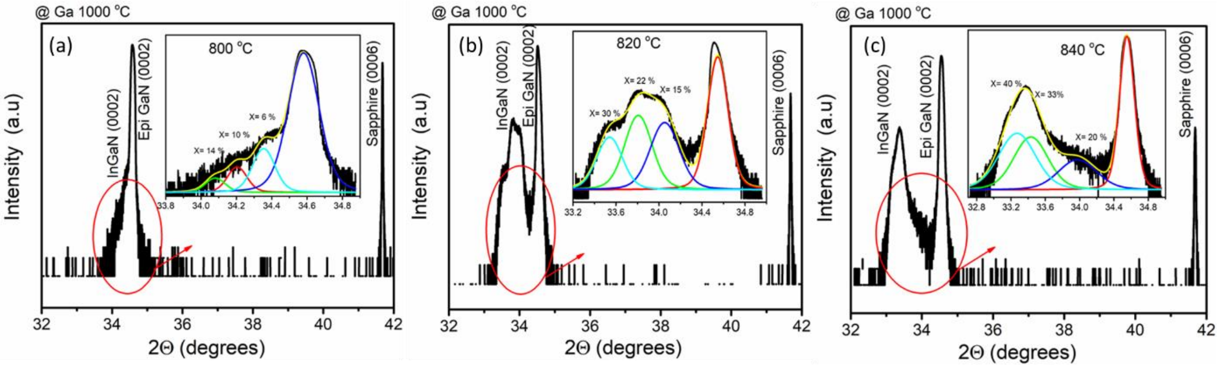

Figure 4.14 HRXRD patterns of InGaN thin films with varying k-cell temperature of Indium (a) 800 °C, (b) 820 °C and (c) 840 °C

4.2.3.2 Optical Properties

To determine the band gap and emission of the grown films we carried out UV-Visible absorption spectroscopy measurement and from the data, we plotted Tauc's plot. Figure 4.15 shows Tauc's plot for all the samples and we extrapolated the straight-line region of the plot to intersect the energy axis at 0 value $(\alpha E)^2$ to determine the energy gap. The obtained values are 2.69 eV, 2.55 eV and 2.39 eV for the samples grown with indium k-cell temperatures 800 °C, 820 °C and 840 °C, respectively. The energy gaps are reduced as we increase the indium flux due to more indium incorporation in the films.

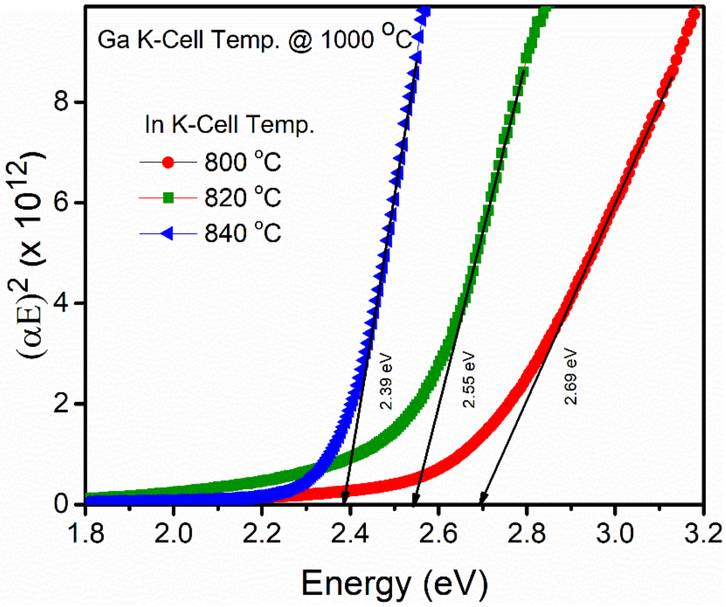

Figure 4.15 Tauc's plot of InGaN thin films with varying k-cell temperature of Indium

We also carried out the room temperature photoluminescence measurements to study the emission properties. Figure 4.16 shows the PL spectra of all the samples grown. We observed broad emissions from all the samples due to the presence of different phases which are evident from HRXRD patterns. The systematic shift in the maxima of emission is also observed. i.e., the sample with higher indium concentration emitted at lower energy region and that with lower indium concentration emitted at higher energy region.

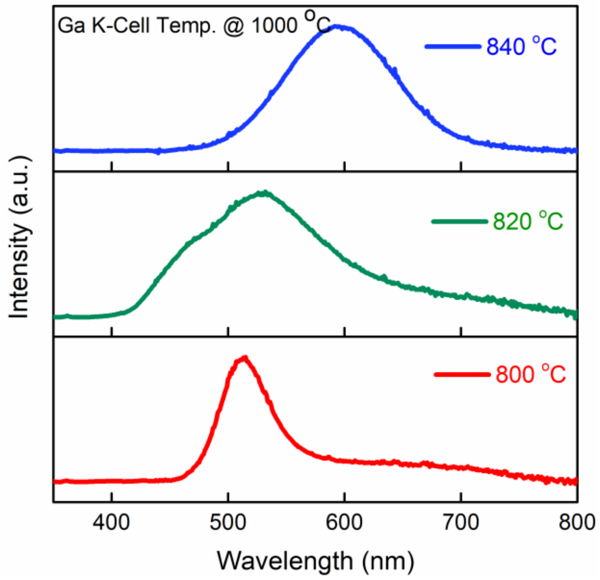

Figure 4.16 Photoluminescence spectra of InGaN thin films varying k-cell temperature of Indium

4.2.3.3 Hall Measurement

To study the electrical properties like carrier concentration and Hall mobility, we have carried out Hall measurements. Figure 4.17shows the extracted values from Hall measurements, carrier concentration vs mobility recorded at 300K. The carrier concentrations for all the samples are found to be almost of the same value ($\approx 10^{18}$ cm^{-3}), while the mobility of the samples increases as the indium incorporation is increased,

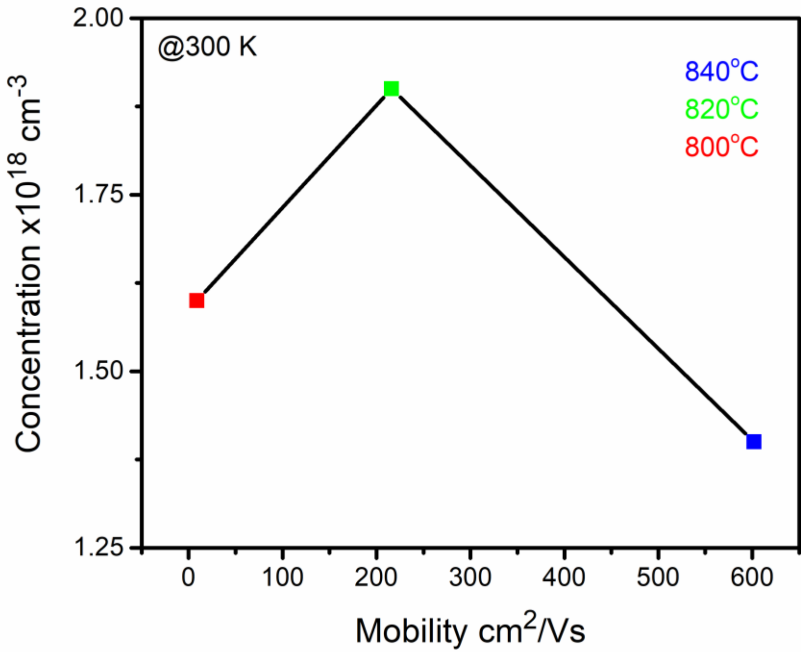

Figure 4.17 Carrier Concentration vs Mobility plot for InGaN thin films with varying k-cell temperature of Indium

4.2.3.4 Photoelectrochemical properties

We have studied properties like morphology, decrease in the band gap to increase the absorption and straddle with the redox potential of water. So, it will be interesting to investigate photoelectrochemical properties. In this view, we fabricated the device by giving ohmic contacts and covered it with epoxy and Teflon tape, to carry out the photocurrent measurement in an electrolyte of 1M Na_2SO_4. Figure 4.18a shows the measured photocurrent density vs applied potential (vs SCE), for all the photoelectrodes. The photoelectrodes show negligible dark photocurrent density and under the illumination of light passing through a visible pass filter, the photoelectrode with the highest indium concentration shows better performance compared to the other two. We can observe that samples with Indium k-cell temperatures of 840 ^{o}C and 820 ^{o}C do not show much difference in performance although there is a significant change in indium concentration in them. So, the sample with indium k-cell temperature of 820 ^{o}C shows better performance due to the morphology of the sample also playing an important role. Overall, the photoelectrode with the highest indium concentration shows superior performance with better photocurrent density and onset potential.

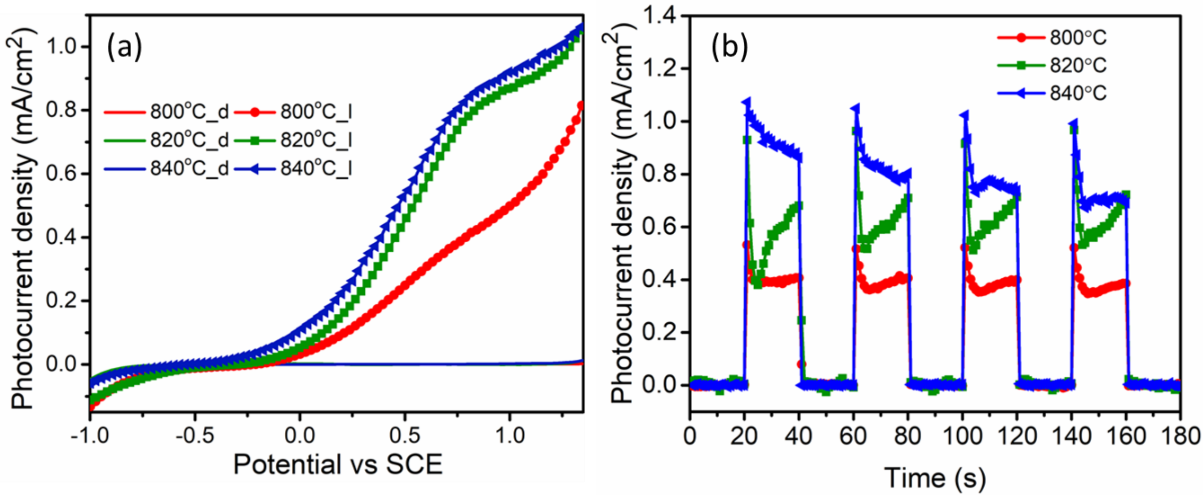

Figure 4.18 (a) The variation in photocurrent density (under dark and illumination using visible band filter) as a function of potential for InGaN photoelectrodes with different k-cell temperature of Indium. (b) The transient photoresponse at a potential of 0.8 V Vs SCE using visible band filter for the InGaN photoelectrodes.

Chronoamperometric experiments are carried out on all the samples to understand the photoresponse, 0.8 V vs SCE bias was applied during experiments. Figure 4.18b shows, all the samples are having quick photoresponse with an overshoot in photocurrent density, which is ascribed to a complicated carrier transportation process, mainly related to hole transfer efficiency from photoelectrode to electrolyte[196]. In the present case, the overshoot may be due to poor hole transfer efficiency.

4.2.4 Inferences

We have grown InGaN with different indium concentration by varying indium flux (or k-cell temperature) and to understand its photoelectrochemical properties, we have fabricated InGaN photoelectrodes. The samples' morphology and indium incorporation, changing the band gap, helped in observing good photocurrent densities. Among these samples, the sample with the highest indium concentration showed excellent performance in both photocurrent density and onset potential, compared to the other two samples.

4.3 PEC properties of InGaN with different electrolytes

4.3.1 Introduction

The hydrogen evolution reaction (HER) and the oxygen evolution reaction (OER) are the two half-reactions that make up the complete water splitting reaction. It is well known that the extreme pH of severely acidic or alkaline situations can increase efficiency. As a result, at extreme pH levels, majority of the basic understanding of water splitting has been established. As the conductivity of pure water is too low for an efficient PEC water splitting, choosing the electrolyte is very important. In the literature, different electrolytes with different concentrations were used to minimize the resistivity in the cell and to enhance the photoelectrochemical reaction.[197,198] Here in this work, we tried to understand the effects of different electrolytes on the PEC properties of InGaN photoelectrodes. We chose acid, base, and neutral conditions and carried out the measurements.

4.3.2 Experimental details

InGaN thin films are grown on c-sapphire substrates, by varying gallium k-cell temperature (or Ga flux) and keeping other parameters constants, by using PAMBE. Prior to deposition, all the substrates were cleaned chemically with acetone and isopropyl alcohol, and thermally degassed in the Preparation Chamber at 600 °C for an hour and at 800 °C in the growth chamber for 30 min., and then maintained growth temperature throughout film deposition. The growth parameters are tabulated in Table 4.4.

Table 4.4 Growth parameters of InGaN with different Gallium flux

Samples	Substrate Temp. (°C)	Ga K cell temp. (°C)	In K cell temp. (°C)	N_2 flow (sccm)	Duration	N_2 Plasma power (W_f)
1	350	940	800	1.5	3 hr (1000 nm)	300
2		970				
3		1000				

After the deposition, all the samples are then investigated for their properties by using various complementary characterization techniques like FESEM, HRXRD and Optical Absorption.

4.3.3 Results and Discussions

4.3.3.1 FESEM, HRXRD and Tauc's plot

We have seen in previous sections how the morphologies of thin films play a significant role in improving the performance of photoelectrochemical properties. The morphologies of grown samples with different Gallium flux (Ga k-cell temperature) are shown the Figure 4.19. The figures show that the morphologies are porous-like structures and randomly spread nanorods in cavities across the surface.

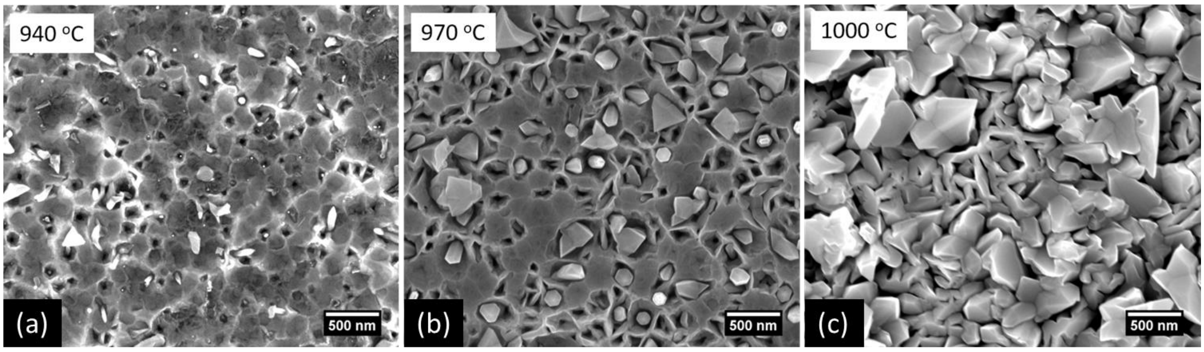

Figure 4.19 FESEM images of InGaN with varying k-cell temperature of Gallium (a) 940 °C, (b) 9700 °C and (c) 1000 °C

The HRXRD patterns are carried out to determine the structural properties and to calculate the indium incorporation by using Vegard's law. Figure 4.20a shows the 2θ-ω scans for all three samples and confirms the wurtzite crystal structure and epitaxial nature with the sapphire substrate. The broader nature of InGaN (0002) peak shows the co-existence of multiple phases. We have deconvoluted these peaks by fitting as shown in Figure 4.20b and calculated the composition of each phase and the values are shown in the same figure. The average indium concentrations calculated are 24%, 11% and 8% for the samples grown with Ga k-cell temperatures of 940 °C, 970 °C, and 1000 °C respectively.

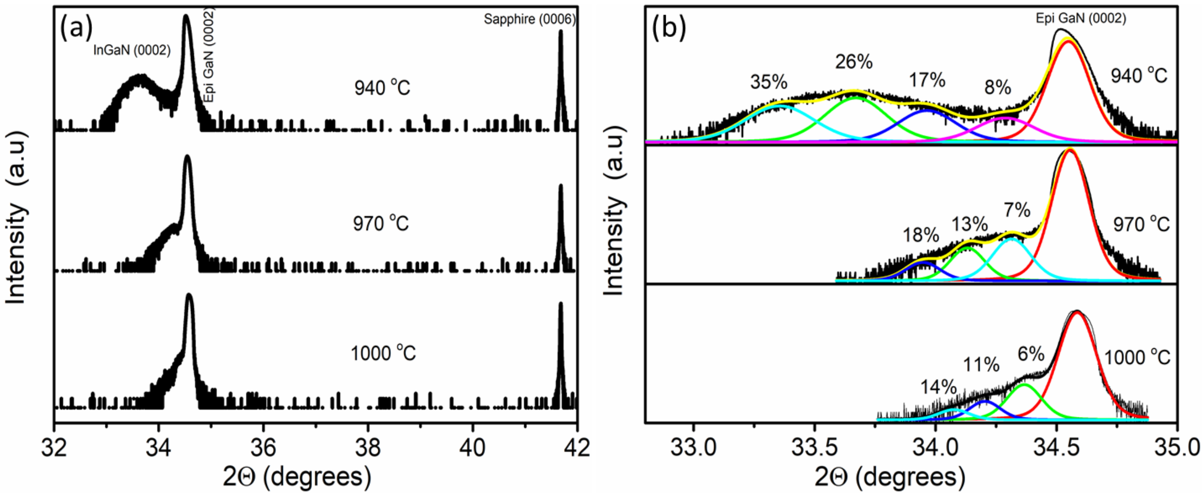

Figure 4.20 HRXRD patterns of InGaN thin films with varying k-cell temperature of Gallium (a) 2θ-ω scan, (b) Fitted InGaN (0002) peak

The energy gaps of these samples are determined by Tauc's plot as shown in Figure 4.21, plotted by using absorption spectroscopy data. Obtained energy gap values are 2.29 eV, 2.55 eV and 2.67 eV for the samples grown with Ga k-cell temperatures 940 °C, 970 °C and 1000 °C respectively. As we increase the gallium flux the indium concentration decreased and the energy gap increased as expected.

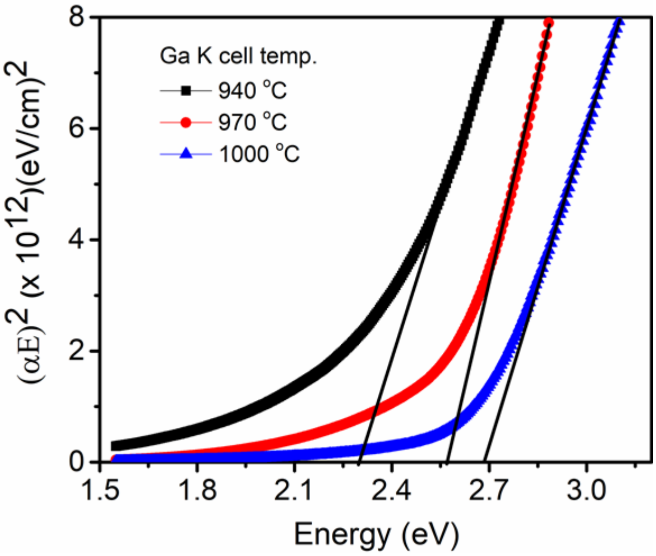

Figure 4.21 Tauc's plot of InGaN thin films with varying k-cell temperature of Gallium

4.3.3.2 Photoelectrochemical Properties

To understand the PEC properties, we fabricated the devices (photoelectrodes) by making ohmic contacts and covered the contact region with insulating epoxy and Teflon tape. We then used these photoelectrodes as working electrodes to measure the photocurrent densities under a visible pass filter, in three different electrolytes of 1M, namely, Na_2SO_4, HCl and NaOH. Figure 4.22 shows photocurrent densities measured by sweeping the potential with reference to SCE, in different electrolytes. All the photoelectrodes show negligible dark current, and the photocurrent at 1V is observed to increase with Na_2SO_4, HCl and NaOH electrolytes, due to an increase in the conductivity of water. It is observed that the onset potentials are cathodic shifted in HCl compared to Na_2SO_4 and shift further in case of NaOH electrolyte. We can see it clearly in Figure 4.23b, the respective shifts of the onset potentials. In case of NaOH, the shift can be attributed to a lower standard electrode potential of +0.4 V for oxidation of OH^-, in comparison to that of +1.23 V for H_2O[199–201]. Hence hydroxide oxidation is more favorable in NaOH and shifts the onset potential. The photocurrent also is more in NaOH compared to the other two, which may be because of the onset etching process at the surface[201]. The etching removes surface recombination centers which help in the efficient separation of charge carriers and increases the photocurrent. Also, the photocurrent density in the HCl case is raised abruptly compared to that of Na_2SO_4, due to more surface recombination of charges taking place in Na_2SO_4.[202]

Chronoamperometric experiments to study transient photoresponse are carried out on all the photoelectrodes, at 0.8V vs SCE. Figure 4.23b shows the transient photoresponse carried out by chopping (ON/OFF) the light every 20 seconds, all the samples show a fast response. In case of Na_2SO_4, an overshoot in photocurrent is observed but not in case of HCl and NaOH, which may be attributed to the better hole transfer efficiency from the electrode to the electrolyte, compared to that in Na_2SO_4.

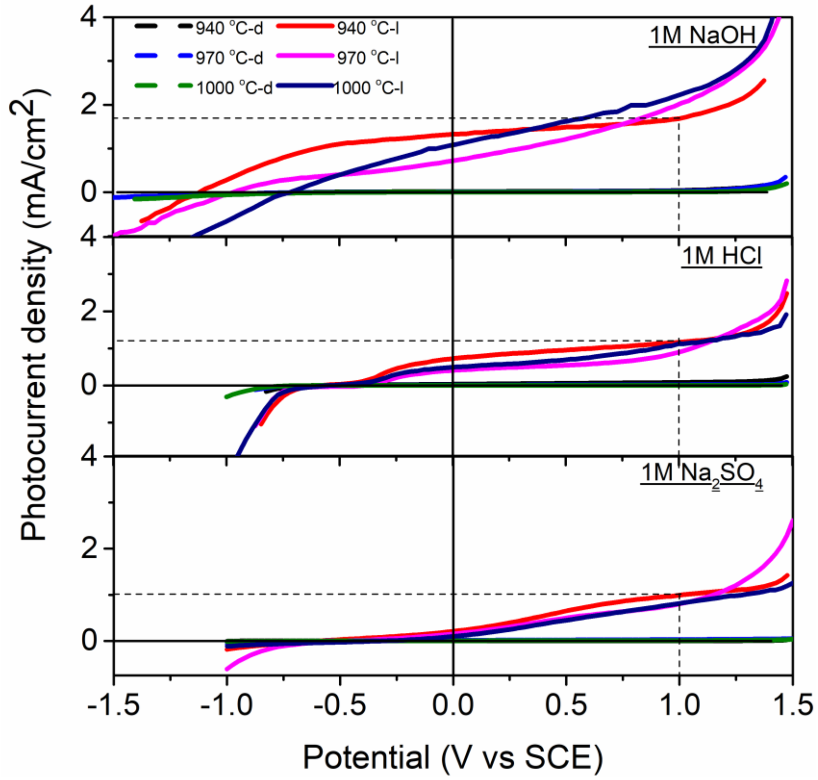

Figure 4.22 The variation in photocurrent density (under dark and illumination using visible band filter) as a function of potential for InGaN photoelectrodes with different k-cell temperature of gallium, in Na_2SO_4, HCl and NaOH electrolytes.

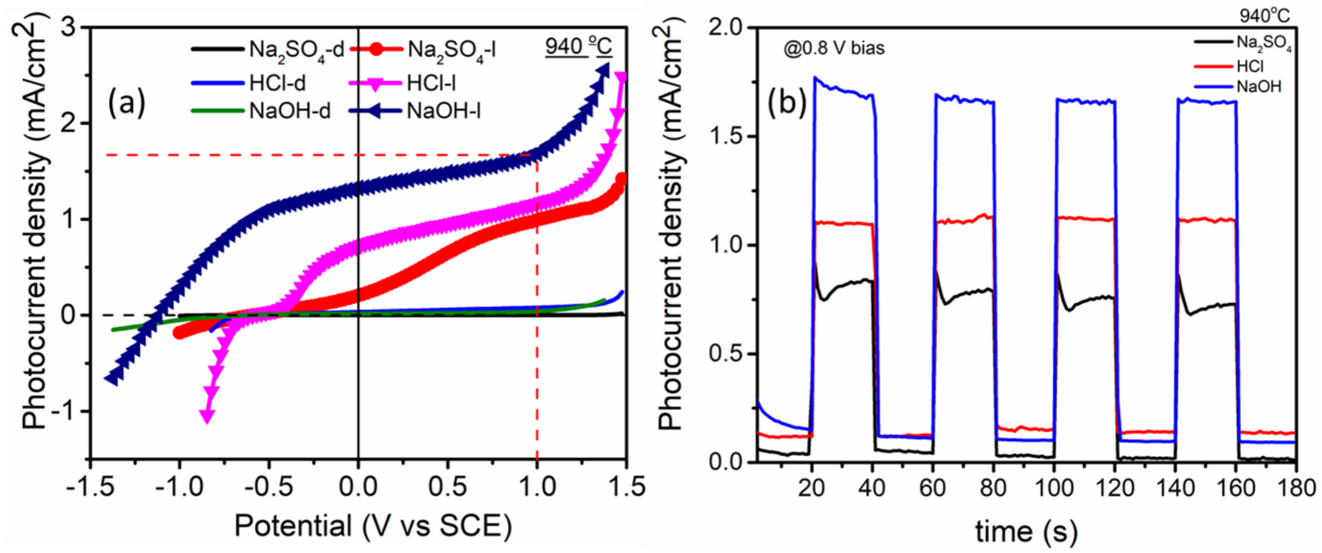

Figure 4.23(a) Photocurrent density vs potential (vs SCE) for the photoelectrode which is grown with Ga k-cell temperature at 940^{o}C, in Na_2SO_4, HCl and NaOH electrolytes. (b) The transient photoresponse at a potential of 0.8 V Vs SCE using visible band filter for the InGaN photoelectrodes.

4.3.3.3 FESEM and XRD after PEC measurements

After carrying out PEC measurements carried out in NaOH, the samples are found to be damaged at the surface. To understand this, we carried out FESEM to re-look at the morphology and XRD to observe the changes in the structure of the electrodes. Figure 4.23 a-c shows that the samples are etched out during experiments as shown in Figure 4.19. The insets in FESEM images show a magnified region of the surface. The corrosive etching of the sample observed by XRD patterns shows significant structural change in InGaN (0002) peaks as compared to those before the PEC measurements, as can be seen in Figure 4.23 d-f.

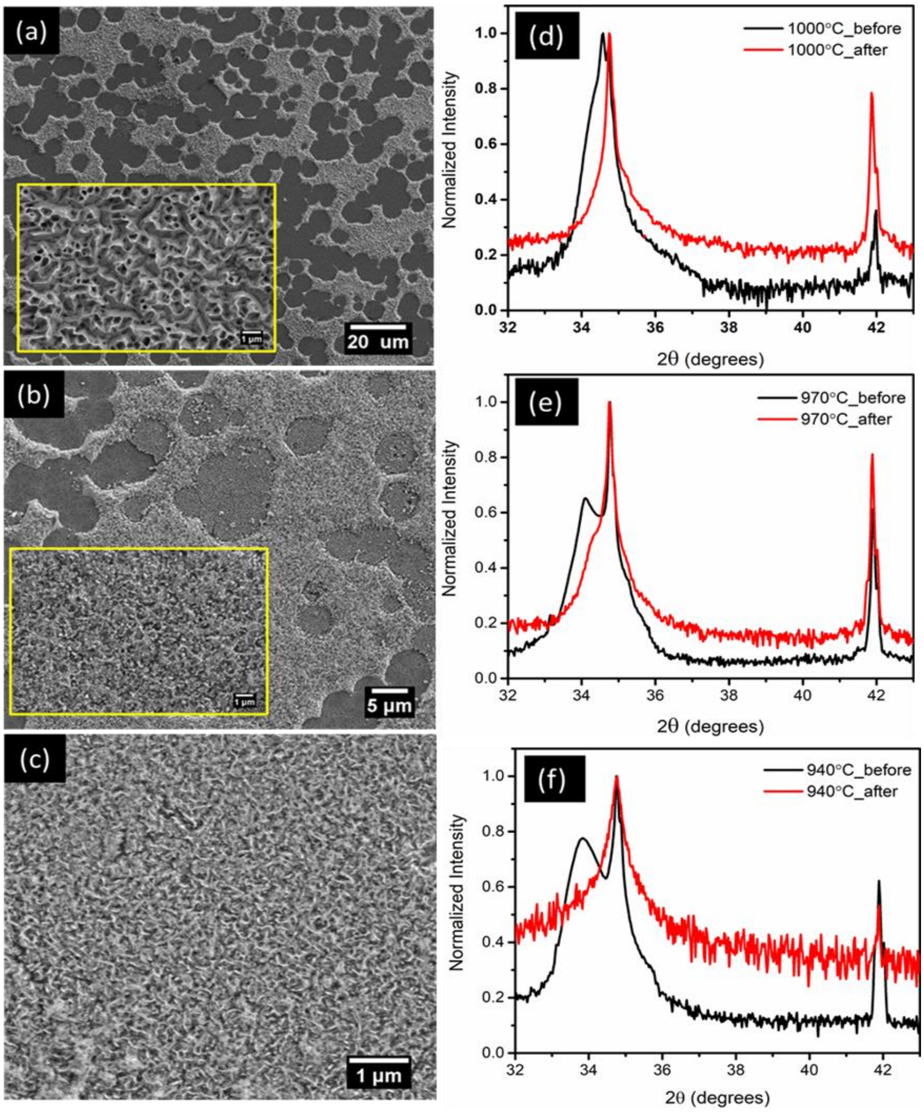

Figure 4.24 (a-c) FESEM images after, and (d-f) XRD patterns before and after PEC measurements for the samples grown by varying gallium k-cell temperature 1000 ^{o}C, 970 ^{o}C and 940 ^{o}C respectively.

4.3.3.4 Inferences

We have deposited InGaN by varying gallium k-cell temperature (Ga flux) and studied the effects of different electrolytes such as Na_2SO_4, HCl and NaOH on these electrodes. We have observed an onset shift in photocurrent density with NaOH showing the highest shift due to favorable potential of oxidation of OH^-(+0.4 V) compared to oxidation of water (+1.23 V). Samples are also found to be etched out after the PEC measurements, the FESEM images and XRD patterns before and after show both morphology and structural change.

Chapter 5

$In_xGa_{1-x}N$ thin films grown on n^+ Si (111)

This chapter discusses the photoelectrochemical properties of InGaN grown on conducting Si (111) substrate. The effect of the interface on the properties is discussed. The chapter allows how TiN as an interface layer helps in avoiding interfacial resistance caused by SiN_x *formed during growth.*

5.1 PEC properties of InGaN thin films grown on Si (111)

5.1.1 Introduction

InGaN grown on different substrates like sapphire and epi GaN are used as photoelectrodes for water splitting applications discussed in the previous chapters. Even though there are many reports on the photoelectrolysis of InGaN-based systems, reaching commercial by viable application is hindered due to the low solar to hydrogen conversion efficiency. This may be partially due to the lack of a highly conductive substrate, which plays a crucial role in the transport of photogenerated holes and electrons to the respective electrodes. The high resistivity of the most commonly used substrates such as sapphire and SiC, to grow III-nitrides prevents the direct electrical contact of overgrown devices with electrical components. Therefore, Si (111) is being investigated as an alternative substrate for InGaN growth due to its excellent doping properties, high abundance and excellent crystal quality that helps InGaN to grow epitaxially. Also, its low cost, availability of large-sized wafers, good thermal conductivity, ease of cleavability and possible integration of III-nitrides with the mature silicon technology[203] have attracted technologists and researchers. The lattice parameter mismatch between Si and III-nitrides promotes the formation of low defect nanostructures. These nanostructures grown on conducting Si (111) substrate will have an advantage as Si can act as a back contact for electrical measurement, and due to their large surface to volume ratio, can play a significant role in photoelectrochemical water splitting. During InGaN growth on Si by PAMBE, the Si substrate might be exposed to nitrogen plasma which results in the formation of a thin SiN_x insulating layer at the interface of InGaN and Si. This will increase the interfacial resistance and resist charge transport during water splitting. In order to avoid this, we have grown a titanium nitride (TiN) layer on the Si surface before InGaN deposition. The growth of InGaN nanowires on Ti metal layer by MBE is reported by Ebaid et.el.[204] have shown an enhancement in charge carrier transport and an improved STH with the introduction of Ti metal layer. However, since TiN has ≈6% of lattice mismatch[205] with GaN, it enables the formation of epitaxial films. In addition, this TiN interface layer provides low contact resistance which can be used to make back contact to the photoelectrodes[206]. It also has a suitable work function (4.25 eV) for electric contact to InGaN, which helps to improve the electron-hole charge separation.

In this chapter, we report our studies of grown InGaN thin films with different morphologies such as nanorods and nanowall network, on a highly doped conducting Si (111) substrate with and without TiN layer. Electrical back contact to the substrate is used for photocurrent density measurements to study the PEC properties.

5.1.2 Experimental details for InGaN/Si

InGaN thin films are grown by using PAMBE on conductive Si (111) substrates (ρ = 0.001-0.005 ohm-cm), where the growth parameters used are given in Table 5.1. Prior to the growth, Si substrates were chemically cleaned employing standard RCA1 technique procedures developed by Werner Kern at Radio Corporation of America (RCA) to remove organic residues from the silicon wafers and RCA2 to remove metal ion impurities from the surface[207]. Further, the substrates were thermally cleaned (degassed) at 600 °C for 1 hour in the

Table 5.1 Growth parameters of InGaN thin films grown on Si (111) substrate

Samples	Substrate Temp. (°C)	Ga K cell temp. (°C)	In K cell temp. (°C)	N_2 flow (sccm)
S1	350	1000	800	1.5
S2	350	1000	840	1.5
S3	350	980	800	1.5
S4	350	980	840	1.5

preparation chamber of the MBE system and at 800 ^{o}C for 30 minutes in the growth chamber to observe the typical 7x7 RHEED pattern reflecting the atomically and structurally clean surface. The growth temperature is maintained throughout the deposition for an hour while it is exposed to N_2^+ plasma, of power of 300 W. After the deposition the films were characterized by using different techniques such as FESEM, XRD and the photoelectrochemical properties of all the photoelectrodes studied in a PEC cell.

5.1.3 Results and Discussion

5.1.3.1 FESEM and XRD

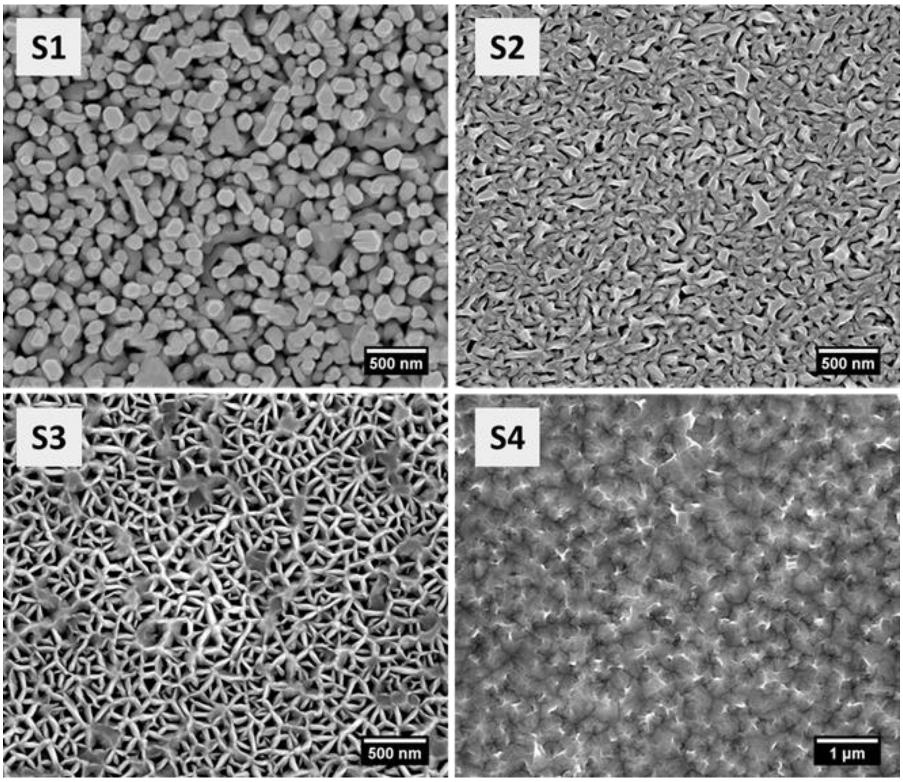

Figure 5.1 FESEM images of InGaN grown on Si (111) substrates as per the growth parameters given in the Table 5.1.

We have seen from the previous chapters that the kinetics of growth which are controlled by the growth parameters strongly affect both the surface morphology and the indium composition of the grown InGaN films. In order to see how the growth parameters, affect the morphology of InGaN films grown on Si substrate, we have carried out FESEM imaging. Figure 5.1 shows the top view of FESEM images of all four samples with four different morphologies. The mentioned growth parameters are given in Table 5.1. It can be noticed from the scale bars in the figures that the various features observed are about 100 nm in the size, except in the last figure where the features observed about 200 nm in size. The morphologies of the sample S1 showed nanorods structures, S2 showed tetrahedral-like structures, S3 showed the nanowall network formation and S4 showed tapered pyramidal structures. In this study, we focus on how surface morphology affects PEC properties.

XRD technique is used to study the structural properties and to determine the indium concentration of these four samples with different morphologies. It confirmed that InGaN films are formed in the wurtzite crystal structure. The left panel of the XRD patterns given in Figure 5.2 shows that InGaN grows with the c-axis and grows along with the Si (111) direction in all the samples. On the right side, InGaN (0002) peaks are deconvoluted into gaussian components and are used to determine the indium concentration by using Vegard's law. The deconvolution reveals that the peak at $2\theta \approx 33^o$, keeps increasing for the samples S1 to S4. The enhancement of this peak reflects the increase of the indium incorporation in the respective samples to form $In_xGa_{1-x}N$ of different x values. Calculated values of indium concentration are 7%, 17%, 21% and 30% for the samples S1, S2, S3 and S4, respectively. From samples S1 to S2, the increase in indium composition is attributed to indium k-cell temperature. From S1 to S3 the increase in indium composition is due to the decrease in gallium k-cell temperature. For samples S1 to S4 the increase in indium composition is due to both decrease in gallium k-cell temperature and also the increase in indium k-cell temperature. The effect of indium and gallium k-cell temperatures on indium composition for samples grown on Si showed the same trend as that were grown on epi GaN substrates which were described in the previous chapters.

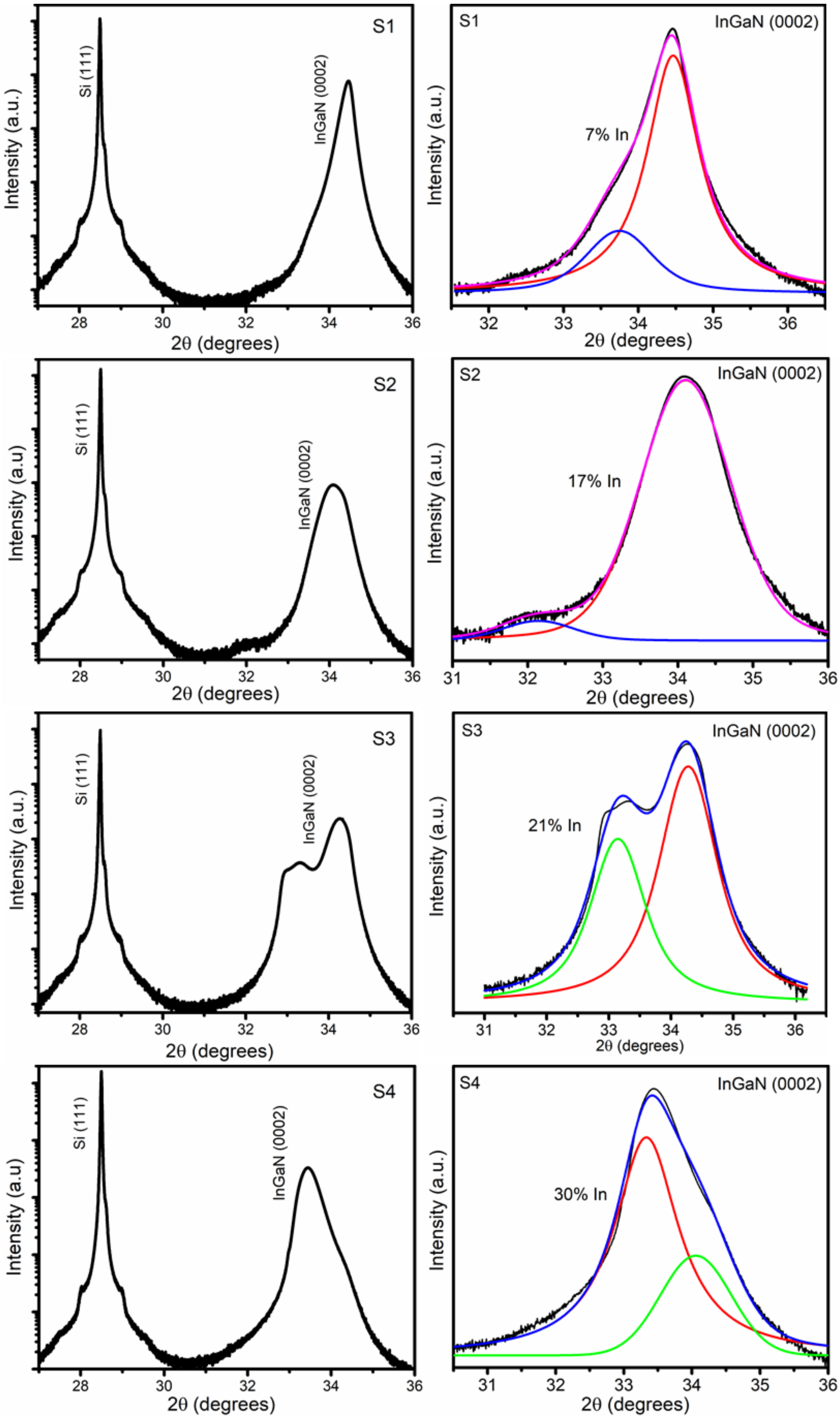

Figure 5.2 XRD patterns of InGaN on Si (left side) and Deconvoluted InGaN (0002) peaks (right side)

5.1.3.2 PEC properties

The effect of surface morphology and indium composition on the photoelectrochemical water splitting studies are carried out by fabricating InGaN/Si photoelectrodes on all the samples by making aluminium ohmic contact on silicon. The PEC measurements were carried out in 1M HCl electrolyte. In order to protect the metal contact from corrosion due to the electrolyte, we covered the contact area with an insulated epoxy and wrapped it with Teflon to avoid its exposure to the acidic electrolyte. Photocurrent densities were measured under a visible band pass filter and Xe lamp power of 180 W. Figure 5.3 shows the photocurrent densities recorded by sweeping voltages against SCE. The insets in the plots are included to relate the PEC properties with various morphologies of corresponding photoelectrodes. The dark current in all the samples are observed to be negligible. The photocurrent density in case

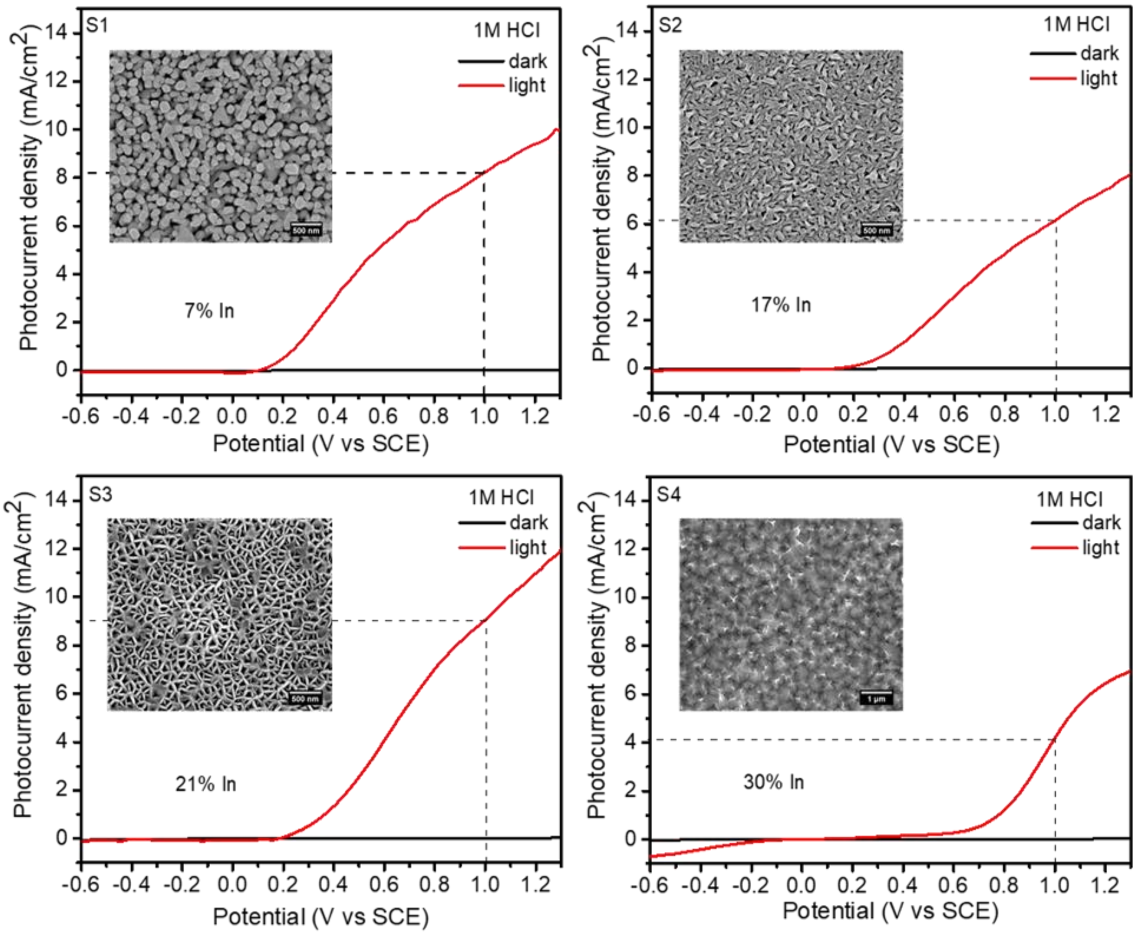

Figure 5.3 Variation in photocurrent density as a function of potential (vs SCE) for InGaN photoelectrodes grown on Si (111), insets shown are morphologies of corresponding photoelectrodes.

of nanorods (S1) is high, despite low indium concentration. This may be due to large surface area caused by the 100nm-sized nanorods which are in contact with the electrolyte[92,181]. Sample S3, which comprises of the nanowall network structure with more indium composition (21%) compared to that of S1 (7%) showed the highest photocurrent density among the four samples fabricated, suggesting that this might be due to the nanowall network morphology[164,192]. Even though the samples S2 (17%) and S4 (30%) have higher indium composition compared to sample S1, we observe that S1 shows a better photocurrent density, which can be attributed to the increased surface area of nanorods that can interact with the electrolyte. As compared to the InGaN thin films grown on c-sapphire or epi GaN substrates, the samples grown on silicon showed a positive shift (anodic shift) in the onset potential. This shift might be attributed to the presence of an unintentionally formed SiN_x interface layer during the growth of InGaN thin films on silicon[194] in which bare Si (111) was exposed to the nitrogen plasma. We studied and discussed more on this in the next section 5.2.

We carried out chronoamperometric experiments to check the photo and chemical stabilities of fabricated InGaN/Si photoelectrodes. Figure 5.4 shows the variation in the photocurrent densities as a function of time at a fixed bias voltage of 1.2 V for samples S1 and S2 in different electrolyte (1M HCl and 1M Na_2SO_4) solutions, respectively. The experiments were carried out for about an hour for samples S1 and S2 in each electrolyte. Both the electrodes showed chemically stable photocurrent densities with time in Na_2SO_4 electrolyte. However, the photocurrent densities reduce gradually with time in HCl electrolyte, which indicates that the photoelectrodes are not stable enough over longer durations.

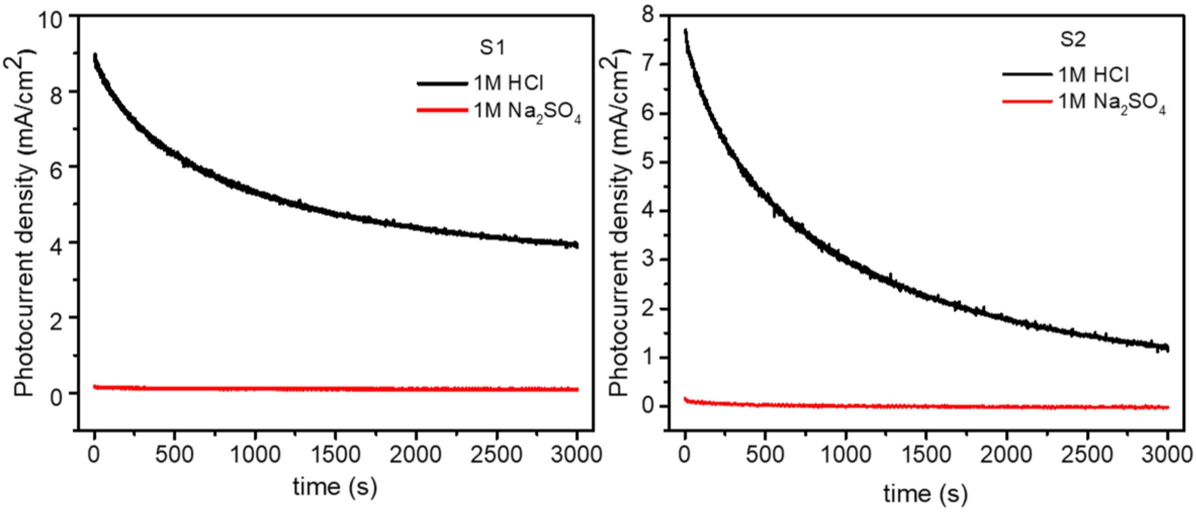

Figure 5.4 Photocurrent versus time showing stabilities of InGaN/Si photoelectrodes at a bias of 1.2V, in 1M HCl and 1M Na_2SO_4 electrolyte.

In order to see the effect of the electrolyte on the morphology of the photoelectrodes, we performed, FESEM studies after the PEC measurements. Figure 5.5 shows the FESEM images for all the samples S1, S2, S3 and S4 before and after the PEC measurements. Corrosive etching of the InGaN surfaces is observed in all the samples, which may be enhanced due to photo corrosion caused by UV light and applied voltages[208,209]. The figure shows that though the samples S1 and S4 have changed their morphologies after the PEC measurements, while S2 and S3 are relatively more stable.

.

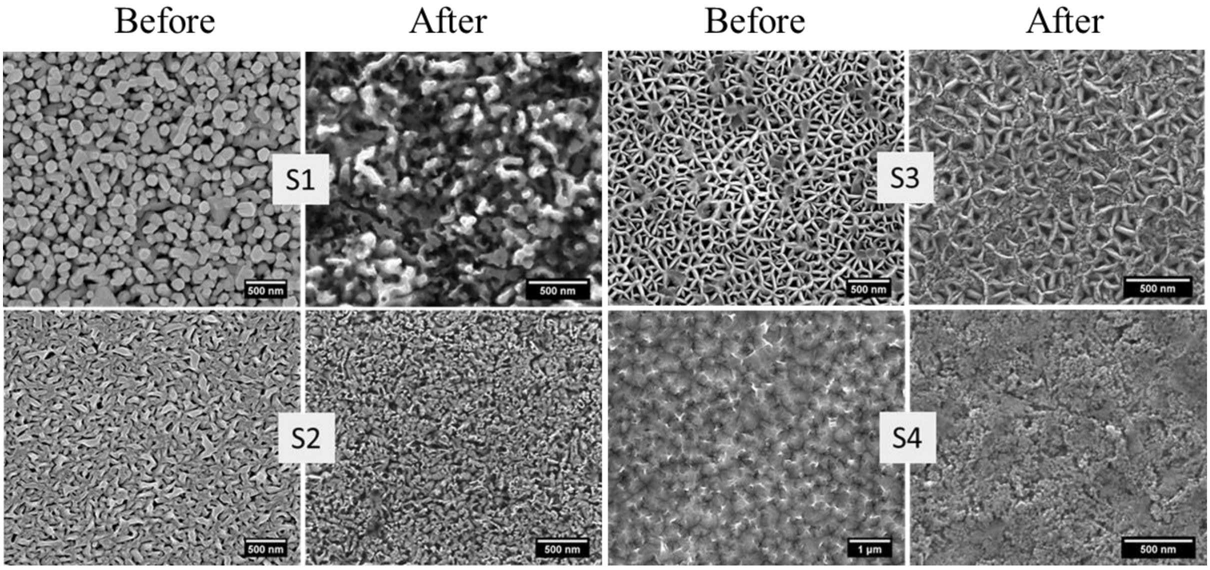

Figure 5.5 FESEM images of the samples S1, S2, S3 and S4, before and after the PEC measurements

5.1.4 Inferences

Thus, in this study, we have reported the PEC properties of InGaN grown on Si (111) substrates and from FESEM images we observed different morphologies of nanostructures. Significant photocurrent densities are observed in these samples compared to InGaN grown on c-sapphire substrates, as discussed in the previous chapter. Stability studies show that these photoelectrodes with some morphologies are more stable than others for a longer duration in HCl due to etching, as revealed in the FESEM images obtained after the PEC measurements.

5.2 Effect of TiN interfacial layer on PEC properties

In the previous section, we observed that the onset potential of InGaN grown on Si substrates gets shifted towards a positive potential (anodic shift) when compared to InGaN grown on c-sapphire substrates, which was discussed in the previous chapters. Since we speculate that this difference might be due to the formation of an insulating silicon nitride layer (SiN_x) at the interface[194], during the brief exposure of Si (111) surface to nitrogen plasma, just before the InGaN growth initiates. In order to understand this, we have grown an intermediate titanium nitride (TiN) layer on the Si surface before InGaN deposition. The effect of this TiN layer on PEC properties are discussed in this section.

5.2.1 Experimental Details for InGaN/TiN/Si

We followed the same procedure mentioned in section 5.1.2 to clean the Si substrate, before being loaded into the growth chamber to deposit TiN using PAMBE. The substrate temperature is maintained at 600 °C and titanium is evaporated using k-cell temperature at 1530 °C and the nitrogen flow rate of 1.2 sccm and nitrogen plasma power of 350 W for a duration of 2 hours, to deposit TiN on Si (111). Later, we loaded Si and TiN/Si substrates to deposit InGaN for one hour and the growth parameters are shown in Table 5.2. InGaN deposition on both substrates is carried out simultaneously to minimize the variations in the growth parameters. The schematic diagram of samples is shown in Figure 5.6, where SiN_x is unintentionally formed in both the samples during growth, while the TiN layer is deposited in S2.

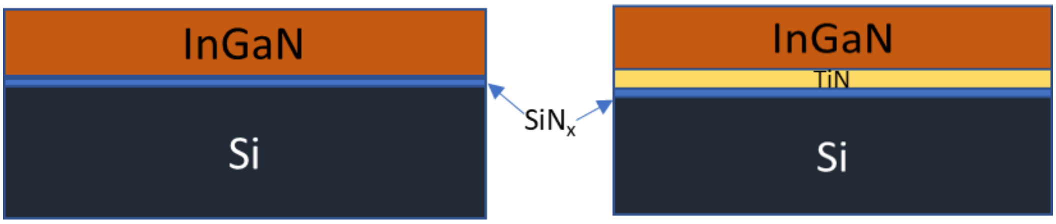

Figure 5.6 Schematic representation of InGaN grown on Si and TiN/Si substrates

Table 5.2 Growth parameters for InGaN grown on Si and TiN

Sample	Substrate Temp. (°C)	Ga K cell temp. (°C)	In K cell temp. (°C)	N_2 flow (sccm)	Duration	N_2 Plasma power (W_f)
InGaN/Si	375	950 ($1.3x10^{-7}$ torr -BEP)	820 ($2.1x10^{-7}$ torr -BEP)	1.5	1hr	300
InGaN/TiN/Si						

After the deposition, we characterized the samples with different characterization techniques. FESEM, XRD, Capacitance-Voltage (CV) and PEC measurements are carried out in 1M HCl electrolyte to study the PEC and chronoamperometric properties for stability measurements.

5.2.2 Results and discussions

5.2.2.1 FESEM and XRD

To examine the morphologies of the grown samples we have carried out FESEM imaging and the recorded images are shown in Figure 5.7. The top view of the grown samples (Figure 5.7 a & c) reveals that nanorods are formed in both cases with no significant difference in morphology except for the different densities of nanorods. InGaN nanorods grown on Si (Figure 5.7a) are slightly denser than that of grown on TiN/Si (Figure 5.7c). Also, Figure 5.7 (b) and (d) are the cross-section FESEM images of InGaN grown on TiN/Si and Si, respectively. In Figure 5.7b, we can clearly see the presence of the interface layer of TiN (≈60 nm). The thickness of InGaN grown on Si is ~650 nm while that grown on TiN/Si is ~200 nm. This difference in the InGaN thickness with identical growth conditions suggests that the sticking coefficient of InGaN on TiN is low than on a bare silicon surface, which results in a slower growth rate, as compared to that of on Si substrate.

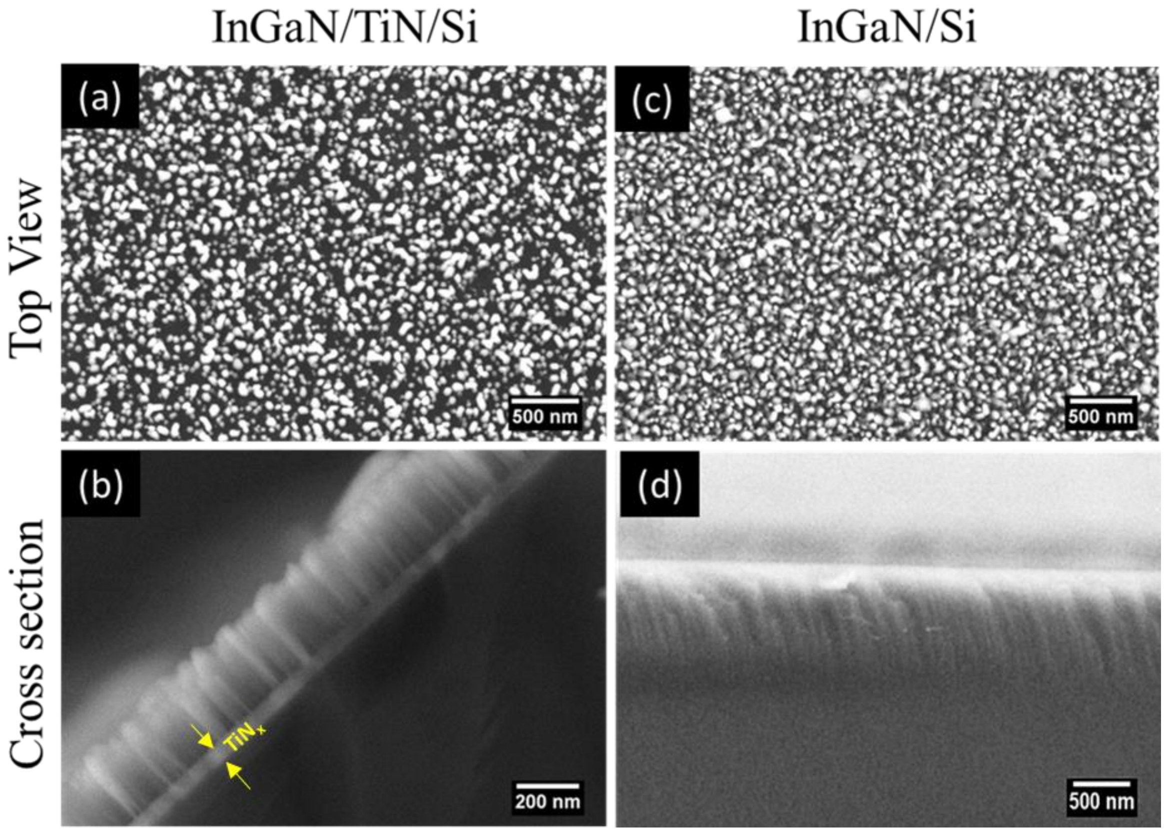

Figure 5.7 FESEM morphologies of InGaN grown on (a) Si and (c) TiN/Si, and their respective cross-section images (b) and (d).

To understand the structural properties and to determine indium concentration, we carried out XRD measurements. The recorded patterns are shown in Figure 5.8, which reveals that InGaN grows epitaxially on TiN as well as on Si substrates with c-axis orients along the growth direction. Insets in Figure 5.8 are deconvoluted (0002) peaks into gaussian components, which indicate the formation of the different phases. It can be observed in Figure 5.8a, that only one phase is dominant when InGaN is grown on Si (111) with a TiN interfacial layer. While in Figure 5.8b, three phases are clearly formed on the bare Si (111) surface. The peak around 34.5° in both the samples observed in the deconvoluted (0002) peak is due to GaN. Indium concentrations in each of the phases are calculated by using Vegard's law (Eq. 3.1) and are found to be $In_xGa_{1-x}N$ phases with indium 15% and 37% (average of 21%) on Si and 5% on TiN/Si. Since the lattice mismatch[205] between TiN and GaN is less (≈ 6%) compared to that between TiN and InGaN, the growth of GaN on TiN is more favored. This results in low indium concentration in the InGaN/TiN/Si sample, due to increased time for the nucleation of GaN on this surface. Further, HRXRD phi-scan of $(10\bar{1}1)$ plane of InGaN

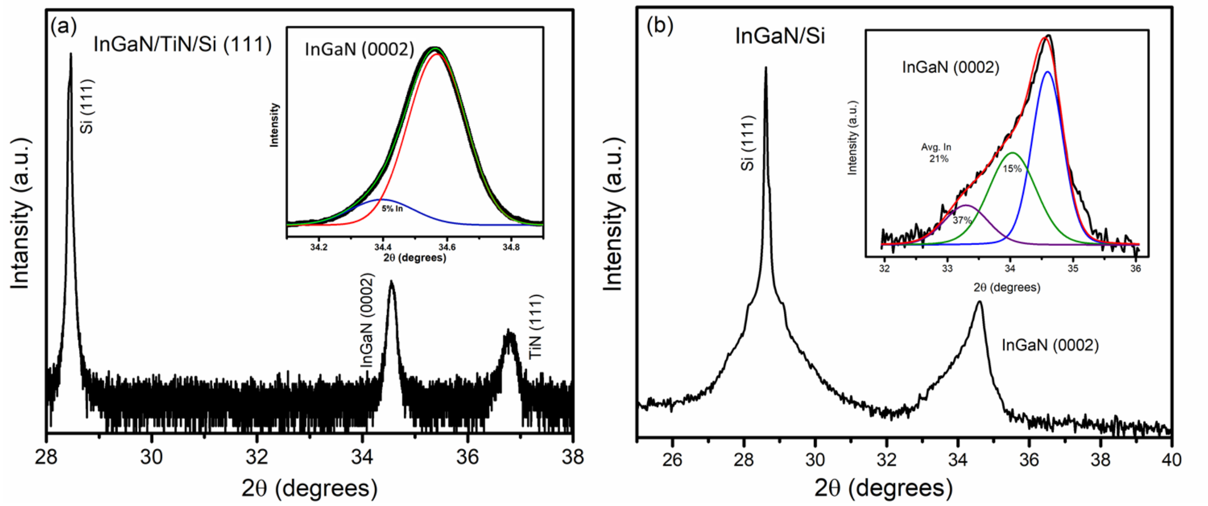

Figure 5.8 XRD patterns of InGaN grown on (a) TiN/Si and (b) Si. Insets show the deconvoluted InGaN (0002) peaks

grown on TiN/Si is shown in Figure 5.9. phi-scan shows six equally spaced peaks (60^{o} apart), confirming the hexagonal crystal symmetry of the film and the epitaxial orientation along the c-direction.

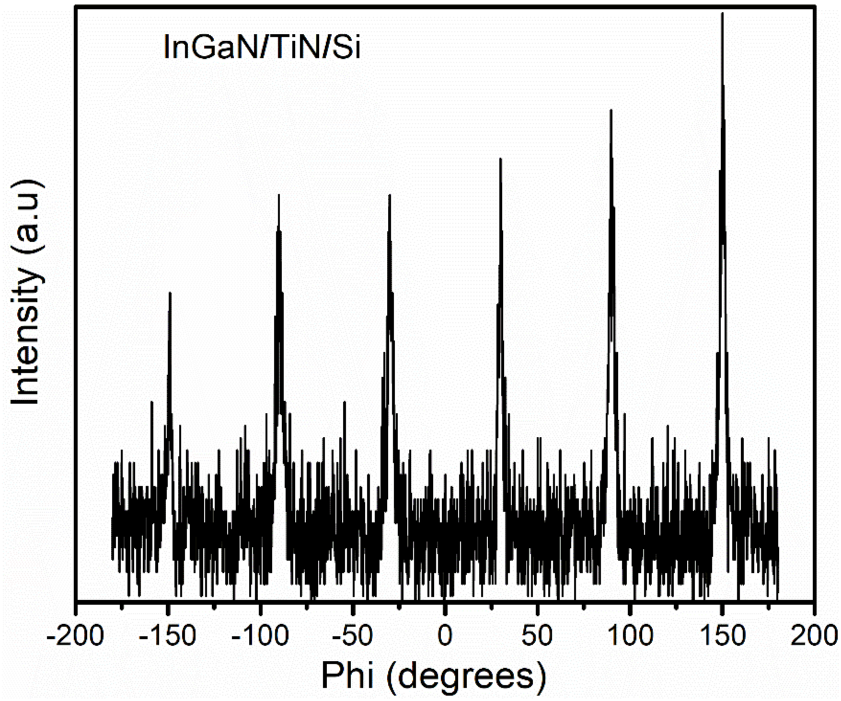

Figure 5.9 Phi-Scan of InGaN (10-11) plane acquired by HRXRD of InGaN/TiN/Si,

5.2.2.2 PEC measurements

To understand the effect of TiN interfacial layer on PEC properties, we fabricated the photochemical device by making ohmic contact with indium on TiN in InGaN/TiN/Si electrode and with aluminium on Si made on the InGaN/Si electrode. Again, the contact regions were covered with insulated epoxy and Teflon tape to avoid corrosion of the contact with the acidic electrolyte. Using these photoelectrodes, we measured photocurrent densities in 1M HCl electrolyte under Xe lamp with 180W with visible band pass filter by sweeping voltage against SCE, as shown in Figure 5.10a. It is clearly observed from the plot that the onset potential for both the electrodes are different and in case of InGaN/TiN/Si onset potential is shifted towards the negative side (cathodic shift) as compared to that of InGaN/Si. This shift in InGaN/Si may be due to the formation of an amorphous SiN_x layer during the growth of InGaN at the interface and building a potential barrier[204]. The improved carrier extraction efficiency in InGaN/TiN/Si may be attributed to reduced interfacial resistance. Also, the figure clearly shows that the dark current density observed in both samples is negligible. However, when exposed to light the photocurrent density increases significantly.

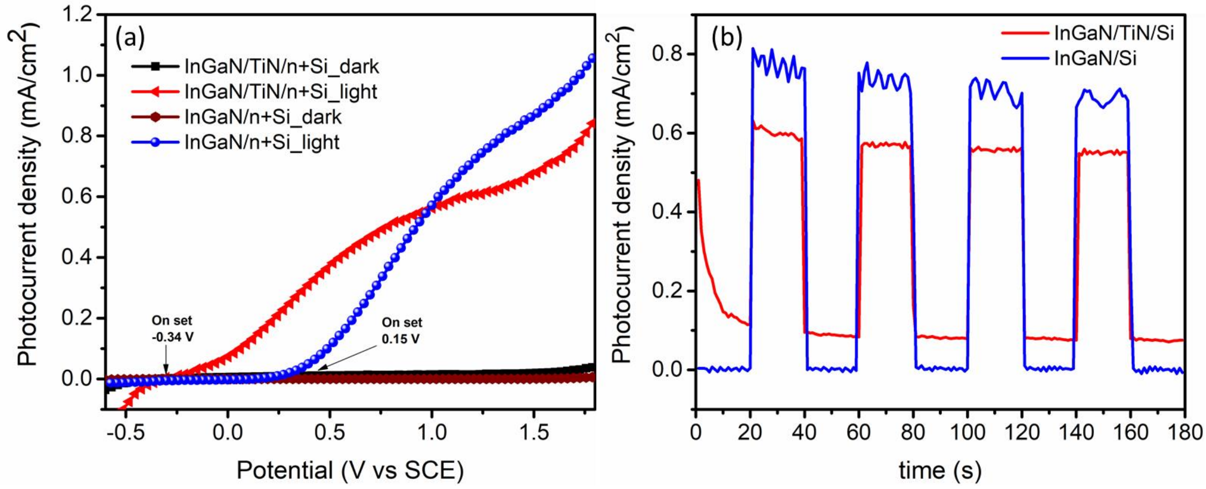

Figure 5.10 (a) The variation in photocurrent density (under dark and illumination using visible band filter) as a function of potential for InGaN grown on Si and TiN/Si (b) The transient photo response at a potential of 1.2 V Vs SCE.

It is clear from the figure that the onset of photocurrent is different in both samples. The onset is -0.34 V in the sample with an intermediate TiN layer, while it is +0.15 V when InGaN was grown on bare Si. However, as the potential increases, the sample with TiN layer increases upto about +0.5 V and then displays a reduced photocurrent density increase from 0.5 V to

1.5 V before beginning to increase again. However, in case of InGaN on bare Si, the photocurrent density increase much faster, reaching a value of >1.0 mA/cm^2, with a reduced plateau region between 1.0-1.5 V region.

Chronoamperometric experiments of both electrodes are carried out in HCl electrolyte at an applied bias of 1.2V by switching light (Chopping) OFF/ON every 20 seconds and the transient photo responses are as shown in Figure 5.10b. Also, no overshoot when switched on the light in photocurrent density shows better hole transfer efficiency[196] in both photoelectrodes. Further, Figure 5.11 represents the results of the transient photo response at a potential of 1.2 V, and shows the variation in photocurrent densities with the time in 1M HCl solution of about 40 minutes for both the photoelectrodes InGaN/Si and InGaN/TiN/Si. As compared to the photoelectrode without TiN, the photoelectrode with TiN layer showed better stability, though with a lower photocurrent density of 0.6 mA/cm^2, while the same for InGaN grown on bare Si, shows a monotonic decrease from 0.8 to 0.65 mA/cm^2 over 2500 seconds. The stability degradation in InGaN/Si is partially attributed to SiN$_x$ layer formation at the interface, which is reported to be rapidly etched during the water splitting process leading to associated GaN etching and also increased interfacial resistance[210].

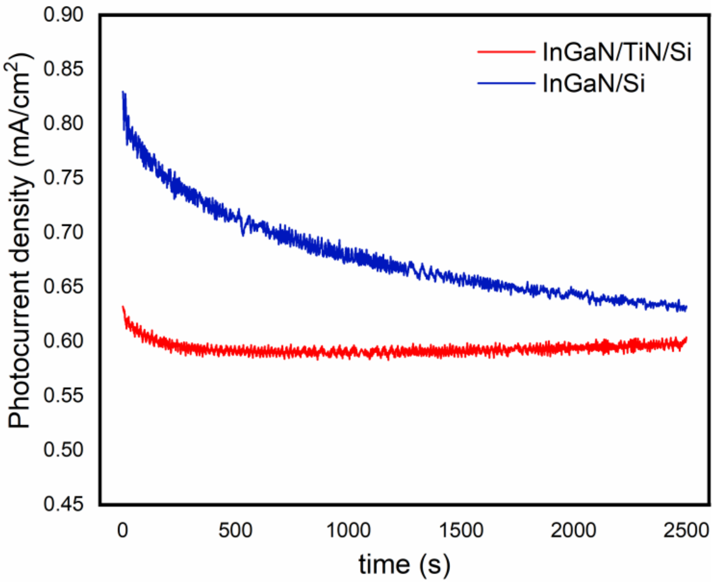

Figure 5.11 Photocurrent density versus time showing stabilities of InGaN/Si and InGaN/TiN/Si photoelectrodes at a bias of 1.2V, in 1M HCl electrolyte.

Further, to understand the onset potential observed for InGaN/Si, we carried out capacitance-voltage (CV) measurements at room temperature at a frequency of 100 kHz. The

CV measurements are carried out on samples S1 and S2 described in section 5.1. Figure 5.12 shows the $1/C^2$ vs V plot for InGaN on Si, for S1 and S2. The built-in potential is extracted from the intercept at voltage axis of $1/C^2$ vs V plot. The values are found to be 0.40 V and 0.49 V for S1 and S2 samples, respectively. This built-in potential can be attributed to the presence of the interfacial SiN_x layer. The shift in onset potential between InGaN/TiN/Si and InGaN/Si in Figure 5.10a is also 0.49 V, which has an approximately similar value as the built-in potential in InGaN/Si (S1 and S2). This suggests that the SiN_x layer in InGaN/Si samples is the reason for the shift in the onset potential we observe in this study.

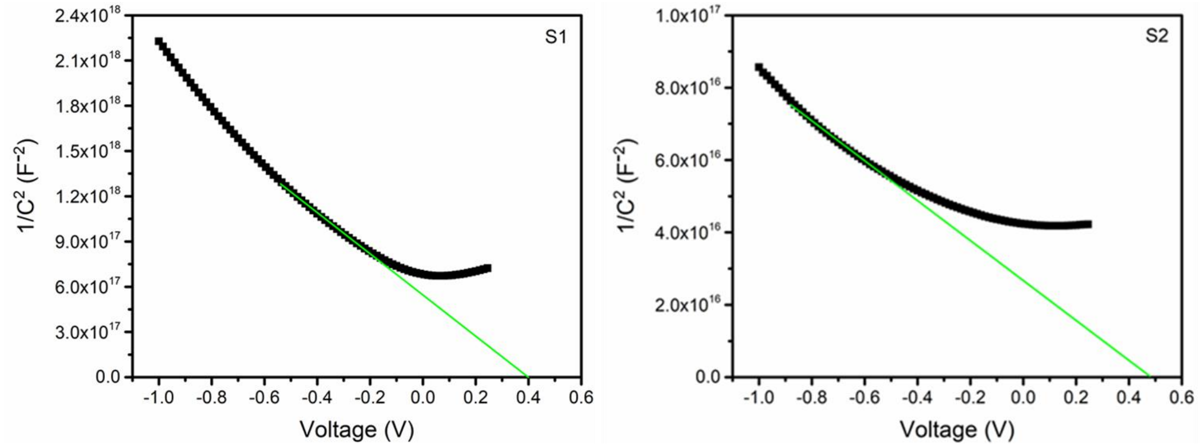

Figure 5.12 $1/C^2$ vs V plot for InGaN/Si (S1 and S2 from section 5.1)

5.2.3 Inferences

In this section, we have studied the impact of an interfacial TiN layer and the SiN_x layer on PEC properties and their role in indium incorporation in InGaN, which shows significant variation in indium composition of 5% in InGaN/TiN/Si compared to that of 21% in InGaN/Si. In PEC measurements, due to interface resistance of an unintentionally formed SiN_x layer in the InGaN/Si case results in the anodic shift in onset potential from -0.34 V to +0.15 V. By depositing a TiN layer on Si, the effect of SiN_x layer on PEC properties is avoided. Consequently, improved the carrier extraction efficiency by reducing the interfacial resistance in the InGaN/TiN/Si. In addition, built-in potential in InGaN/Si at about +0.49 V, which closely matches with onset potential shift, suggests the role of SiN_x layer.

Chapter 6
Summary and Future Directions

This chapter gives a summary of the work done, lists the limitations, and suggests further research work that can be undertaken to explore more possibilities and processes that can yield a highly efficient and stable system for water splitting.

.

6.1 Summary

In Chapter 3, GaN nanowall network (NWN) was grown in MBE spontaneously without any catalyst and formed a heterostructure with TiO_2 grown by ALD technique. We compared mainly the photoelectrochemical properties of GaN NWN/ TiO_2 (TGN) and GaN epilayer/TiO_2 (TGE) heterostructures with the $In_xGa_{1-x}N/TiO_2$ (TIGN) heterostructures. The FESEM images show the conformal coating of TiO_2 on GaN and nanowall network morphology of GaN and the XRD and Raman experiments confirm the anatase crystal structure of TiO_2. From XPS valence band spectra Fermi level positions in each sample were obtained which we used in arriving at the band diagram to understand the characteristics of the heterostructure. The photoelectrochemical properties of TiO_2/GaN heterostructure with two different morphologies of GaN were studied and it was known that the structure with GaN nanowall network morphology (TGN) displayed a better photoelectrochemical response with a photocurrent density of ~0.65 mA/cm^2 and an IPCE of 17% compared to 0.24 mA/cm^2 and 6% of the planar GaN based heterostructure (TGE), at an applied bias of 1.24 V and at an incident power of only 13mW/cm^2. The chronoamperometric analysis also showed very high stability of both electrodes. The better photo response in TGN was shown to be due to appropriate band bending at the interface, and the improved light absorption was attributed to the NWN morphology. The band diagram showed a higher barrier height of 1.8 eV for the TGN structure compared to that of 1.4 eV for TGE, which favors photogenerated charge separation.

In the second section, the fabrication of InGaN/TiO_2 heterostructures by coating GaN nanostructured films with TiO_2 using ALD, were discussed. The structural, morphological, optical and photoelectrochemical properties were studied. The In concentrations were extracted to be 13% and 16% from XRD by using Vegard's law with the help of lattice parameters obtained from XRD. The energy band gap extracted from the Tauc plot, and the emission peak observed from room temperature photoluminescence showed absorption and emission in the visible region and good transient photo response characteristics. The InGaN/TiO_2 structure with higher In composition showed a higher photocurrent density with ~160 μA/cm^2 for heterostructure with more indium compared to ~ 17μA/cm^2 with lower indium, due to the improved light absorption and enhanced charge separation which has been attributed to the interfacial band bending.

In Chapter 4, we understood the role of composition and surface properties on photoelectrochemical properties. We fabricated InGaN photoelectrodes with different indium compositions and with different morphologies by systematically changing the growth parameters. The In concentration in InGaN was controlled by varying the substrate temperature and different morphologies for samples with similar indium composition (~33%) were achieved by varying the film thickness and N_2 flow rates. The HRXRD showed the variation in indium composition and the FESEM images confirmed the variation in surface morphology. The optical absorption and emission studies showed the fabricated thin-film structures have energy bands in the visible region. The samples grown at different substrate temperatures showed a systematic change in optical energy, whereas the samples grown at different N_2 flow rates and thicknesses showed a difference only in the morphology but not in the indium composition and band gap (~2.1 eV). Our results show that the photoelectrochemical properties not only depended on the indium incorporation but also on the surface morphology. Photoelectrochemical measurements showed a significant increase in the photocurrent density by changing the surface morphology. We have seen that the photocurrent density is increased 4 times from 0.25 to 0.90 mA/cm^2 at a potential of 1V vs SCE by varying the morphology, demonstrating that the surface to volume ratio is also as significant as the bandgap of the material in determining the photoelectrochemical properties. The chronoamperometric analysis showed that the electrodes are fast responsive to light and their stability is good under the experimental conditions.

InGaN with different indium concentrations by varying indium flux (or k-cell temperature) and their photoelectrochemical properties were discussed in the second section. We fabricated InGaN photoelectrodes with different morphologies and with systematic incorporation of indium (9 to, 21 and 31%) as calculated using HRXRD data by using Vegard's law. Bandgaps were varied systematically as varified by Tauc's plots. All these factors are seen to help in observing good photocurrent densities. Among these samples, the sample with the highest indium concentration showed excellent performance in photocurrent density (~1mA/cm^2) as well as onset potential compared to the other two samples.

InGaN samples were deposited by varying gallium k-cell temperature (Ga flux) and studied the effects of different electrolytes such as Na_2SO_4, HCl and NaOH, which was discussed in the third section. We have observed an onset shift in photocurrent density, and more shift in case of NaOH due to the favorable potential of oxidation of OH^-(+0.4 V) compared to oxidation of water (+1.23 V). Samples were also found to be etched out after the PEC measurements, the FESEM images and XRD patterns before and after, revealed the etching of samples.

In Chapter 5, we studied the PEC properties of $In_xGa_{1-x}N$ grown on n^+ Si (111) substrates and from FESEM images we observed different morphologies of nanostructures. Significant photocurrent densities are observed in these samples compared to InGaN grown on c-sapphire substrates as observed in Chapter 4. Stability studies show that these photoelectrodes are not stable in HCl electrolyte for long period due to minor etching as is revealed by FESEM measurements. In the second section of this chapter, we studied the impact of TiN layer on PEC properties and its role in indium incorporation in InGaN. We found that due to interface resistance by SiN_x layer in InGaN/Si anodic shift in onset potential was observed and by depositing TiN on Si to avoid SiN_x layer formation, we improved the carrier extraction efficiency by reducing the interfacial resistance in InGaN/TiN/Si. In addition, observation of a built-in potential in InGaN/Si helped in understanding the shift in onset potential.

6.2 Limitations and Future directions

Though we have clearly demonstrated the potential of the use of InGaN and its heterostructures in highly efficient water splitting applications, phase separation in $In_xGa_{1-x}N$ thin films with high indium compositions and lack of proper substrate to grow III-nitrides that result in defects, are seen to affect the structural, optical, electrical properties, etc. which can be a real roadblock for device fabrication. Nitride semiconductors are also not stable in basic (alkaline) solutions which etch the electrode material. Hence causing difficult to carry out PEC measurements for a longer duration. These are some limitations, which need to be overcome in future experiments.

Further, in continuation of the present work discussed in the thesis, some experiments need to be carried out to improve the properties. The etching of InGaN samples in the electrolytes observed in the work can be reduced by further optimizing growth conditions and depositing different passivation layers on them. The enhancement of PEC properties can be studied for forming more interesting heterostructures by depositing nanoparticles such as silver, gold, etc. We have seen in Chapter 3, we fabricated heterostructure with TiO_2 demonstrating improved performance. However, we can further experiment it on homoepitaxial growth by depositing p-InGaN by optimizing magnesium incorporation in InGaN to achieve better quality p-type InGaN, which can help in reducing defects in the film compared to other heterostructures due to large lattice mismatches. Also, tandem structures with InGaN layers of varying In-Ga compositions can be explored so that we can absorb the maximum available energy of the solar spectrum for PEC water splitting experiments. As discussed in Chapter 5 TiN growth on Si, similar attempts can be carried out by depositing TiN on c-Sapphire, which can also be used as back contact in devices. It will be interesting to grow InAlN and InAlGaN to span the whole UV to IR, covering most of the solar spectrum, but for PEC applications with suitable bandgap can be optimized and investigate the properties. Overall, the present study has shown the potential of various interfaces with GAN nanostructures for water splitting applications. However, further work is necessary to optimize heterostructure formation, chemical stability and bandgap tuning to significantly enhance charge separation for the exploration of this system more efficiently. The processes and methods used here are very expensive, and so the efficacy of the system outweigh the cost involved. Other inexpensive methods of forming such nanostructures and interfaces can also be explored in the near future.

Bibliography

(1) Ambacher, O. Growth and Applications of Group III-Nitrides. *J. Phys. D: Appl. Phys.* **1998**, *31* (20), 2653–2710. https://doi.org/10.1088/0022-3727/31/20/001.

(2) Ponce, F. A.; Bour, D. P. Nitride-Based Semiconductors for Blue and Green Light-Emitting Devices. *Nature* **1997**, *386* (6623), 351–359. https://doi.org/10.1038/386351a0.

(3) Wu, J. When Group-III Nitrides Go Infrared: New Properties and Perspectives. *Journal of Applied Physics* **2009**, *106* (1), 011101. https://doi.org/10.1063/1.3155798.

(4) Nakamura, S. The Roles of Structural Imperfections in InGaN-Based Blue Light-Emitting Diodes and Laser Diodes. *Science* **1998**, *281* (5379), 956–961. https://doi.org/10.1126/science.281.5379.956.

(5) Butcher, K. S. A.; Tansley, T. L. InN, Latest Development and a Review of the Band-Gap Controversy. *Superlattices and Microstructures* **2005**, *38* (1), 1–37. https://doi.org/10.1016/j.spmi.2005.03.004.

(6) Morkoç, H. Potential Applications of III–V Nitride Semiconductors. *Materials Science and Engineering: B* **1997**, *43* (1), 137–146. https://doi.org/10.1016/S0921-5107(96)01849-1.

(7) Nanishi, Y.; Saito, Y.; Yamaguchi, T. RF-Molecular Beam Epitaxy Growth and Properties of InN and Related Alloys. *Jpn. J. Appl. Phys.* **2003**, *42* (5R), 2549. https://doi.org/10.1143/JJAP.42.2549.

(8) Bhuiyan, A. G.; Hashimoto, A.; Yamamoto, A. Indium Nitride (InN): A Review on Growth, Characterization, and Properties. *Journal of Applied Physics* **2003**, *94* (5), 2779–2808. https://doi.org/10.1063/1.1595135.

(9) Wang, X.; Yoshikawa, A. Molecular Beam Epitaxy Growth of GaN, AlN and InN. *Progress in Crystal Growth and Characterization of Materials* **2004**, *48–49*, 42–103. https://doi.org/10.1016/j.pcrysgrow.2005.03.002.

(10) Khan, A.; Balakrishnan, K.; Katona, T. Ultraviolet Light-Emitting Diodes Based on Group Three Nitrides. *Nature Photon* **2008**, *2* (2), 77–84. https://doi.org/10.1038/nphoton.2007.293.

(11) Strite, S.; Morkoç, H. GaN, AlN, and InN: A Review. *Journal of Vacuum Science & Technology B: Microelectronics and Nanometer Structures Processing, Measurement, and Phenomena* **1992**, *10* (4), 1237–1266. https://doi.org/10.1116/1.585897.

(12) Gil, B. *Group III Nitride Semiconductor Compounds: Physics and Applications*; Clarendon Press: Oxford [England, 1998.

(13) Morkoç, H. *Nitride Semiconductor Devices: Fundamentals and Applications*; John Wiley & Sons, 2013.

(14) Wu, J.; Walukiewicz, W.; Shan, W.; Yu, K. M.; Ager, J. W.; Li, S. X.; Haller, E. E.; Lu, H.; Schaff, W. J. Temperature Dependence of the Fundamental Band Gap of InN. *Journal of Applied Physics* **2003**, *94* (7), 4457–4460. https://doi.org/10.1063/1.1605815.

(15) Feneberg, M.; Leute, R. A. R.; Neuschl, B.; Thonke, K.; Bickermann, M. High-Excitation and High-Resolution Photoluminescence Spectra of Bulk AlN. *Phys. Rev. B* **2010**, *82* (7), 075208. https://doi.org/10.1103/PhysRevB.82.075208.

(16) Jain, S. C.; Willander, M.; Narayan, J.; Overstraeten, R. V. III–Nitrides: Growth, Characterization, and Properties. *Journal of Applied Physics* **2000**, *87* (3), 965–1006. https://doi.org/10.1063/1.371971.

(17) Kaun, S. W.; Wong, M. H.; Mishra, U. K.; Speck, J. S. Molecular Beam Epitaxy for High-Performance Ga-Face GaN Electron Devices. *Semicond. Sci. Technol.* **2013**, *28* (7), 074001. https://doi.org/10.1088/0268-1242/28/7/074001.

(18) Juza, R.; Hahn, H. Über die Kristallstrukturen von Cu3N, GaN und InN Metallamide und Metallnitride. *Zeitschrift für anorganische und allgemeine Chemie* **1938**, *239* (3), 282–287. https://doi.org/10.1002/zaac.19382390307.

(19) Maruska, H. P.; Tietjen, J. J. THE PREPARATION AND PROPERTIES OF VAPOR-DEPOSITED SINGLE-CRYSTAL-LINE GaN. *Appl. Phys. Lett.* **1969**, *15* (10), 327–329. https://doi.org/10.1063/1.1652845.

(20) Pankove, J. I.; Miller, E. A.; Richman, D.; Berkeyheiser, J. E. Electroluminescence in GaN. *Journal of Luminescence* **1971**, *4* (1), 63–66. https://doi.org/10.1016/0022-2313(71)90009-3.

(21) Amano, H.; Kito, M.; Hiramatsu, K.; Akasaki, I. P-Type Conduction in Mg-Doped GaN Treated with Low-Energy Electron Beam Irradiation (LEEBI). *Jpn. J. Appl. Phys.* **1989**, *28* (12A), L2112. https://doi.org/10.1143/JJAP.28.L2112.

(22) Nakamura, S.; Mukai, T. M. T.; Senoh, M. S. M. High-Power GaN P-N Junction Blue-Light-Emitting Diodes. *Jpn. J. Appl. Phys.* **1991**, *30* (12A), L1998. https://doi.org/10.1143/JJAP.30.L1998.

(23) Nakamura, S.; Senoh, M. S. M.; Mukai, T. M. T. P-GaN/N-InGaN/N-GaN Double-Heterostructure Blue-Light-Emitting Diodes. *Jpn. J. Appl. Phys.* **1993**, *32* (1A), L8. https://doi.org/10.1143/JJAP.32.L8.

(24) Nakamura, S.; Senoh, M.; Iwasa, N.; Nagahama, S. N. S. High-Brightness InGaN Blue, Green and Yellow Light-Emitting Diodes with Quantum Well Structures. *Jpn. J. Appl. Phys.* **1995**, *34* (7A), L797. https://doi.org/10.1143/JJAP.34.L797.

(25) Nakamura, S. III-V Nitride-Based Light-Emitting Diodes. *Diamond and Related Materials* **1996**, *5* (3), 496–500. https://doi.org/10.1016/0925-9635(96)80067-7.

(26) George, T.; Jacobsohn, E.; Pike, W. T.; Chang-Chien, P.; Khan, M. A.; Yang, J. W.; Mahajan, S. Novel Symmetry in the Growth of Gallium Nitride on Magnesium Aluminate Substrates. *Appl. Phys. Lett.* **1996**, *68* (3), 337–339. https://doi.org/10.1063/1.116708.

(27) Kuramata, A.; Horino, K.; Domen, K.; Shinohara, K.; Tanahashi, T. High-quality GaN Epitaxial Layer Grown by Metalorganic Vapor Phase Epitaxy on (111) MgAl2O4 Substrate. *Appl. Phys. Lett.* **1995**, *67* (17), 2521–2523. https://doi.org/10.1063/1.114445.

(28) Sun, C. J.; Yang, J. W.; Chen, Q.; Asif Khan, M.; George, T.; Chang-Chien, P.; Mahajan, S. Deposition of High Quality Wurtzite GaN Films over Cubic (111) MgAl2O4 Substrates Using Low Pressure Metalorganic Chemical Vapor Deposition. *Appl. Phys. Lett.* **1996**, *68* (8), 1129–1131. https://doi.org/10.1063/1.115735.

(29) Popovici, G.; Kim, W.; Botchkarev, A.; Tang, H.; Morkoç, H.; Solomon, J. Impurity Contamination of GaN Epitaxial Films from the Sapphire, SiC and ZnO Substrates. *Appl. Phys. Lett.* **1997**, *71* (23), 3385–3387. https://doi.org/10.1063/1.120343.

(30) Kobayashi, N. P.; Kobayashi, J. T.; Dapkus, P. D.; Choi, W.-J.; Bond, A. E.; Zhang, X.; Rich, D. H. GaN Growth on Si(111) Substrate Using Oxidized AlAs as an Intermediate Layer. *Appl. Phys. Lett.* **1997**, *71* (24), 3569–3571. https://doi.org/10.1063/1.120394.

(31) Li, W.; Ni, W. Residual Strain in GaN Epilayers Grown on Sapphire and (6H)SiC Substrates. *Appl. Phys. Lett.* **1996**, *68* (19), 2705–2707. https://doi.org/10.1063/1.116315.

(32) Kung, P.; Saxler, A.; Zhang, X.; Walker, D.; Lavado, R.; Razeghi, M. Metalorganic Chemical Vapor Deposition of Monocrystalline GaN Thin Films on Β-LiGaO2 Substrates. *Appl. Phys. Lett.* **1996**, *69* (14), 2116–2118. https://doi.org/10.1063/1.116898.

(33) Hamdani, F.; Yeadon, M.; Smith, D. J.; Tang, H.; Kim, W.; Salvador, A.; Botchkarev, A. E.; Gibson, J. M.; Polyakov, A. Y.; Skowronski, M.; Morkoç, H. Microstructure and Optical Properties of Epitaxial GaN on ZnO (0001) Grown by Reactive Molecular Beam Epitaxy. *Journal of Applied Physics* **1998**, *83* (2), 983–990. https://doi.org/10.1063/1.366786.

(34) Kaiser, S.; Preis, H.; Gebhardt, W.; Ambacher, O.; Angerer, H.; Stutzmann, M.; Rosenauer, A.; Gerthsen, D. Quantitative Transmission Electron Microscopy Investigation of the Relaxation by Misfit Dislocations Confined at the Interface of GaN/Al2O3(0001). *Jpn. J. Appl. Phys.* **1998**, *37* (1R), 84. https://doi.org/10.1143/JJAP.37.84.

(35) Kelly, M. K.; Ambacher, O.; Dimitrov, R.; Handschuh, R.; Stutzmann, M. Optical Process for Liftoff of Group III-Nitride Films. *physica status solidi (a)* **1997**, *159* (1), R3–R4. https://doi.org/10.1002/1521-396X(199701)159:1<R3::AID-PSSA99993>3.0.CO;2-F.

(36) Paszkowicz, W.; Černý, R.; Krukowski, S. Rietveld Refinement for Indium Nitride in the 105–295 K Range. *Powder Diffraction* **2003**, *18* (2), 114–121. https://doi.org/10.1154/1.1566957.

(37) Tanaka, M.; Nakahata, S.; Sogabe, K.; Nakata, H. N. H.; Tobioka, M. T. M. Morphology and X-Ray Diffraction Peak Widths of Aluminum Nitride Single Crystals Prepared by the Sublimation Method. *Jpn. J. Appl. Phys.* **1997**, *36* (8B), L1062. https://doi.org/10.1143/JJAP.36.L1062.

(38) Darakchieva, V.; Monemar, B.; Usui, A. On the Lattice Parameters of GaN. *Appl. Phys. Lett.* **2007**, *91* (3), 031911. https://doi.org/10.1063/1.2753122.

(39) Wu, M. F.; Zhou, S. Q.; Vantomme, A.; Huang, Y.; Wang, H.; Yang, H. High-Precision Determination of Lattice Constants and Structural Characterization of InN Thin Films. *Journal of Vacuum Science & Technology A* **2006**, *24* (2), 275–279. https://doi.org/10.1116/1.2167970.

(40) Liu, L.; Edgar, J. H. Substrates for Gallium Nitride Epitaxy. *Materials Science and Engineering: R: Reports* **2002**, *37* (3), 61–127. https://doi.org/10.1016/S0927-796X(02)00008-6.

(41) Dovidenko, K.; Oktyabrsky, S.; Narayan, J.; Razeghi, M. Aluminum Nitride Films on Different Orientations of Sapphire and Silicon. *Journal of Applied Physics* **1996**, *79* (5), 2439–2445. https://doi.org/10.1063/1.361172.

(42) Grandal, J.; Sánchez-García, M. a.; Calle, F.; Calleja, E. Morphology and Optical Properties of InN Layers Grown by Molecular Beam Epitaxy on Silicon Substrates. *physica status solidi (c)* **2005**, *2* (7), 2289–2292. https://doi.org/10.1002/pssc.200461571.

(43) Davydov, V. Yu.; Klochikhin, A. a.; Emtsev, V. v.; Ivanov, S. v.; Vekshin, V. v.; Bechstedt, F.; Furthmüller, J.; Harima, H.; Mudryi, A. v.; Hashimoto, A.; Yamamoto, A.; Aderhold, J.; Graul, J.; Haller, E. e. Band Gap of InN and In-Rich InxGa1—XN Alloys (0.36 < x < 1). *physica status solidi (b)* **2002**, *230* (2), R4–R6. https://doi.org/10.1002/1521-3951(200204)230:2<R4::AID-PSSB99994>3.0.CO;2-Z.

(44) Anani, M.; Abid, H.; Chama, Z.; Mathieu, C.; Sayede, A.; Khelifa, B. InxGa1−xN Refractive Index Calculations. *Microelectronics Journal* **2007**, *38* (2), 262–266. https://doi.org/10.1016/j.mejo.2006.11.001.

(45) McLaughlin, D. V. P.; Pearce, J. M. Analytical Model for the Optical Functions of Indium Gallium Nitride with Application to Thin Film Solar Photovoltaic Cells. *Materials Science and Engineering: B* **2012**, *177* (2), 239–244. https://doi.org/10.1016/j.mseb.2011.12.008.

(46) Vurgaftman, I.; Meyer, J. R. Band Parameters for Nitrogen-Containing Semiconductors. *Journal of Applied Physics* **2003**, *94* (6), 3675–3696. https://doi.org/10.1063/1.1600519.

(47) Jani, O.; Ferguson, I.; Honsberg, C.; Kurtz, S. Design and Characterization of GaN/InGaN Solar Cells. *Appl. Phys. Lett.* **2007**, *91* (13), 132117. https://doi.org/10.1063/1.2793180.

(48) Grandal, J.; Pereiro, J.; Bengoechea-Encabo, A.; Fernández-Garrido, S.; Sánchez-García, M. A.; Muñoz, E.; Calleja, E.; Luna, E.; Trampert, A. InN/InGaN Multiple Quantum Wells Emitting at 1.5 Mm Grown by Molecular Beam Epitaxy. *Appl. Phys. Lett.* **2011**, *98* (6), 061901. https://doi.org/10.1063/1.3552195.

(49) High Efficiency, Radiation-Hard Solar Cells.

(50) Farrell, R. M.; Neufeld, C. J.; Cruz, S. C.; Lang, J. R.; Iza, M.; Keller, S.; Nakamura, S.; DenBaars, S. P.; Mishra, U. K.; Speck, J. S. High Quantum Efficiency InGaN/GaN Multiple Quantum Well Solar Cells with Spectral Response Extending out to 520 Nm. *Appl. Phys. Lett.* **2011**, *98* (20), 201107. https://doi.org/10.1063/1.3591976.

(51) Fiorentini, V.; Bernardini, F.; Della Sala, F.; Di Carlo, A.; Lugli, P. Effects of Macroscopic Polarization in III-V Nitride Multiple Quantum Wells. *Phys. Rev. B* **1999**, *60* (12), 8849–8858. https://doi.org/10.1103/PhysRevB.60.8849.

(52) Bernardini, F.; Fiorentini, V. Nonlinear Macroscopic Polarization in III-V Nitride Alloys. *Phys. Rev. B* **2001**, *64* (8), 085207. https://doi.org/10.1103/PhysRevB.64.085207.

(53) Ho, I.; Stringfellow, G. B. Solid Phase Immiscibility in GaInN. *Appl. Phys. Lett.* **1996**, *69* (18), 2701–2703. https://doi.org/10.1063/1.117683.

(54) Nagatomo, T.; Kuboyama, T.; Minamino, H.; Omoto, O. Properties of Ga1-XInxN Films Prepared by MOVPE. *Jpn. J. Appl. Phys.* **1989**, *28* (8A), L1334. https://doi.org/10.1143/JJAP.28.L1334.

(55) Yoshimoto, N.; Matsuoka, T.; Sasaki, T.; Katsui, A. Photoluminescence of InGaN Films Grown at High Temperature by Metalorganic Vapor Phase Epitaxy. *Appl. Phys. Lett.* **1991**, *59* (18), 2251–2253. https://doi.org/10.1063/1.106086.

(56) Piner, E. L.; McIntosh, F. G.; Roberts, J. C.; Aumer, M. E.; Joshkin, V. A.; Bedair, S. M.; El-Masry, N. A. Growth and Properties of InGaN and AlInGaN Thin Films on (0001) Sapphire. *MRS Internet Journal of Nitride Semiconductor Research* **1996**, *1* (1), 43. https://doi.org/10.1557/S1092578300002155.

(57) Kim, D.-J.; Moon, Y.-T.; Song, K.-M.; Lee, I.-H.; Park, S.-J. Effect of Growth Pressure on Indium Incorporation during the Growth of InGaN by MOCVD. *J. Electron. Mater.* **2001**, *30* (2), 99–102. https://doi.org/10.1007/s11664-001-0107-y.

(58) Chen, H.; Feenstra, R. M.; Northrup, J.; Neugebauer, J.; Greve, D. W. Indium Incorporation and Surface Segregation during InGaN Growth by Molecular Beam Epitaxy: Experiment and Theory. *MRS Internet Journal of Nitride Semiconductor Research* **2001**, *6* (1), 11. https://doi.org/10.1557/S1092578300000235.

(59) Kushi, K.; Sasamoto, H.; Sugihara, D.; Nakamura, S.; Kikuchi, A.; Kishino, K. High Speed Growth of Device Quality GaN and InGaN by RF-MBE. *Materials Science*

and Engineering: B **1999**, *59* (1), 65–68. https://doi.org/10.1016/S0921-5107(98)00365-1.

(60) Böttcher, T.; Einfeldt, S.; Kirchner, V.; Figge, S.; Heinke, H.; Hommel, D.; Selke, H.; Ryder, P. L. Incorporation of Indium during Molecular Beam Epitaxy of InGaN. *Appl. Phys. Lett.* **1998**, *73* (22), 3232–3234. https://doi.org/10.1063/1.122728.

(61) Shen, X. Q.; Ide, T.; Shimizu, M.; Okumura, H. Growth and Characterizations of InGaN on N- and Ga-Polarity GaN Grown by Plasma-Assisted Molecular-Beam Epitaxy. *Journal of Crystal Growth* **2002**, *237–239*, 1148–1152. https://doi.org/10.1016/S0022-0248(01)02073-5.

(62) Lee, R. The Outlook for Population Growth. *Science* **2011**, *333* (6042), 569–573. https://doi.org/10.1126/science.1208859.

(63) di Primio, R.; Horsfield, B.; Guzman-Vega, M. A. Determining the Temperature of Petroleum Formation from the Kinetic Properties of Petroleum Asphaltenes. *Nature* **2000**, *406* (6792), 173–176. https://doi.org/10.1038/35018046.

(64) *A review on exergy comparison of hydrogen production methods from renewable energy sources - Energy & Environmental Science (RSC Publishing)*. https://pubs.rsc.org/en/content/articlelanding/2012/ee/c2ee01098d/unauth (accessed 2022-03-28).

(65) *Recent Progress in Metal-Organic Frameworks for Applications in Electrocatalytic and Photocatalytic Water Splitting - Wang - 2017 - Advanced Science - Wiley Online Library*. https://onlinelibrary.wiley.com/doi/full/10.1002/advs.201600371 (accessed 2022-03-28).

(66) Linic, S.; Christopher, P.; Ingram, D. B. Plasmonic-Metal Nanostructures for Efficient Conversion of Solar to Chemical Energy. *Nature Mater* **2011**, *10* (12), 911–921. https://doi.org/10.1038/nmat3151.

(67) *Recent Progress in Energy-Driven Water Splitting - Tee - 2017 - Advanced Science - Wiley Online Library*. https://onlinelibrary.wiley.com/doi/full/10.1002/advs.201600337 (accessed 2022-03-28).

(68) Chiarello, G. L.; Aguirre, M. H.; Selli, E. Hydrogen Production by Photocatalytic Steam Reforming of Methanol on Noble Metal-Modified TiO2. *Journal of Catalysis* **2010**, *273* (2), 182–190. https://doi.org/10.1016/j.jcat.2010.05.012.

(69) Jafari, T.; Moharreri, E.; Amin, A. S.; Miao, R.; Song, W.; Suib, S. L. Photocatalytic Water Splitting—The Untamed Dream: A Review of Recent Advances. *Molecules* **2016**, *21* (7), 900. https://doi.org/10.3390/molecules21070900.

(70) *Artificial photosynthesis for solar water-splitting | Nature Photonics*. https://www.nature.com/articles/nphoton.2012.175 (accessed 2022-03-28).

(71) *Nanomaterials for photoelectrochemical water splitting – review - ScienceDirect*. https://www.sciencedirect.com/science/article/abs/pii/S0360319918301745?via%3Dihub (accessed 2022-03-28).

(72) Ager, J. W.; Shaner, M. R.; Walczak, K. A.; Sharp, I. D.; Ardo, S. Experimental Demonstrations of Spontaneous, Solar-Driven Photoelectrochemical Water Splitting. *Energy Environ. Sci.* **2015**, *8* (10), 2811–2824. https://doi.org/10.1039/C5EE00457H.

(73) Fujishima, A.; Honda, K. Electrochemical Photolysis of Water at a Semiconductor Electrode. *Nature* **1972**, *238* (5358), 37–38. https://doi.org/10.1038/238037a0.

(74) *Solar fuel production: Strategies and new opportunities with nanostructures - ScienceDirect*. https://www.sciencedirect.com/science/article/abs/pii/S1748013215000717 (accessed 2022-03-28).

(75) *E-MRS/MRS Bilateral Energy Conference Innovative Technological Configurations of Photoelectrochemical Cells - ScienceDirect*. https://www.sciencedirect.com/science/article/pii/S1876610212010223 (accessed 2022-03-29).

(76) Smith, W. A. Photoelectrochemical Cell Design, Efficiency, Definitions, Standards, and Protocols. In *Photoelectrochemical Solar Fuel Production: From Basic Principles to Advanced Devices*; Giménez, S., Bisquert, J., Eds.; Springer International Publishing: Cham, 2016; pp 163–197. https://doi.org/10.1007/978-3-319-29641-8_4.

(77) *Solar Water Splitting: Progress Using Hematite (α-Fe2O3) Photoelectrodes - Sivula - 2011 - ChemSusChem - Wiley Online Library*. https://chemistry-europe.onlinelibrary.wiley.com/doi/abs/10.1002/cssc.201000416 (accessed 2022-03-29).

(78) Krol, R. van de; Liang, Y.; Schoonman, J. Solar Hydrogen Production with Nanostructured Metal Oxides. *J. Mater. Chem.* **2008**, *18* (20), 2311–2320. https://doi.org/10.1039/B718969A.

(79) Weber, M. F.; Dignam, M. J. Efficiency of Splitting Water with Semiconducting Photoelectrodes. *J. Electrochem. Soc.* **1984**, *131* (6), 1258. https://doi.org/10.1149/1.2115797.

(80) van de Krol, R.; Grätzel, M. Introduction. In *Photoelectrochemical Hydrogen Production*; van de Krol, R., Grätzel, M., Eds.; Springer US: Boston, MA, 2012; pp 3–11. https://doi.org/10.1007/978-1-4614-1380-6_1.

(81) Khaselev, O.; Turner, J. A. A Monolithic Photovoltaic-Photoelectrochemical Device for Hydrogen Production via Water Splitting. *Science* **1998**, *280* (5362), 425–427. https://doi.org/10.1126/science.280.5362.425.

(82) Lopes, T.; Dias, P.; Andrade, L.; Mendes, A. E-MRS/MRS Bilateral Energy Conference Innovative Technological Configurations of Photoelectrochemical Cells. *Energy Procedia* **2012**, *22,* 35–40. https://doi.org/10.1016/j.egypro.2012.05.229.

(83) Holze, R. C.M.A. Brett, A.M.O. Brett: Electrochemistry — Principles, Methods and Applications, OXford University Press, Oxford, ISBN 0-19-855388-9, 1993, 427

Pages, £ 25.00. *Berichte der Bunsengesellschaft für physikalische Chemie* **1994**, *98* (10), 1350–1350. https://doi.org/10.1002/bbpc.19940981033.

(84) *The concept of Fermi level pinning at semiconductor/liquid junctions. Consequences for energy conversion efficiency and selection of useful solution redox couples in solar devices | Journal of the American Chemical Society*. https://pubs.acs.org/doi/10.1021/ja00531a001 (accessed 2022-03-29).

(85) Wang, D.; Pierre, A.; Kibria, M. G.; Cui, K.; Han, X.; Bevan, K. H.; Guo, H.; Paradis, S.; Hakima, A.-R.; Mi, Z. Wafer-Level Photocatalytic Water Splitting on GaN Nanowire Arrays Grown by Molecular Beam Epitaxy. *Nano letters* **2011**, *11* (6), 2353–2357.

(86) Kocha, S. S.; Peterson, M. W.; Arent, D. J.; Redwing, J. M.; Tischler, M. A.; Turner, J. A. Electrochemical Investigation of the Gallium Nitride-Aqueous Electrolyte Interface. *J. Electrochem. Soc.* **1995**, *142* (12), L238. https://doi.org/10.1149/1.2048511.

(87) Fujii, K.; Karasawa, T.; Ohkawa, K. Hydrogen Gas Generation by Splitting Aqueous Water Using N-Type GaN Photoelectrode with Anodic Oxidation. *Jpn. J. Appl. Phys.* **2005**, *44* (4L), L543. https://doi.org/10.1143/JJAP.44.L543.

(88) Fujii, K.; Kusakabe, K.; Ohkawa, K. Photoelectrochemical Properties of InGaN for H2 Generation from Aqueous Water. *Jpn. J. Appl. Phys.* **2005**, *44* (10R), 7433. https://doi.org/10.1143/JJAP.44.7433.

(89) *Modulating Surface/Interface Structure of Emerging InGaN Nanowires for Efficient Photoelectrochemical Water Splitting - Lin - 2020 - Advanced Functional Materials - Wiley Online Library*. https://onlinelibrary.wiley.com/doi/abs/10.1002/adfm.202005677 (accessed 2022-03-29).

(90) Butson, J.; Narangari, P. R.; Karuturi, S. K.; Yew, R.; Lysevych, M.; Tan, H. H.; Jagadish, C. Photoelectrochemical Studies of InGaN/GaN MQW Photoanodes. *Nanotechnology* **2017**, *29* (4), 045403. https://doi.org/10.1088/1361-6528/aa9eae.

(91) *Improved photoelectrochemical performance of GaN nanopillar photoanodes - IOPscience*. https://iopscience.iop.org/article/10.1088/1361-6528/aa61ed/meta (accessed 2022-03-29).

(92) Benton, J.; Bai, J.; Wang, T. Enhancement in Solar Hydrogen Generation Efficiency Using a GaN-Based Nanorod Structure. *Appl. Phys. Lett.* **2013**, *102* (17), 173905. https://doi.org/10.1063/1.4803926.

(93) Hwang, Y. J.; Wu, C. H.; Hahn, C.; Jeong, H. E.; Yang, P. Si/InGaN Core/Shell Hierarchical Nanowire Arrays and Their Photoelectrochemical Properties. *Nano letters* **2012**, *12* (3), 1678–1682.

(94) Murphy, A. B.; Barnes, P. R. F.; Randeniya, L. K.; Plumb, I. C.; Grey, I. E.; Horne, M. D.; Glasscock, J. A. Efficiency of Solar Water Splitting Using Semiconductor Electrodes. *International Journal of Hydrogen Energy* **2006**, *31* (14), 1999–2017. https://doi.org/10.1016/j.ijhydene.2006.01.014.

(95) Chernomordik, B. D.; Russell, H. B.; Cvelbar, U.; Jasinski, J. B.; Kumar, V.; Deutsch, T.; Sunkara, M. K. Photoelectrochemical Activity of As-Grown, $\upalpha$-Fe2O3nanowire Array Electrodes for Water Splitting. *Nanotechnology* **2012**, *23* (19), 194009. https://doi.org/10.1088/0957-4484/23/19/194009.

(96) *Solar Water Oxidation by an InGaN Nanowire Photoanode with a Bandgap of 1.7 eV | ACS Energy Letters*. https://pubs.acs.org/doi/abs/10.1021/acsenergylett.7b01138 (accessed 2022-03-29).

(97) *A Monolithically Integrated InGaN Nanowire/Si Tandem Photoanode Approaching the Ideal Bandgap Configuration of 1.75/1.13 eV - Fan - 2017 - Advanced Energy Materials - Wiley Online Library*. https://onlinelibrary.wiley.com/doi/10.1002/aenm.201600952 (accessed 2022-03-29).

(98) *A large-scale, ultrahigh-resolution nanoemitter ordered array with PL brightness enhanced by PEALD-grown AlN coating - Nanoscale (RSC Publishing)*. https://pubs.rsc.org/en/content/articlelanding/2019/nr/c8nr07946c/unauth (accessed 2022-03-29).

(99) Huang, J.; Yuan, Y.; Shao, Y.; Yan, Y. Understanding the Physical Properties of Hybrid Perovskites for Photovoltaic Applications. *Nat Rev Mater* **2017**, *2* (7), 1–19. https://doi.org/10.1038/natrevmats.2017.42.

(100) Zhao, C.; Alfaraj, N.; Chandra Subedi, R.; Liang, J. W.; Alatawi, A. A.; Alhamoud, A. A.; Ebaid, M.; Alias, M. S.; Ng, T. K.; Ooi, B. S. III-Nitride Nanowires on Unconventional Substrates: From Materials to Optoelectronic Device Applications. *Progress in Quantum Electronics* **2018**, *61*, 1–31. https://doi.org/10.1016/j.pquantelec.2018.07.001.

(101) Kibria, M. G.; Chowdhury, F. A.; Zhao, S.; AlOtaibi, B.; Trudeau, M. L.; Guo, H.; Mi, Z. Visible Light-Driven Efficient Overall Water Splitting Using p-Type Metal-Nitride Nanowire Arrays. *Nat Commun* **2015**, *6* (1), 6797. https://doi.org/10.1038/ncomms7797.

(102) Kibria, M. G.; Nguyen, H. P. T.; Cui, K.; Zhao, S.; Liu, D.; Guo, H.; Trudeau, M. L.; Paradis, S.; Hakima, A.-R.; Mi, Z. One-Step Overall Water Splitting under Visible Light Using Multiband InGaN/GaN Nanowire Heterostructures. *ACS Nano* **2013**, *7* (9), 7886–7893. https://doi.org/10.1021/nn4028823.

(103) Ebaid, M.; Kang, J.-H.; Lim, S.-H.; Ha, J.-S.; Lee, J. K.; Cho, Y.-H.; Ryu, S.-W. Enhanced Solar Hydrogen Generation of High Density, High Aspect Ratio, Coaxial InGaN/GaN Multi-Quantum Well Nanowires. *Nano Energy* **2015**, *12*, 215–223. https://doi.org/10.1016/j.nanoen.2014.12.033.

(104) *Direct hydrogen gas generation by using InGaN epilayers as working electrodes: Applied Physics Letters: Vol 93, No 16*. https://aip.scitation.org/doi/abs/10.1063/1.3006332 (accessed 2022-03-29).

(105) *GaN with Laterally Aligned Nanopores To Enhance the Water Splitting - The Journal of Physical Chemistry C (ACS Publications)*. https://pubs.acs.org/doi/abs/10.1021/acs.jpcc.7b00748 (accessed 2018-04-19).

(106) *Efficient Light Absorption by GaN Truncated Nanocones for High Performance Water Splitting Applications | ACS Applied Materials & Interfaces*. https://pubs.acs.org/doi/abs/10.1021/acsami.8b09084 (accessed 2022-03-29).

(107) Soto Rodriguez, P. E. D.; Nash, V. C.; Aseev, P.; Gómez, V. J.; Kumar, P.; Alvi, N. U. H.; Sánchez, A.; Villalonga, R.; Pingarrón, J. M.; Nötzel, R. Electrocatalytic Oxidation Enhancement at the Surface of InGaN Films and Nanostructures Grown Directly on Si(111). *Electrochemistry Communications* **2015**, *60*, 158–162. https://doi.org/10.1016/j.elecom.2015.09.003.

(108) Xi, X.; Yang, C.; Cao, H.; Yu, Z.; Li, J.; Lin, S.; Ma, Z.; Zhao, L. GaN Nanocolumns Fabricated by Self-Assembly Ni Mask and Its Enhanced Photocatalytic Performance in Water Splitting. *Applied Surface Science* **2018**, *462*, 310–315. https://doi.org/10.1016/j.apsusc.2018.08.113.

(109) Hou, Y.; Yu, X.; Syed, Z. A.; Shen, S.; Bai, J.; Wang, T. GaN Nano-Pyramid Arrays as an Efficient Photoelectrode for Solar Water Splitting. *Nanotechnology* **2016**, *27* (45), 455401. https://doi.org/10.1088/0957-4484/27/45/455401.

(110) *Molecular beam epitaxy - ScienceDirect*. https://www.sciencedirect.com/science/article/abs/pii/S0039602801015254?via%3Dihub (accessed 2022-03-08).

(111) Heffernan, J.; Kauer, M.; Hooper, S. E.; Bousquet, V.; Johnson, K. InGaN Violet Laser Diodes Grown by Molecular Beam Epitaxy. *physica status solidi (a)* **2004**, *201* (12), 2668–2671. https://doi.org/10.1002/pssa.200405034.

(112) Mao, F. M.; Yang, J. M.; Austin, W. E.; Heck, J. H. Residual Gas Analysers and Their Use in High Vacuum Systems. *Vacuum* **1987**, *37* (3), 335–338. https://doi.org/10.1016/0042-207X(87)90020-0.

(113) Reflection High-Energy Electron Diffraction (RHEED). In *Applied RHEED: Reflection High-Energy Electron Diffraction During Crystal Growth*; Braun, W., Ed.; Springer Tracts in Modern Physics; Springer: Berlin, Heidelberg, 1999; pp 13–26. https://doi.org/10.1007/BFb0109550.

(114) Ichimiya, A.; Cohen, P. I. *Reflection High-Energy Electron Diffraction*; Cambridge University Press: Cambridge, 2004. https://doi.org/10.1017/CBO9780511735097.

(115) Wang, G.-C.; Lu, T.-M. Origins of Texture Formation. In *RHEED Transmission Mode and Pole Figures: Thin Film and Nanostructure Texture Analysis*; Wang, G.-C., Lu, T.-M., Eds.; Springer: New York, NY, 2014; pp 133–147. https://doi.org/10.1007/978-1-4614-9287-0_8.

(116) *Aleskovskii: Chemistry and technology of solids - Google Scholar*. https://scholar.google.com/scholar_lookup?title=Chemistry%20and%20technology%20of%20solids&journal=J%20Appl%20Chem%20USSR&volume=47&pages=2207-2217&publication_year=1974&author=Aleskovskii%2CVB (accessed 2022-03-09).

(117) Suntola, T.; Antson, J. Method for Producing Compound Thin Films. US4058430A, November 15, 1977. https://patents.google.com/patent/US4058430A/en (accessed 2022-03-09).

(118) Leskelä, M.; Ritala, M. Atomic Layer Deposition (ALD): From Precursors to Thin Film Structures. *Thin Solid Films* **2002**, *409* (1), 138–146. https://doi.org/10.1016/S0040-6090(02)00117-7.

(119) Ritala, M.; Leskelä, M. Atomic Layer Deposition. In *Handbook of Thin Films Materials*; Nalwa, H. S., Ed.; Academic Press, 2002; Vol. Volume 1, pp 103–159.

(120) Reimer, L. Elemental Analysis and Imaging with X-Rays. In *Scanning Electron Microscopy: Physics of Image Formation and Microanalysis*; Reimer, L., Ed.; Springer Series in Optical Sciences; Springer: Berlin, Heidelberg, 1998; pp 379–447. https://doi.org/10.1007/978-3-540-38967-5_10.

(121) *Rev. Mod. Phys. 75, 949 (2003) - Advances in atomic force microscopy*. https://journals.aps.org/rmp/abstract/10.1103/RevModPhys.75.949 (accessed 2022-03-09).

(122) *Elements of X-Ray Diffraction | Engineering Mechanics | Introductory Engineering | Science & Engineering | Store | Learner US Site*. https://www.pearson.com/store/p/elements-of-x-ray-diffraction/P100000151708/9780201610918 (accessed 2022-03-13).

(123) Pietsch, U.; Holý, V.; Baumbach, T. Elements for Designing an X-Ray Diffraction Experiment. In *High-Resolution X-Ray Scattering: From Thin Films to Lateral Nanostructures*; Pietsch, U., Holý, V., Baumbach, T., Eds.; Advanced Texts in Physics; Springer: New York, NY, 2004; pp 5–29. https://doi.org/10.1007/978-1-4757-4050-9_1.

(124) *High Resolution X-Ray Diffractometry And Topography*. Routledge & CRC Press. https://www.routledge.com/High-Resolution-X-Ray-Diffractometry-And-Topography/Bowen-Tanner/p/book/9780367400637 (accessed 2022-03-13).

(125) Davydov, V. Yu.; Averkiev, N. S.; Goncharuk, I. N.; Nelson, D. K.; Nikitina, I. P.; Polkovnikov, A. S.; Smirnov, A. N.; Jacobson, M. A.; Semchinova, O. K. Raman and Photoluminescence Studies of Biaxial Strain in GaN Epitaxial Layers Grown on 6H–SiC. *Journal of Applied Physics* **1997**, *82* (10), 5097–5102. https://doi.org/10.1063/1.366310.

(126) Kisielowski, C.; Krüger, J.; Ruvimov, S.; Suski, T.; Ager, J. W.; Jones, E.; Liliental-Weber, Z.; Rubin, M.; Weber, E. R.; Bremser, M. D.; Davis, R. F. Strain-Related Phenomena in GaN Thin Films. *Phys. Rev. B* **1996**, *54* (24), 17745–17753. https://doi.org/10.1103/PhysRevB.54.17745.

(127) Stenzel, O. Introduction. In *The Physics of Thin Film Optical Spectra: An Introduction*; Stenzel, O., Ed.; Springer Series in Surface Sciences; Springer International Publishing: Cham, 2016; pp 1–7. https://doi.org/10.1007/978-3-319-21602-7_1.

(128) Tauc, J. Optical Properties and Electronic Structure of Amorphous Ge and Si. *Materials Research Bulletin* **1968**, *3* (1), 37–46. https://doi.org/10.1016/0025-5408(68)90023-8.

(129) Tauc, J.; Grigorovici, R.; Vancu, A. Optical Properties and Electronic Structure of Amorphous Germanium. *physica status solidi (b)* **1966**, *15* (2), 627–637. https://doi.org/10.1002/pssb.19660150224.

(130) Perkowitz, S. *Optical Characterization of Semiconductors: Infrared, Raman, and Photoluminescence Spectroscopy*; Elsevier, 2012.

(131) Darbandi, M. UV-VIS Spectroscopy/Photoluminescence for Characterization of Silica Coated Core-Shell Nanomaterials. In *UV-VIS and Photoluminescence Spectroscopy for Nanomaterials Characterization*; Kumar, C., Ed.; Springer: Berlin, Heidelberg, 2013; pp 431–452. https://doi.org/10.1007/978-3-642-27594-4_11.

(132) Ozawa, L. *Cathodoluminescence and Photoluminescence: Theories and Practical Applications*; CRC Press: Boca Raton, 2017. https://doi.org/10.1201/9781315219493.

(133) Briggs, D.; Seah, M. P. *Practical Surface Analysis, Auger and X-Ray Photoelectron Spectroscopy*; Wiley, 1990.

(134) *Modern Techniques of Surface Science*. https://www.cambridge.org/core/books/modern-techniques-of-surface-science/46441C87E3A42E5E03C42BCDDFD760AF (accessed 2022-03-13).

(135) *Introduction to Surface Physics*; Oxford University Press: Oxford, New York, 1994.

(136) Hüfner, S. Continuous Satellites and Plasmon Satellites: XPS Photoemission in Nearly Free Electron Systems. In *Photoelectron Spectroscopy: Principles and Applications*; Hüfner, S., Ed.; Advanced Texts in Physics; Springer: Berlin, Heidelberg, 2003; pp 173–209. https://doi.org/10.1007/978-3-662-09280-4_4.

(137) *An Introduction to Surface Analysis by XPS and AES, 2nd Edition | Wiley*. https://www.wiley.com/en-us/An+Introduction+to+Surface+Analysis+by+XPS+and+AES%2C+2nd+Edition-p-9781119417651 (accessed 2022-03-13).

(138) *Measurement of Sheet Resistivities with the Four-Point Probe - Smits - 1958 - Bell System Technical Journal - Wiley Online Library*. https://onlinelibrary.wiley.com/doi/abs/10.1002/j.1538-7305.1958.tb03883.x (accessed 2022-03-11).

(139) Beer, A. C. Hall Effect and the Beauty and Challenges of Science. In *The Hall Effect and Its Applications*; Chien, C. L., Westgate, C. R., Eds.; Springer US: Boston, MA, 1980; pp 299–338. https://doi.org/10.1007/978-1-4757-1367-1_10.

(140) van der PAUW, L. J. A Method of Measuring Specific Resistivity and Hall Effect of Discs of Arbitrary Shape. In *Semiconductor Devices: Pioneering Papers*; WORLD SCIENTIFIC, 1991; pp 174–182. https://doi.org/10.1142/9789814503464_0017.

(141) Chen, Z.; Deutsch, T. G.; Dinh, H. N.; Domen, K.; Emery, K.; Forman, A. J.; Gaillard, N.; Garland, R.; Heske, C.; Jaramillo, T. F.; Kleiman-Shwarsctein, A.; Miller, E.; Takanabe, K.; Turner, J. Experimental Considerations. In *Photoelectrochemical Water Splitting: Standards, Experimental Methods, and*

Protocols; Chen, Z., Dinh, H. N., Miller, E., Eds.; SpringerBriefs in Energy; Springer: New York, NY, 2013; pp 17–44. https://doi.org/10.1007/978-1-4614-8298-7_3.

(142) Hou, Y.; Syed, Z. A.; Smith, R.; Athanasiou, M.; Gong, Y.; Yu, X.; Bai, J.; Wang, T. Enhanced Water Splitting with Silver Decorated GaN Photoelectrode. *J. Phys. D: Appl. Phys.* **2016**, *49* (26), 265601. https://doi.org/10.1088/0022-3727/49/26/265601.

(143) Ravi, L.; Boopathi, K.; Panigrahi, P.; Krishnan, B. Growth of Gallium Nitride Nanowires on Sapphire and Silicon by Chemical Vapor Deposition for Water Splitting Applications. *Applied Surface Science* **2018**. https://doi.org/10.1016/j.apsusc.2018.01.306.

(144) Cao, D.; Xiao, H.; Fang, J.; Liu, J.; Gao, Q.; Liu, X.; Ma, J. Photoelectrochemical Water Splitting on Nanoporous GaN Thin Films for Energy Conversion under Visible Light. *Mater. Res. Express* **2017**, *4* (1), 015019. https://doi.org/10.1088/2053-1591/aa56ee.

(145) Aihua Zhong and Kazuhiro Hane. Characterization of GaN Nanowall Network and Optical Property of InGaN/GaN Quantum Wells by Molecular Beam Epitaxy. *Japanese Journal of Applied Physics* **2013**, *52* (8S), 08JE13.

(146) Guo, P.; Jiang, J.; Shen, S.; Guo, L. ZnS/ZnO Heterojunction as Photoelectrode: Type II Band Alignment towards Enhanced Photoelectrochemical Performance. *International Journal of Hydrogen Energy* **2013**, *38* (29), 13097–13103. https://doi.org/10.1016/j.ijhydene.2013.01.184.

(147) Hong, E.; Kim, J. H. Oxide Content Optimized ZnS–ZnO Heterostructures via Facile Thermal Treatment Process for Enhanced Photocatalytic Hydrogen Production. *International Journal of Hydrogen Energy* **2014**, *39* (19), 9985–9993. https://doi.org/10.1016/j.ijhydene.2014.04.137.

(148) Yu, X.; Zhang, J.; Zhao, Z.; Guo, W.; Qiu, J.; Mou, X.; Li, A.; Claverie, J. P.; Liu, H. NiO–TiO2 p–n Heterostructured Nanocables Bridged by Zero-Bandgap RGO for Highly Efficient Photocatalytic Water Splitting. *Nano Energy* **2015**, *16*, 207–217. https://doi.org/10.1016/j.nanoen.2015.06.028.

(149) Thakur, V.; Kesaria, M.; Shivaprasad, S. M. Enhanced Band Edge Luminescence from Stress and Defect Free GaN Nanowall Network Morphology. *Solid State Communications* **2013**, *171*, 8–13. https://doi.org/10.1016/j.ssc.2013.07.012.

(150) Luttrell, T.; Halpegamage, S.; Tao, J.; Kramer, A.; Sutter, E.; Batzill, M. Why Is Anatase a Better Photocatalyst than Rutile? - Model Studies on Epitaxial TiO_2 Films. *Scientific Reports* **2014**, *4*, srep04043. https://doi.org/10.1038/srep04043.

(151) Ohsaka, T.; Izumi, F.; Fujiki, Y. Raman Spectrum of Anatase, TiO2. *Journal of Raman Spectroscopy* **1978**, *7* (6), 321–324. https://doi.org/10.1002/jrs.1250070606.

(152) Harima, H. Properties of GaN and Related Compounds Studied by Means of Raman Scattering. *J. Phys.: Condens. Matter* **2002**, *14* (38), R967. https://doi.org/10.1088/0953-8984/14/38/201.

(153) Wetzel, C.; Suski, T.; Ager III, J. W.; Weber, E. R.; Haller, E. E.; Fischer, S.; Meyer, B. K.; Molnar, R. J.; Perlin, P. Pressure Induced Deep Gap State of Oxygen in GaN. *Phys. Rev. Lett.* **1997**, *78* (20), 3923–3926. https://doi.org/10.1103/PhysRevLett.78.3923.

(154) Vasu, K.; Sreedhara, M. B.; Ghatak, J.; Rao, C. N. R. Atomic Layer Deposition of P-Type Epitaxial Thin Films of Undoped and N-Doped Anatase TiO2. *ACS Appl. Mater. Interfaces* **2016**, *8* (12), 7897–7901. https://doi.org/10.1021/acsami.6b00628.

(155) Yang, C.; Liu, L.; Zhu, S.; Yu, Z.; Xi, X.; Wu, S.; Cao, H.; Li, J.; Zhao, L. GaN with Laterally Aligned Nanopores To Enhance the Water Splitting. *J. Phys. Chem. C* **2017**, *121* (13), 7331–7336. https://doi.org/10.1021/acs.jpcc.7b00748.

(156) Hou, Y.; Yu, X.; Syed, Z. A.; Shen, S.; Bai, J.; Wang, T. GaN Nano-Pyramid Arrays as an Efficient Photoelectrode for Solar Water Splitting. *Nanotechnology* **2016**, *27*, 455401. https://doi.org/10.1088/0957-4484/27/45/455401.

(157) Wolcott, A.; Smith, W. A.; Kuykendall, T. R.; Zhao, Y.; Zhang, J. Z. Photoelectrochemical Water Splitting Using Dense and Aligned TiO2 Nanorod Arrays. *Small* **2009**, *5* (1), 104–111. https://doi.org/10.1002/smll.200800902.

(158) Liu, M.; Snapp, N. de L.; Park, H. Water Photolysis with a Cross-Linked Titanium Dioxide Nanowire Anode. *Chem. Sci.* **2010**, *2* (1), 80–87. https://doi.org/10.1039/C0SC00321B.

(159) Cho, I. S.; Chen, Z.; Forman, A. J.; Kim, D. R.; Rao, P. M.; Jaramillo, T. F.; Zheng, X. Branched TiO2 Nanorods for Photoelectrochemical Hydrogen Production. *Nano Lett.* **2011**, *11* (11), 4978–4984. https://doi.org/10.1021/nl2029392.

(160) Chen, H. M.; Chen, C. K.; Liu, R.-S.; Zhang, L.; Zhang, J.; Wilkinson, D. P. Nano-Architecture and Material Designs for Water Splitting Photoelectrodes. *Chem. Soc. Rev.* **2012**, *41* (17), 5654–5671. https://doi.org/10.1039/C2CS35019J.

(161) Fan, S.; Shih, I.; Mi, Z. A Monolithically Integrated InGaN Nanowire/Si Tandem Photoanode Approaching the Ideal Bandgap Configuration of 1.75/1.13 EV. *Advanced Energy Materials* **2017**, *7* (2), 1600952. https://doi.org/10.1002/aenm.201600952.

(162) Moses, P. G.; Van de Walle, C. G. Band Bowing and Band Alignment in InGaN Alloys. *Appl. Phys. Lett.* **2010**, *96* (2), 021908. https://doi.org/10.1063/1.3291055.

(163) Chu, S.; Vanka, S.; Wang, Y.; Gim, J.; Wang, Y.; Ra, Y.-H.; Hovden, R.; Guo, H.; Shih, I.; Mi, Z. Solar Water Oxidation by an InGaN Nanowire Photoanode with a Bandgap of 1.7 EV. *ACS Energy Lett.* **2018**, *3* (2), 307–314. https://doi.org/10.1021/acsenergylett.7b01138.

(164) Kubakaddi, S. B.; Chirakkara, S.; Hosamani, G.; Shivaprasad, S. M. Nanostructured P-TiO2/n-GaN Heterostructure as a Potential Photoelectrode for Efficient Charge Separation. *Nanotechnology* **2018**, *29* (50), 50LT02. https://doi.org/10.1088/1361-6528/aae565.

(165) Wu, M. F.; Zhou, S. Q.; Vantomme, A.; Huang, Y.; Wang, H.; Yang, H. High-Precision Determination of Lattice Constants and Structural Characterization of InN Thin Films. *Journal of Vacuum Science & Technology A* **2006**, *24* (2), 275–279. https://doi.org/10.1116/1.2167970.

(166) Darakchieva, V.; Monemar, B.; Usui, A. On the Lattice Parameters of GaN. *Applied Physics Letters* **2007**, *91* (3), 031911. https://doi.org/10.1063/1.2753122.

(167) Urbach, F. The Long-Wavelength Edge of Photographic Sensitivity and of the Electronic Absorption of Solids. *Phys. Rev.* **1953**, *92* (5), 1324–1324. https://doi.org/10.1103/PhysRev.92.1324.

(168) Martin, R. W.; Middleton, P. G.; O'Donnell, K. P.; Van der Stricht, W. Exciton Localization and the Stokes' Shift in InGaN Epilayers. *Appl. Phys. Lett.* **1999**, *74* (2), 263–265. https://doi.org/10.1063/1.123275.

(169) McCluskey, M. D.; Van de Walle, C. G.; Romano, L. T.; Krusor, B. S.; Johnson, N. M. Effect of Composition on the Band Gap of Strained InxGa1−xN Alloys. *Journal of Applied Physics* **2003**, *93* (7), 4340–4342. https://doi.org/10.1063/1.1560563.

(170) Kumawat, U. K.; Kumar, K.; Das, P.; Ahmed, K.; Bhardwaj, P.; Dhawan, A. Enhanced Performance of InGaN Thin-Film Solar Cells Containing Plasmonic and Dielectric Nanostructures. In *Physics, Simulation, and Photonic Engineering of Photovoltaic Devices VIII*; International Society for Optics and Photonics, 2019; Vol. 10913, p 109131P. https://doi.org/10.1117/12.2515405.

(171) Zhang, X.; Liu, Q.; Liu, B.; Yang, W.; Li, J.; Niu, P.; Jiang, X. Giant UV Photoresponse of a GaN Nanowire Photodetector through Effective Pt Nanoparticle Coupling. *J. Mater. Chem. C* **2017**, *5* (17), 4319–4326. https://doi.org/10.1039/C7TC00594F.

(172) Oliva, R.; Zelewski, S. J.; Janicki, \Lukasz; Gwóźdź, K. R.; Serafińczuk, J.; Rudziński, M.; Özbay, E.; Kudrawiec, R. Determination of the Band Gap of Indium-Rich InGaN by Means of Photoacoustic Spectroscopy. *Semicond. Sci. Technol.* **2018**, *33* (3), 035007. https://doi.org/10.1088/1361-6641/aaa908.

(173) Zhang, X.; Liu, B.; Liu, Q.; Yang, W.; Xiong, C.; Li, J.; Jiang, X. Ultrasensitive and Highly Selective Photodetections of UV-A Rays Based on Individual Bicrystalline GaN Nanowire. *ACS Appl. Mater. Interfaces* **2017**, *9* (3), 2669–2677. https://doi.org/10.1021/acsami.6b14907.

(174) Wang, Y.; Schwartz, J.; Gim, J.; Hovden, R.; Mi, Z. Stable Unassisted Solar Water Splitting on Semiconductor Photocathodes Protected by Multifunctional GaN Nanostructures. *ACS Energy Lett.* **2019**, *4* (7), 1541–1548. https://doi.org/10.1021/acsenergylett.9b00549.

(175) AlOtaibi, B.; Harati, M.; Fan, S.; Zhao, S.; Nguyen, H. P. T.; Kibria, M. G.; Mi, Z. High Efficiency Photoelectrochemical Water Splitting and Hydrogen Generation Using GaN Nanowire Photoelectrode. *Nanotechnology* **2013**, *24* (17), 175401. https://doi.org/10.1088/0957-4484/24/17/175401.

(176) Benton, J.; Bai, J.; Wang, T. Significantly Enhanced Performance of an InGaN/GaN Nanostructure Based Photo-Electrode for Solar Power Hydrogen Generation. *Appl. Phys. Lett.* **2013**, *103* (13), 133904. https://doi.org/10.1063/1.4823550.

(177) Yang, C.; Xi, X.; Yu, Z.; Cao, H.; Li, J.; Lin, S.; Ma, Z.; Zhao, L. Light Modulation and Water Splitting Enhancement Using a Composite Porous GaN Structure. *ACS Appl. Mater. Interfaces* **2018**, *10* (6), 5492–5497. https://doi.org/10.1021/acsami.7b15344.

(178) Alvi, N. ul H.; Soto Rodriguez, P. E. D.; Aseev, P.; Gómez, V. J.; Alvi, A. ul H.; Hassan, W. ul; Willander, M.; Nötzel, R. InN/InGaN Quantum Dot Photoelectrode: Efficient Hydrogen Generation by Water Splitting at Zero Voltage. *Nano Energy* **2015**, *13*, 291–297. https://doi.org/10.1016/j.nanoen.2015.02.017.

(179) Sheu, J.-K.; Liao, P.-H.; Cheng, H.-Y.; Lee, M.-L. Photoelectrochemical Hydrogen Generation from Water Using Undoped GaN with Selective-Area Si-Implanted Stripes as a Photoelectrode. *J. Mater. Chem. A* **2017**. https://doi.org/10.1039/C7TA07155H.

(180) Ebaid, M.; Kang, J.-H.; Ryu, S.-W. Controlled Synthesis of GaN-Based Nanowires for Photoelectrochemical Water Splitting Applications. *Semiconductor Science and Technology* **2017**, *32* (1), 013001. https://doi.org/10.1088/0268-1242/32/1/013001.

(181) Xu, Z.; Zhang, S.; Gao, F.; Wen, L.; Yu, Y.; Li, G. Correlations among Morphology, Composition, and Photoelectrochemical Water Splitting Properties of InGaN Nanorods Grown by Molecular Beam Epitaxy. *Nanotechnology* **2018**, *29* (47), 475603. https://doi.org/10.1088/1361-6528/aae0d4.

(182) Deng, J.; Su, Y.; Liu, D.; Yang, P.; Liu, B.; Liu, C. Nanowire Photoelectrochemistry. *Chem. Rev.* **2019**, *119* (15), 9221–9259. https://doi.org/10.1021/acs.chemrev.9b00232.

(183) Zhang, Y.; Tang, L.; Lin, K.; Wang, P.; Xu, C. Investigation on the Effect of Indium Composition on Ultrafast Carrier Dynamics in InGaN Alloys. *Jpn. J. Appl. Phys.* **2018**, *58* (1), 010903. https://doi.org/10.7567/1347-4065/aaecd7.

(184) Davydov, V. Y.; Klochikhin, A. A.; Emtsev, V. V.; Kurdyukov, D. A.; Ivanov, S. V.; Vekshin, V. A.; Bechstedt, F.; Furthmüller, J.; Aderhold, J.; Graul, J.; Mudryi, A. V.; Harima, H.; Hashimoto, A.; Yamamoto, A.; Haller, E. E. Band Gap of Hexagonal InN and InGaN Alloys. *physica status solidi (b)* **2002**, *234* (3), 787–795. https://doi.org/10.1002/1521-3951(200212)234:3<787::AID-PSSB787>3.0.CO;2-H.

(185) Kuykendall, T.; Ulrich, P.; Aloni, S.; Yang, P. Complete Composition Tunability of InGaN Nanowires Using a Combinatorial Approach. *Nature Materials* **2007**, *6* (12), 951–956. https://doi.org/10.1038/nmat2037.

(186) *Evolution of phase separation in In-rich InGaN alloys: Applied Physics Letters: Vol 96, No 23*. https://aip.scitation.org/doi/abs/10.1063/1.3453563?journalCode=apl (accessed 2021-05-19).

(187) Papadomanolaki, E.; Bazioti, C.; Kazazis, S. A.; Androulidaki, M.; Dimitrakopulos, G. P.; Iliopoulos, E. Molecular Beam Epitaxy of Thick InGaN(0001) Films: Effects

of Substrate Temperature on Structural and Electronic Properties. *Journal of Crystal Growth* **2016**, *437*, 20–25. https://doi.org/10.1016/j.jcrysgro.2015.12.012.

(188) Woo, H.; Jo, Y.; Kim, J.; Cho, S.; Roh, C. H.; Lee, J. H.; Kim, H.; Hahn, C.-K.; Im, H. Correlation between Pit Formation and Phase Separation in Thick InGaN Film on a Si Substrate. *Current Applied Physics* **2018**, *18* (12), 1558–1563. https://doi.org/10.1016/j.cap.2018.10.002.

(189) Juodkazytė, J.; Šebeka, B.; Savickaja, I.; Kadys, A.; Jelmakas, E.; Grinys, T.; Juodkazis, S.; Juodkazis, K.; Malinauskas, T. InxGa1−xN Performance as a Band-Gap-Tunable Photo-Electrode in Acidic and Basic Solutions. *Solar Energy Materials and Solar Cells* **2014**, *130* (Supplement C), 36–41. https://doi.org/10.1016/j.solmat.2014.06.033.

(190) Liu, Q.; Shi, J.; Xu, Z.; Zhang, B.; Liu, H.; Lin, Y.; Gao, F.; Li, S.; Li, G. InGaN Nanorods Decorated with Au Nanoparticles for Enhanced Water Splitting Based on Surface Plasmon Resonance Effects. *Nanomaterials* **2020**, *10* (5), 912. https://doi.org/10.3390/nano10050912.

(191) Cao, D.; Xiao, H.; Gao, Q.; Yang, X.; Luan, C.; Mao, H.; Liu, J.; Liu, X. Fabrication and Improved Photoelectrochemical Properties of a Transferred GaN-Based Thin Film with InGaN/GaN Layers. *Nanoscale* **2017**, *9* (32), 11504–11510. https://doi.org/10.1039/C7NR03622A.

(192) Alvi, N. H.; Rodriguez, P. E. D. S.; Kumar, P.; Gómez, V. J.; Aseev, P.; Alvi, A. H.; Alvi, M. A.; Willander, M.; Nötzel, R. Photoelectrochemical Water Splitting and Hydrogen Generation by a Spontaneously Formed InGaN Nanowall Network. *Applied Physics Letters* **2014**, *104* (22), 223104. https://doi.org/10.1063/1.4881324.

(193) Caccamo, L.; Hartmann, J.; Fàbrega, C.; Estradé, S.; Lilienkamp, G.; Prades, J. D.; Hoffmann, M. W. G.; Ledig, J.; Wagner, A.; Wang, X.; Lopez-Conesa, L.; Peiró, F.; Rebled, J. M.; Wehmann, H.-H.; Daum, W.; Shen, H.; Waag, A. Band Engineered Epitaxial 3D GaN-InGaN Core–Shell Rod Arrays as an Advanced Photoanode for Visible-Light-Driven Water Splitting. *ACS Appl. Mater. Interfaces* **2014**, *6* (4), 2235–2240. https://doi.org/10.1021/am4058937.

(194) Ebaid, M.; Min, J.-W.; Zhao, C.; Ng, T. K.; Idriss, H.; Ooi, B. S. Water Splitting to Hydrogen over Epitaxially Grown InGaN Nanowires on a Metallic Titanium/Silicon Template: Reduced Interfacial Transfer Resistance and Improved Stability to Hydrogen. *J. Mater. Chem. A* **2018**, *6* (16), 6922–6930. https://doi.org/10.1039/C7TA11338B.

(195) Effect of Minute Compositional Variations on the Photoelectrochemical Properties of InGaN/TiO2 Heterostructure Electrodes. *Applied Surface Science* **2021**, *539*, 148251. https://doi.org/10.1016/j.apsusc.2020.148251.

(196) Dunn, H. K.; Feckl, J. M.; Müller, A.; Fattakhova-Rohlfing, D.; Morehead, S. G.; Roos, J.; Peter, L. M.; Scheu, C.; Bein, T. Tin Doping Speeds up Hole Transfer during Light-Driven Water Oxidation at Hematite Photoanodes. *Phys. Chem. Chem. Phys.* **2014**, *16* (44), 24610–24620. https://doi.org/10.1039/C4CP03946G.

(197) Luo, W.; Liu, B.; Li, Z.; Xie, Z.; Chen, D.; Zou, Z.; Zhang, R. Stable Response to Visible Light of InGaN Photoelectrodes. *Appl. Phys. Lett.* **2008**, *92* (26), 262110. https://doi.org/10.1063/1.2955828.

(198) Aryal, K.; Pantha, B. N.; Li, J.; Lin, J. Y.; Jiang, H. X. Hydrogen Generation by Solar Water Splitting Using P-InGaN Photoelectrochemical Cells. *Appl. Phys. Lett.* **2010**, *96* (5), 052110. https://doi.org/10.1063/1.3304786.

(199) Crawford, S.; Thimsen, E.; Biswas, P. Impact of Different Electrolytes on Photocatalytic Water Splitting. *J. Electrochem. Soc.* **2009**, *156* (5), H346. https://doi.org/10.1149/1.3090177.

(200) *P2: Standard Reduction Potentials by Value*. Chemistry LibreTexts. https://chem.libretexts.org/Ancillary_Materials/Reference/Reference_Tables/Electrochemistry_Tables/P2%3A_Standard_Reduction_Potentials_by_Value (accessed 2022-03-03).

(201) Finken, M.; Wille, A.; Reuters, B.; Heuken, M.; Kalisch, H.; Vescan, A. Investigations of the Electrochemical Stability of InGaN Photoanodes in Different Electrolytes. *physica status solidi (b)* **2015**, *252* (5), 895–899. https://doi.org/10.1002/pssb.201451576.

(202) Chu, S.; Li, W.; Yan, Y.; Hamann, T.; Shih, I.; Wang, D.; Mi, Z. Roadmap on Solar Water Splitting: Current Status and Future Prospects. *Nano Futures* **2017**, *1* (2), 022001. https://doi.org/10.1088/2399-1984/aa88a1.

(203) *Morphology and optical properties of InN layers grown by molecular beam epitaxy on silicon substrates - Grandal - 2005 - physica status solidi (c) - Wiley Online Library*. https://onlinelibrary.wiley.com/doi/abs/10.1002/pssc.200461571 (accessed 2022-03-07).

(204) Ebaid, M.; Min, J.-W.; Zhao, C.; Ng, T. K.; Idriss, H.; Ooi, B. S. Water Splitting to Hydrogen over Epitaxially Grown InGaN Nanowires on a Metallic Titanium/Silicon Template: Reduced Interfacial Transfer Resistance and Improved Stability to Hydrogen. *J. Mater. Chem. A* **2018**, *6* (16), 6922–6930. https://doi.org/10.1039/C7TA11338B.

(205) Uchida, Y.; Ito, K.; Tsukimoto, S.; Ikemoto, Y.; Hirata, K.; Shibata, N.; Murakami, M. Epitaxial Growth of GaN Layers on Metallic TiN Buffer Layers. *J. Electron. Mater.* **2006**, *35* (10), 1806–1811. https://doi.org/10.1007/s11664-006-0161-6.

(206) *Titanium and titanium nitride contacts to n-type gallium nitride - IOPscience*. https://iopscience.iop.org/article/10.1088/0268-1242/13/11/017 (accessed 2022-03-07).

(207) Kern, W. The Evolution of Silicon Wafer Cleaning Technology. *J. Electrochem. Soc.* **1990**, *137* (6), 1887. https://doi.org/10.1149/1.2086825.

(208) Caccamo, L.; Cocco, G.; Martín, G.; Zhou, H.; Fundling, S.; Gad, A.; Mohajerani, M. S.; Abdelfatah, M.; Estradé, S.; Peiró, F.; Dziony, W.; Bremers, H.; Hangleiter, A.; Mayrhofer, L.; Lilienkamp, G.; Moseler, M.; Daum, W.; Waag, A. Insights into Interfacial Changes and Photoelectrochemical Stability of InxGa1–XN (0001)

Photoanode Surfaces in Liquid Environments. *ACS Appl. Mater. Interfaces* **2016**, *8* (12), 8232–8238. https://doi.org/10.1021/acsami.5b12583.

(209) Koike, K.; Yamamoto, K.; Ohara, S.; Kikitsu, T.; Ozasa, K.; Nakamura, S.; Sugiyama, M.; Nakano, Y.; Fujii, K. Effects of NiO-Loading on n-Type GaN Photoanode for Photoelectrochemical Water Splitting Using Different Aqueous Electrolytes. *International Journal of Hydrogen Energy* **2017**, *42* (15), 9493–9499. https://doi.org/10.1016/j.ijhydene.2016.12.141.

(210) *High Efficiency Solar-to-Hydrogen Conversion on a Monolithically Integrated InGaN/GaN/Si Adaptive Tunnel Junction Photocathode | Nano Letters*. https://pubs.acs.org/doi/abs/10.1021/acs.nanolett.5b00535 (accessed 2022-11-17).

List of Publications

1. Kubakaddi, Shivaram B., et al. "Nanostructured p-TiO2/n-GaN heterostructure as a potential photoelectrode for efficient charge separation." Nanotechnology 29.50 (2018): 50LT02.

2. Shivaram, B. K., Saraswathi Chirakkara, and S. M. Shivaprasad. "Effect of minute compositional variations on the photoelectrochemical properties of InGaN/TiO2 heterostructure electrodes." Applied Surface Science 539 (2021): 148251.

3. Shivaram, B. K., Saraswathi Chirakkara, and S. M. Shivaprasad. "The dominant role of surface morphology and indium composition on the photoelectrochecmical properties of epitaxial InGaN nanostructures" Manuscript submitted.

4. Shivaram, B. K., Saraswathi Chirakkara, and S. M. Shivaprasad. "Investigations on the role of the indium composition on the photoelectrochemical properties of InGaN grown on epi GaN " Manuscript under preparation.

5. Shivaram, B. K., Saraswathi Chirakkara, and S. M. Shivaprasad. "Effect of the interfacial TiN layer on the PEC properties of InGaN grown on Si (111)" Manuscript under preparation.